Title
On the Implementation and Applications of Discrete-Time Filters for Soil-Structure Interaction Analyses

Author
Gash, Richard J.H.

Publication Date
2015

Peer reviewed|Thesis/dissertation

University of California

Los Angeles

On the Implementation and Applications of Discrete-Time Filters for Soil-Structure Interaction Substructure Analyses

A dissertation submitted in partial satisfaction

of the requirements for the degree

Doctor of Philosophy in Civil Engineering

by

Richard James Henry Gash

2015

Abstract of the Dissertation

On the Implementation and Applications of Discrete-Time Filters for Soil-Structure Interaction Substructure Analyses

by

Richard James Henry Gash

Doctor of Philosophy in Civil Engineering

University of California, Los Angeles, 2015

Professor Ertugrul Taciroglu, Chair

This work explores the implementation and applications of discrete-time filters as time-domain approximations of frequency-dependent foundation impedance functions for use in substructure dynamic response history analysis. The project's ultimate objective is to offer practicing engineers a robust, reliable option for accounting for inertial soil-structure interaction in time domain analyses.

The substructure method is a means of accounting for the interaction between a structure, its foundation, and the surrounding geology when subjected to dynamic excitation. The method models the soil-foundation interface using what are termed the *foundation impedance functions*. The frequency dependence of these functions complicates the method's implementation, especially in the time domain. Approximating impedance functions using discrete time filters yields recursive, time-dependent relations that may subsequently be incorporated into the system's equations of motion for integration using standard time-stepping methods.

Work along four interconnected lines of inquiry are presented. The first thread comprises a critical review of existing literature and delineates the motivation for

the present effort. The second provides formulation and implementation details for both elastic and inelastic structural systems. Also included is a detailed analytical and numerical analysis of the stability of combined filter-integrator. The third line of effort includes three practical applications of the filter method, an investigation into the effects of inertial soil-structure interaction on yielding systems, a demonstration of the effects of soil profile on constant ductility spectra, and a case study wherein the filter method is used to predict the response of the Millikan Library on the campus of the California Institute of Technology to the 2002 Yorba Linda Earthquake. The final line of effort specifically targets practicing engineers by offering further detail on filter design and features a tutorial on filter design using the MATLAB® programming environment.

The dissertation of Richard James Henry Gash is approved.

Jian Zhang

Jonathan P. Stewart

Ali H. Sayed

Ertugrul Taciroglu, Committee Chair

University of California, Los Angeles

2015

To my wife, my partner in all things: Thank you.

And to my children: May you each live to make the world a better place.

Table of Contents

List of Figures

List of Tables

Acknowledgments

This work would not have been possible without the help of many individuals and organizations. Thank you to the Department of Civil and Mechanical Engineering at the United States Military Academy for offering me the opportunity to undertake this endeavor via the United States Army's Advanced Civil Schooling Program. A special thank you to my advisor and committee chair, Professor Ertugrul Taciroglu for your mentorship and guidance throughout this process. Thank you also to the members of my committee, Professor Ali Sayed, Professor Jonathan Stewart, and Professor Jian Zhang. You have each challenged me and inspired me. Finally, thank you to my colleagues, Farid Ghahari and Elnaz Esmaeilzadeh Seylabi. Your assistance, advice, and encouragement has been invaluable.

The manuscript was prepared using the `uclathes` LaTeX document template available at: `https://github.com/jolohaga/uclathes`.

Vita

1996	B.S. (Civil Engineering), United States Military Academy.
1996-Present	Commissioned Officer in the United States Army Corps of Engineers. Highlights of military service include:
1996-1999	Combat Engineer Platoon Leader 1st Armored Division, Fort Riley, Kansas.
2002-2004	Horizontal Construction Company Commander 864th Engineer Battalion, Fort Lewis, Washington.
2003	Award of the Bronze Star Medal for combat service in Iraq.
2006-2008	Instructor, Department of Civil and Mechanical Engineering United States Military Academy, West Point, New York.
2007	Advisor to the National Military Academy of Afghanistan Combined Security and Transition Command, Afghanistan.
2010-2011	Battalion Executive Officer 2nd Infantry Division, Republic of Korea.
2011-2012	Director of Public Works Camp As Sayliyah, Qatar.
2000	M.S. (Geology and Geophysics), University of Missouri, Rolla.
2001	Registration as a Professional Engineer in Missouri and Ohio.
2006	M.S. (Civil Engineering), University of California, Los Angeles.

2008 Recognition as Young Governmental Engineer of the Year by the American Society of Civil Engineers

Presentations

Stable Time-domain Representation of Foundation Impedance Functions. Engineering Mechanics Institute Conference. Hamilton, Ontario. August, 2014

CHAPTER 1

Introduction

1.1 Motivation

Structures constantly experience loading. They must withstand their own weight, the forces induced by their intended use, and those forces generated by the environment within which they exist. It is often this latter category, the environment, which provides the most extreme loading events. Engineers must design structures to withstand hurricane-force winds, earthquakes, and even blast and impact loads. One tool that engineers use to investigate the structural response to such extreme loads is response history analysis. This typically involves development of a mathematical model of the structure and its environment, application of the anticipated loading conditions, and observation of the model's performance over time, both during and after loading. From this response history, engineers can then harvest parameters of interest such as displacements and forces generated within the structural members.

Consider now, a massive structure such as the containment facility for a nuclear power plant. Imagine that structure shaking during an earthquake. Due to its weight and stiffness, it will initially resist seismic motion, but once it begins to move, its substantial inertia will seek to keep it in motion. It will, in effect, impart energy back into the ground. The ensuing feedback loop—i.e., "ground shakes the building, and the shaking building, in turn, shakes the already-shaking ground"—complicates the response history analysis, and may necessitate a simultaneous and

fully-coupled analysis of the structure and its surrounding soil media. This effect is often referred to as *inertial* soil-structure interaction (SSI). More technically, inertial SSI is defined as the phenomenon wherein inertia developed within a vibrating structure generates forces and moments that cause displacements of the foundation with respect to the free-field. These displacements may be seen as the difference between the response of the soil in the presence of the foundation and the expected response of the soil to the same excitation if the structure were not present.

In most cases, inertial SSI tends to reduce the overall response of a structure. In fact, initial guidelines for building codes allowed engineers to either ignore SSI effects, or more liberally, take blanket reductions to the expected response [1]. Quite to the contrary, it is now widely accepted that stiff, short-period structures (such as the nuclear containment facility from above) may actually experience increased responses due to the effects of inertial SSI. Worse, when structures become damaged or otherwise exhibit inelastic behavior during shaking, recent work suggests that amplified responses should be expected for a much broader range of structures than merely stiff and massive ones [2].

Current practice for accounting for inertial SSI involves modeling the foundation-soil interface using complex-valued impedance functions. These functions may be conceptualized as a set of springs and dampers (dashpots) that transfer motion between the soil-foundation system and the far-field. Impedance functions for various simple foundation geometries and soil profiles are readily available in the relevant literature. Recent advances in computational methods have also allowed for generation of impedance functions for more complicated foundation-soil systems [3]. One major obstacle hindering the widespread use of these functions in engineering practice is that they vary with frequency. This frequency dependence complicates their use in use in response history analysis, which is required when the supported structure exhibits any nonlinearity. The current

state-of-practice includes several methods of addressing this issue, but all have various short comings—as will be discussed later—that inhibit their utility, and hence, widespread adoption.

1.2 Research Objective

The goal of this work is to improve the current state of earthquake engineering practice by devising, implementing, and applying a viable method to accurately account for inertial soil-structure interaction in time-domain substructure analyses. The approach that will be developed here leverages signal processing theory to represent frequency-dependent foundation impedance functions as discrete-time filters. The end-state is a tool that practicing engineers can use to efficiently generate site-specific nonlinear response histories that are necessary for performance-based seismic assessment and design.

1.3 Organization

Figure 1.1 displays the organization of this work. The project as a whole follows four lines of effort toward achievement of the overall objective. As the figure shows, each line of effort contains several "milestones" or subordinate objectives. This manuscript documents progress toward the overall goal by following loosely from the upper left of the figure to its lower right. The various milestones are grouped into chapters according to the key at the bottom of the figure.

The first line of effort investigates the background literature and establishes its motivation. It sets the project's research objective, examines the current state-of-practice, demonstrates the necessary signal processing tools, and concludes with a reproduction of previously published results. The second line effort focuses on implementation of the filter method for both elastic and inelastic structures

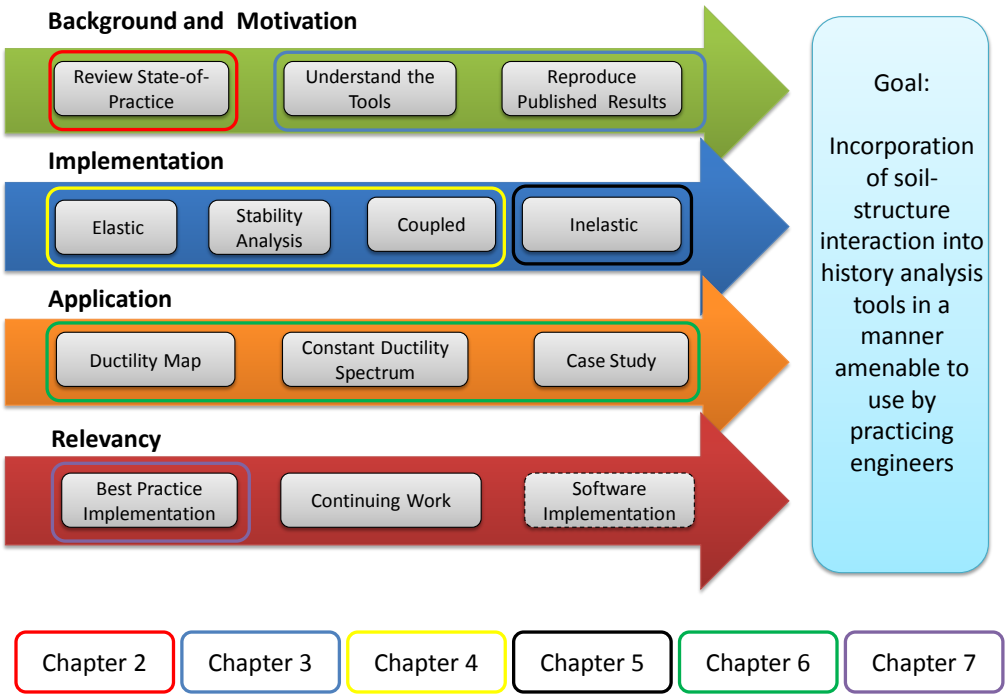

Figure 1.1: *Project organization.*

subject to first uncoupled, and subsequently coupled, motions. Included is a robust analytical and numerical stability analysis.

The third line of effort provides three parametric studies carried out using the filter method: The first study seeks to answer the question "is soil-structure interaction beneficial or detrimental?" through the construction of a set of ductility maps. The second couples the filter method with advances in computational mechanics that allow efficient computation of impedance functions for arbitrary soil profiles and foundation geometries to demonstrate the effects that soil profile can have on constant ductility spectra. The third one is a case study demonstrating use of the filter method to predict the dynamic responses of the Millikan Library—a USGS-instrumented building located on the campus of the California Institute of Technology—during the 2002 Yorba Linda Earthquake.

The final line of effort is targeted to practicing civil engineers who may not readily possess the signal processing skills necessary to implement and gainfully use the filter method. It includes a detailed filter design tutorial that makes use of the MATLAB programing environment.

This dissertation concludes by identifying the future work needed to develop a comprehensive soil-structure interaction software package that can be integrated into state-of-the-art commercial structural analysis software.

CHAPTER 2

State-of-practice

2.1 Soil Structure Interaction

The field of soil-structure interaction involves examination of how a structure, its foundation, and the surrounding geologic media respond as a system to dynamic loading. Such loading may come from vehicles, machinery, wind, and even blasts. The vast majority of SSI-related research, however, relates to earthquake-induced vibrations. In his work "*Soil Structure Interaction, The Early Stages*," Roesset [4] credits the likes of Sezawa, Martel, and Housner, whose works from the 1930s through 1950s launched this field of study as an independent research area. These early pioneers analyzed newly available recordings of strong seismic events and the corresponding structural responses they induced. They noted, and sought to account for, differences between observed responses and those predicted by contemporary theories, which assumed structures moved in exact compliance with their supporting media.

The 1970s saw what Kausel [5] referred to as the beginning of the modern era of seismic soil-structure interaction. During this time, the field enjoyed tremendous research gains enabled by advances in computer-aided numerical methods and driven by funding from the nuclear power industry. Out of these efforts, two broad categories of SSI effects emerged. The first, termed *kinematic effects*, related to the interaction between incoming seismic waves and a foundation due to discrepancies among their stiffness. The second, termed *inertial effects*, addressed

the phenomenon of a moving structure imparting energy through its foundation back to its supporting soil. This latter phenomenon leads to foundation displacements, rotations, and energy dissipation through radiation and hysteretic soil damping that are not accounted for if the systems foundation is modeled as *fixed* to the surrounding soil and geological media. It is generally agreed that these kinematic and inertial effects combine to lengthen a structure's natural period of vibration.

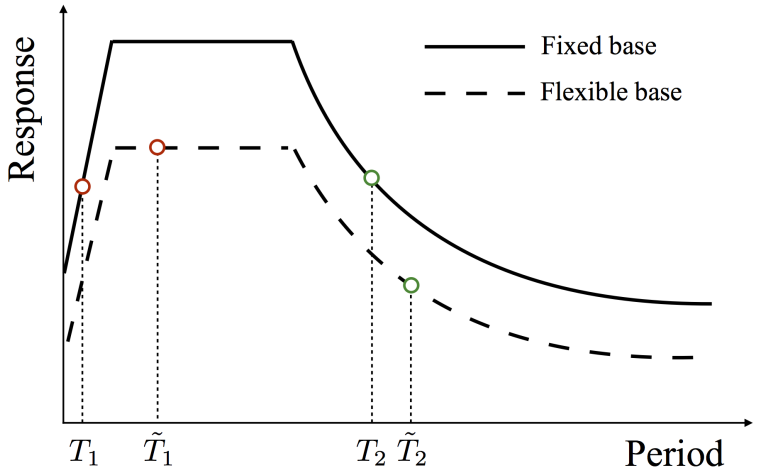

Figure 2.1: *Generic design spectra for fixed- and flexible-base SDOF structures with different natural periods.*

The consequences of considering or neglecting SSI effects can be seen in Figure 2.1, which displays a *design spectra*. On the figure, the abscissa depicts a range of hypothetical structural periods and the ordinate depicts spectral responses—i.e., the maximum values of a given response parameter, such as displacement or acceleration, that a structure can expect to experience when excited by a set of anticipated ground motions. Note the difference between the structures repre-

sented by T_1 and T_2. Structure T_2 has a relatively long period, like that of a tall, slender building or a flexible bridge. Structure T_1 has a relatively short period, akin to that of a short, stiff structure. If T_2 elongates to $\tilde{T}_2$ due to SSI, then the structure's anticipated spectral response decreases. Conversely, when T_1 elongates to $\tilde{T}_1$, its spectral response increases. In this case, soil-structure interaction *increases* the demand on the structure. Zhang and Tang quantified these (among other) effects using a dimensional analysis approach [6].

While design spectra are useful tools, they only estimate the maximum of a given response parameter. In many cases, engineers are more interested in a structure's response history, or how it will respond to dynamic loading over time. To this end, two major methods of soil-structure response history analysis have evolved. Termed the *direct method* and the *substructure method*, both address kinematic and inertial interaction, and offer viable means of determining response history. Both are currently used in practice.

2.1.1 Direct and Substructure Methods of Analysis of SSI

The first method, commonly referred to as the direct method, involves the discretization of the combined soil-foundation-structure system, typically with the finite element method. While this method does offer the potential to account for both kinematic and inertial SSI effects in one step, its complexity and computational expense has prohibited its widespread adoption in engineering practice [7].

The alternative is the substructure method, which divides the solution into three component steps. The first step involves the adjustment of the anticipated seismic input motion to account for kinematic effects. To accomplish this, a transfer function is typically used to convert free-field motions—or the motion a particular site would feel in the absence of the structure and foundation—into what is termed a *foundation input motion*. This is generally accomplished by carrying

out analyses with a direct method wherein the the foundation system is modeled with its inherent stiffness but with no (or negligible) mass. The second step involves accounting for inertial interaction effects through the determination of a set of foundation impedance functions, which represent the soil-foundation system's dynamic stiffness and radiation damping. During the final step, the foundation input motion is applied to the structure through the foundation impedance functions. It is in this third step of the substructure method is where the significant contributions of this research lie: the goal being to offer engineers a viable method of approximating the inherently frequency-dependent foundation impedance functions in the time-domain, in a way that facilitates straight-forward and accurate response history analyses.

The following two sections take a closer look at steps two and three of the substructure analysis method.

2.1.2 The Substructure Method: Foundation Impedance Functions

Foundation impedance functions offer a means of mathematically representing a truncated soil domain's reactions at the soil-foundation interface. The concept of a foundation impedance function grew out of early work by researchers such as Reissner [8], Bycroft [9], and others. To date, analytical and semi-analytical solutions exist in the literature for many simple foundation geometries and soil conditions (see, for example, [10–14]). Also, recent advances in computational mechanics now offer a means of generating impedance functions for more complicated foundation geometries and soil profiles including tunnels, and highway overpass approach embankments [3, 15]. While specific notation tends to vary, foundation impedance functions typically take the form

$$\bar{k}_j = k_j + i\omega c_j \tag{2.1}$$

where k_j represents stiffness, c_j represents damping, the subscript j represents the direction of motion, and i represents $\sqrt{-1}$. In addition to the linear frequency dependence inherent in the imaginary term, both k_j and c_j may also vary with frequency.

2.1.3 The Substructure Method: Response History Analysis

Once an engineer has determined the foundation input motion and obtained the relevant set of foundation impedance functions for a given soil-foundation-structure system, the final step in the substructure method involves computation of the structure's anticipated response. Numerous methods exist to accomplish this. Some yield only maximum response parameters; others offer an entire response history. This work will examine for existing methods from the latter category—*viz.*, a frequency domain solution, a convolution-based solution, a representative frequency solution, and a lumped parameter model—as verification metrics to gage the performance of the filter method that will be devised here.

The frequency domain solution uses a transfer function to solve a structure's equations of motion in the frequency domain. As the transfer function exists in the frequency domain, it is relatively straightforward to insert a frequency-dependent foundation impedance function into the solution. Unfortunately, this method is only valid for linear analyses; it cannot be used to analyze structures that undergo inelastic deformations.

The second method involves convolution of the impedance functions' impulse responses in the time domain. While this method has the potential to address the major deficiency of the frequency domain solution in that it could account for inelastic structural deformations, it also has major drawbacks. The first is relatively large computational expense of convolution. The second is the potential for inaccuracy stemming from a phenomenon know as *time-domain leakage*. Despite

these issues, the convolution solution is worth investigating, as its implementation is similar to that of the filter method.

The third method is the most popular in practice. It removes the frequency dependence from the impedance functions by evaluating them at some representative frequency, often the flexible-base first mode natural frequency of the structure [7], or the frequency of a representative single-degree-of-freedom (SDOF) oscillator [16]. This method works well for elastic structures with first-mode dominated responses. The method has challenges accommodating inelastic structures whose natural frequency may change during loading. This issue may be exaggerated by a "jagged" impedance function that show significant variation with frequency.

The final method uses Wolf's lumped parameter—a.k.a. *monkey tail*—model [17] to replace the foundation impedance functions with sets of masses, dashpots, and springs. Wolf offers lumped parameter models for simple soil-foundation systems, such as a rigid disk resting on a uniform half space. Others have formulated methods for deriving more complicated lumped parameter models for arbitrary foundations founded on non-homogeneous soil profiles [18]. The next chapter demonstrates implementation of each of these four methods as well as a fixed-base reference solution.

2.2 Implementation of Existing Methods

Consider the soil-foundation-structure system depicted in Figure 2.2(a). The system consists of a single degree-of-freedom (SDOF) structure supported by a rigid disk that rests on a uniform soil half-space. Its key physical properties are listed in Table 2.1.

The geological values for this system are chosen to reflect those occurring at California Strong Motion Instrumentation Program (CSMIP) Station 58223 lo-

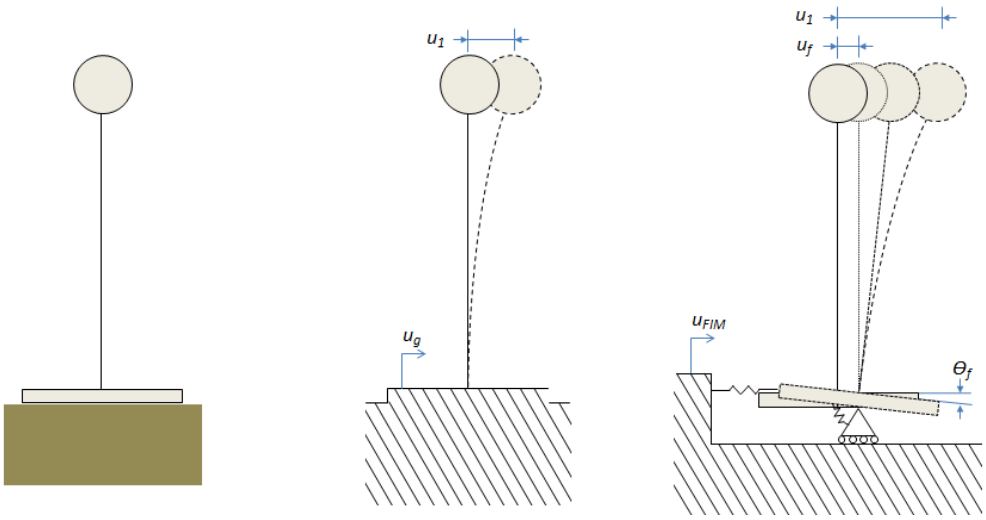

(a) Soil-Foundation-Structure System **(b)** Fixed Base Model **(c)** Substructure Model

Figure 2.2: *A simple soil-foundation-structure system with fixed base and substructure models.*

cated at the San Francisco International Airport (SFO). The ground motion used to excite the system will be the east-west surface motion recorded at SFO during the October 17, 1989 Loma Prieta Earthquake. The acceleration record for this event is plotted in Figure 2.3. It contains $L = 200$ data points spaced at $\Delta_t = 0.02$ seconds. During this event, the site experienced a peak horizontal acceleration of $0.24g$. The record's Fourier amplitude spectrum is shown in Figure 2.4. The maximum value of the smoothed Fourier amplitude spectrum yields the predominant period $T_p = 0.44$ second which occurs at 2.29 Hertz.

Figure 2.2(b) displays a fixed-base model of the structure. In this model, the foundation is assumed to be part of a rigid base. The structure is attached to this base using a connection that prohibits both translation and rotation. The system is excited by applying the desired ground motion to the rigid base. In this case, the ground motion u_g represents the free-field motion. The motion of the

Table 2.1: *Soil-Foundation-Structure System Parameters.*

Geology	
G: Soil Bulk Modulus	2.43 kip/in^2
V_s: Shear Wave Velocity	500 ft/sec
ν: Poisson's Ratio	1/3
Structure	
w: Structure Weight	1000 kips
w_f: Foundation Weight	100 kips
h: Structure Height	30 ft
T: Structural Period	1 sec
ξ: Damping Ratio	0.03
r: Foundation Radius	10 ft
h_f: Foundation Thickness	3 ft

structure can be expressed via the semi-discrete second-order differential equation

$$m\ddot{u}_{1,n} + c\dot{u}_{1,n} + ku_{1,n} = -m\ddot{u}_{g,n} \tag{2.2}$$

where m, c, and k represent structural mass, damping, and stiffness and $\ddot{u}_{1,n}$, $\dot{u}_{1,n}$, and $u_{1,n}$ indicate acceleration, velocity, and displacement at time n. On the right-hand-side of the equation, $\ddot{u}_{g,n}$ represents the free-field ground acceleration at time n. The system has a natural frequency of

$$\omega_0 = \sqrt{\frac{k}{m}} \tag{2.3}$$

and a damping ratio of

$$\xi = \frac{c}{2\sqrt{mk}}\,. \tag{2.4}$$

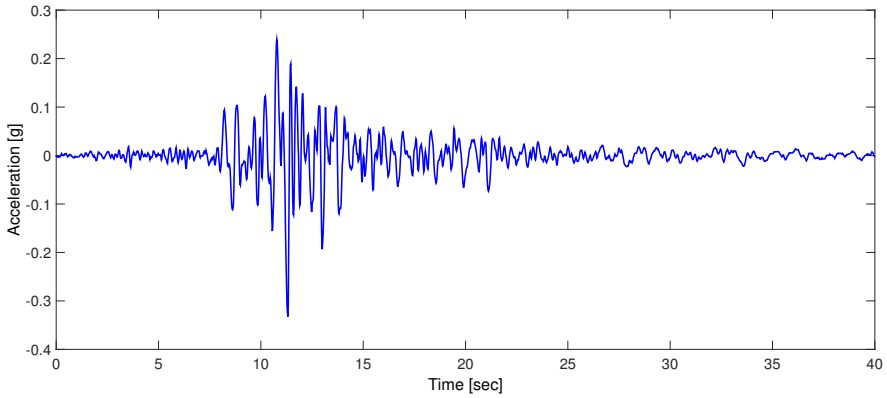

Figure 2.3: *East-West ground acceleration recorded at the San Francisco International Airport during the 1989 Loma Prieta Earthquake.*

Noting that natural frequency is related to structural period by

$$\omega_0 = \frac{2\pi}{T}\,, \tag{2.5}$$

k and c may be expressed in terms of the values in Table 2.1 as

$$k = \frac{4\pi^2 w}{T^2 g} \tag{2.6}$$

and

$$c = 2\xi\sqrt{\frac{wk}{g}} \tag{2.7}$$

with g representing gravitational acceleration.

Figure 2.2(c) displays a substructure model of the system. Here, the rigid foundation remains, but the surrounding soil is replaced by the horizontal foundation impedance function $\bar{k}_x$, and the rotational foundation impedance function $\bar{k}_\theta$. Thus, the foundation is allowed to both translate and rotate. As the system is relatively simple, a rigid disk foundation resting on a homogeneous soil half-space, suitable impedance functions are readily available in the literature. Veletsos and Verbic [12], define them as

$$\bar{k}_x = \frac{8Gr}{2-\nu}\left[k_x + ia_0 c_x\right] \tag{2.8}$$

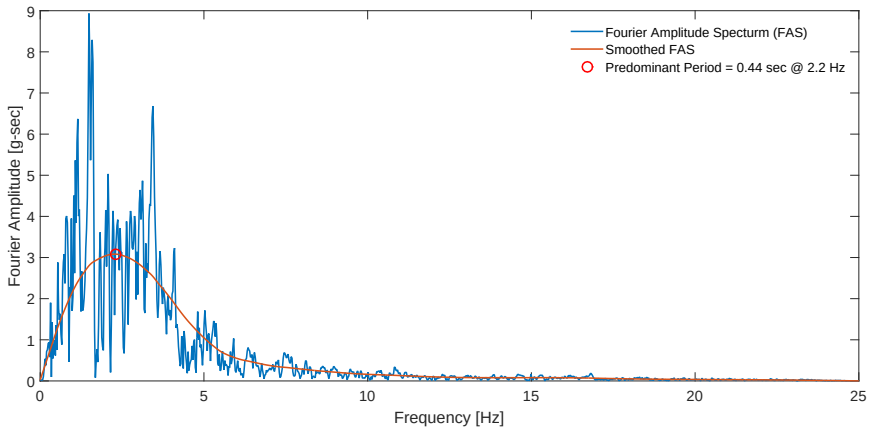

Figure 2.4: *Fourier amplitude spectrum of East-West ground acceleration recorded at the San Francisco International Airport during the 1989 Loma Prieta Earthquake.*

where

$$k_x = 1\,, \qquad c_x = 0.65\,, \qquad a_0 = \frac{\omega r}{V_s}\,,$$

and

$$\bar{k}_\theta = \frac{8Gr^3}{3-3\nu}\left[k_\theta + ia_0 c_\theta\right]\,, \tag{2.9}$$

where

$$k_\theta = 1 - \frac{\beta_1(\beta_2 a_0)^2}{1+\beta_2 a_0)^2}\,, \qquad c_\theta = \frac{\beta_1\beta_2(\beta_2 a_0)^2}{1+\beta_2 a_0)^2}\,,$$
$$\beta_1 = 0.8\,, \qquad \beta_2 = 0.5\,, \qquad a_0 = \omega r/V_s\,.$$

In this model, the system is excited by applying the foundation input motion (u_{FIM}) to the left-side of the horizontal spring. As shown, the fixed base model ignores the effects of both inertial and kinematic interaction while the substructure model has the ability to account for both. That said, as the focus of this work is on inertial interaction, in what follows, the free-field motion will be used as the foundation input motion ($u_g = u_{FIM}$) to isolate inertial effects. The equations of

motion for the soil-foundation-structure system may thus be stated as

$$\begin{bmatrix} m & 0 & 0 \\ 0 & m_f & 0 \\ 0 & 0 & I_f \end{bmatrix} \begin{Bmatrix} \ddot{u}_{1,n} \\ \ddot{u}_{f,n} \\ \ddot{\theta}_{f,n} \end{Bmatrix} + \begin{bmatrix} c & -c & -ch \\ -c & c & ch \\ -ch & ch & ch^2 \end{bmatrix} \begin{Bmatrix} \dot{u}_{1,n} \\ \dot{u}_{f,n} \\ \dot{\theta}_{f,n} \end{Bmatrix} + \begin{bmatrix} k & -k & -kh \\ -k & k & kh \\ -kh & kh & kh^2 \end{bmatrix} \begin{Bmatrix} u_{1,n} \\ u_{f,n} \\ \theta_{f,n} \end{Bmatrix} + \begin{Bmatrix} 0 \\ f_{x,n} \\ f_{\theta,n} \end{Bmatrix} = - \begin{Bmatrix} m \\ m_f \\ 0 \end{Bmatrix} \ddot{u}_{g,n} \quad (2.10)$$

in which I_f represents the foundation's moment of inertia, h represents the structure's height, and $f_{x,n}$ and $f_{\theta,n}$ represent the forces generated by the impedance springs $\bar{k}_x$ and $\bar{k}_\theta$ respectively. Stated in matrix form these equations become

$$\boldsymbol{M}\ddot{\boldsymbol{u}}_n + \boldsymbol{C}\dot{\boldsymbol{u}}_n + \boldsymbol{K}\boldsymbol{u}_n + \boldsymbol{f}_n = \boldsymbol{p}_n \quad (2.11)$$

with $\boldsymbol{M}$, $\boldsymbol{C}$, and $\boldsymbol{K}$ typically referred to as the system's mass, damping, and stiffness matrices. As the foundation impedance functions vary with frequency, determination of $\boldsymbol{f}_n$ in the time domain is not straightforward. It is thus often convenient to restate the equations of motion in the frequency domain as

$$\left(-\omega_l^2 \begin{bmatrix} m & 0 & 0 \\ 0 & m_f & 0 \\ 0 & 0 & I_f \end{bmatrix} + i\omega_l \begin{bmatrix} c & -c & -ch \\ -c & c & ch \\ -ch & ch & ch^2 \end{bmatrix} + \begin{bmatrix} k & -k & -kh \\ -k & k & kh \\ -kh & kh & kh^2 \end{bmatrix} \right) \begin{Bmatrix} U_{t,l} \\ U_{f,l} \\ \Theta_{f,l} \end{Bmatrix} + \begin{Bmatrix} 0 \\ F_{x,l} \\ F_{\theta,l} \end{Bmatrix} = - \begin{Bmatrix} m \\ m_f \\ 0 \end{Bmatrix} \ddot{U}_{g,l} \quad (2.12)$$

in which $U_{t,l}$, $U_{f,l}$, and $\Theta_{f,l}$ are the frequency domain representations of the displacements $u_{1,n}$, $u_{f,n}$, and $\theta_{f,n}$. The forces generated by the impedance springs at each frequency w_l, represented by $F_{x,l}$ and $F_{\theta,l}$, are thus calculated according to

$$F_{x,l} = \bar{k}_{x,l} U_{f,l} \quad \text{and} \quad F_{\theta,l} = \bar{k}_{\theta,l} \Theta_{f,l} \,. \quad (2.13)$$

Note that the subscript l in (2.13) indicates that the original (continuous) impedance functions $\bar{k}_x$ and $\bar{k}_\theta$ that have been sampled at L frequency points at a spacing of Δ_ω. Throughout this work, this convention is used to differentiate between continuous impedance functions and sampled sequences of impedance data.

2.2.1 Fixed Base Response

Although fixed-base solutions ignore the effects of inertial soil-structure interaction, they are still of value to this study in that they can serve as a baseline from which to highlight the SSI effects. In 1959, Newmark [19], proposed a numerical time-stepping integration scheme for solving differential equations such as the fixed-base equation of motion given in (2.2). This method remains widely used in engineering practice. To apply it, begin by restating Eq. (2.2) at time $n+1$ as

$$m\ddot{u}_{1,n+1} + c\dot{u}_{1,n+1} + ku_{1,n+1} = p_{n+1} \tag{2.14}$$

where

$$p_{n+1} = -m\ddot{u}_{g,n+1}\,. \tag{2.15}$$

Next, use Newmark's relations to express velocity and displacement at time $n+1$ as

$$\dot{u}_{1,n+1} = \dot{u}_{1,n} + (1-\gamma)\Delta_t\ddot{u}_{1,n} + \gamma\Delta_t\ddot{u}_{1,n+1} \tag{2.16}$$

and

$$u_{1,n+1} = u_{1,n} + \Delta_t\dot{u}_{1,n} + \Delta_t^2(\frac{1}{2}-\beta)\ddot{u}_{1,n} + \Delta_t^2\beta\ddot{u}_{1,n+1} \tag{2.17}$$

where Δ_t represents the time step, or difference in time between n and $n+1$, and β and γ are Newmark's integration and damping constants. Substituting (2.16) and (2.17) into (2.14) and solving for acceleration at time $n+1$ yields

$$\begin{aligned}\ddot{u}_{1,n+1} = \hat{m}^{-1}P_{n+1} - c\left[\dot{u}_{1,n} + (1-\gamma)\Delta_t\ddot{u}_{1,n}\right] \\ - k\left[u_{1,n} + \Delta_t\dot{u}_{1,n} + (\frac{1}{2}-\beta)\Delta_t^2\ddot{u}_{1,n}\right]\end{aligned} \tag{2.18}$$

where

$$\hat{m} = m + \gamma \Delta_t c + \beta \Delta_t^2 k \,. \tag{2.19}$$

Equations (2.18), (2.16), and (2.17) may then be iterated, beginning with a set of initial conditions to determine the system's response.

Figure 2.5 displays the fixed-base time-history response calculated using the Newmark method with $\beta = 0.25$ and $\gamma = 0.5$ for the system depicted in Figure 2.2a, when excited by the horizontal ground acceleration depicted in Figure 2.3.

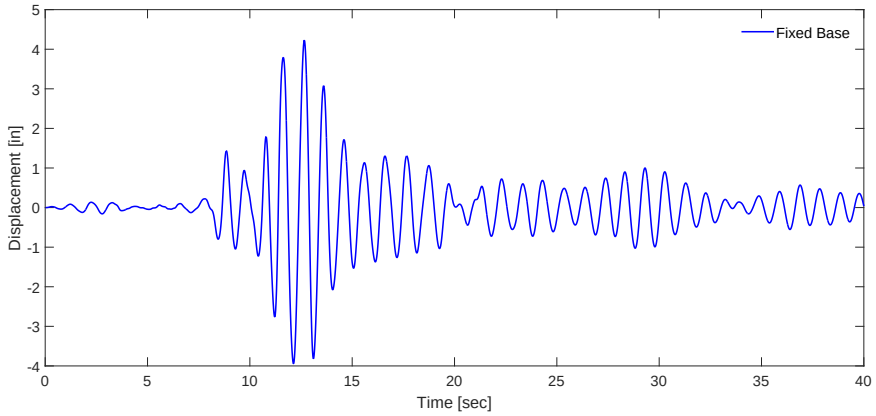

Figure 2.5: *Fixed-base time-history response of SDOF structure subjected to horizontal ground acceleration.*

The response yields a maximum horizontal displacement of $u_{1,max} = 4.23$ inches. Analysis of this response's Fourier amplitude spectrum, shown in Figure 2.6, yields a predominant period of $T_p = 0.97$ seconds. These fixed base values will serve as a baseline for the following substructure analyses.

2.2.2 Substructure Frequency Domain Response

To determine the time-history response of the substructure model in the frequency domain, begin by considering the force generated by the horizontal foundation

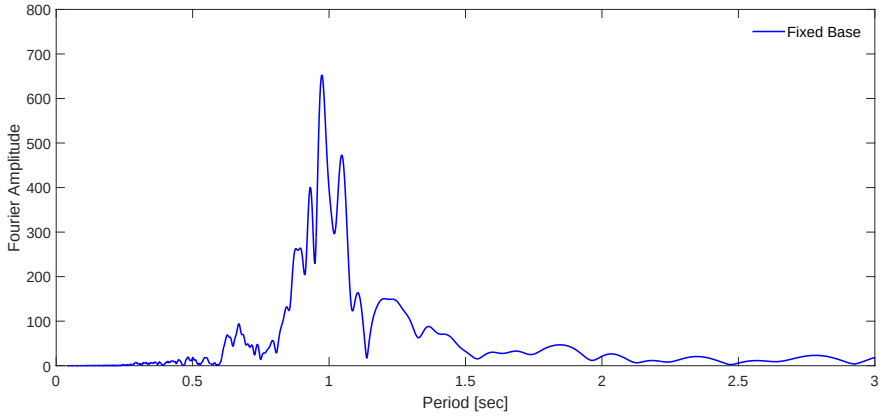

Figure 2.6: *Fourier amplitude spectrum of fixed-base response history for SDOF structure subjected to horizontal ground acceleration.*

impedance spring (according to (2.13) and (2.8)):

$$F_{x,l} = \bar{k}_{x,l} U_{f,l} = \frac{8Gr}{2-\nu}[k_{x,l} + i a_{0,l} c_{x,l}] \,. \tag{2.20}$$

For convenience, express this as

$$F_{x,l} = [\hat{k}_{x,l} + i\omega \hat{c}_{x,l}] U_{f,l} \tag{2.21}$$

where

$$\hat{k}_{x,l} = k_{x,l} \frac{2-\nu}{8Gr} \quad \text{and} \quad \hat{c}_{x,l} = c_{x,l} \frac{a_{0,l}(2-\nu)}{\omega 8Gr} \,.$$

Substituting (2.21) and a similar representation of the force generated by the rotational impedance spring into the frequency domain equations of motion found in (2.10) yields

$$\left(-\omega_l^2 \begin{bmatrix} m & 0 & 0 \\ 0 & m_f & 0 \\ 0 & 0 & I_f \end{bmatrix} + i\omega_l \begin{bmatrix} c & -c & -ch \\ -c & c + \hat{c}_{x,l} & ch \\ -ch & ch & ch^2 + \hat{c}_{\theta,l} \end{bmatrix} + \begin{bmatrix} k & -k & -kh \\ -k & k + \hat{k}_{x,l} & kh \\ -kh & kh & kh^2 + \hat{k}_{\theta,l} \end{bmatrix} \right) \begin{Bmatrix} U_{t,l} \\ U_{f,l} \\ \Theta_{f,l} \end{Bmatrix} = - \begin{Bmatrix} m \\ m_f \\ 0 \end{Bmatrix} \ddot{U}_{g,l} \tag{2.22}$$

which may be expressed more compactly as

$$(-\omega^2 \boldsymbol{M} + i\omega \tilde{\boldsymbol{C}} + \tilde{\boldsymbol{K}})\boldsymbol{U}_l = \boldsymbol{P}_l \tag{2.23}$$

iwhere vectors $\boldsymbol{U}_l$ and $\boldsymbol{P}_l$ contain the system displacements and external forces at each frequency point l, and $\boldsymbol{M}$, $\tilde{\boldsymbol{C}}$, and $\tilde{\boldsymbol{K}}$ are referred to as the system's mass, damping and stiffness matrices. The tildes above the damping and stiffness matrices indicating that they include the frequency-dependent foundation impedance terms. Isolating $\boldsymbol{U}_l$ in (2.23) yields

$$\boldsymbol{U}_l = \boldsymbol{H}_l \boldsymbol{P}_l \tag{2.24}$$

in which the term

$$\boldsymbol{H}_l = (-\omega^2 \boldsymbol{M} + i\omega \tilde{\boldsymbol{C}} + \tilde{\boldsymbol{K}})^{-1} \tag{2.25}$$

is typically referred to as the system's transfer function. Thus, determination of the system's displacement response requires multiplication of the external force vector by the system transfer function. The time history response may then be determined by converting the $\boldsymbol{U}_l$ into the time domain.

In summary, the following four steps are required for execution of the frequency domain method:

1. Transformation of the forcing function from the time domain into the frequency domain.

2. Generation of the system's transfer function.

3. Computation of the system's frequency response.

4. Transformation of the frequency response into the time domain.

As the equations of motion are defined for each frequency point l and both the ground motion record $\ddot{u}_{g,n}$ and desired time history response are defined at discrete

time points n, the discrete Fourier transform and its inverse must be used for conversion between the time and frequency domains. Thus

$$\ddot{U}_{g,l} = \mathcal{F}\left[\ddot{u}_{g,n}\right] \quad \text{and} \quad \boldsymbol{u}_n = \mathcal{F}^{-}1\left[\boldsymbol{U}_l\right] \tag{2.26}$$

where $\mathcal{F}[x]$ and $\mathcal{F}^{-}1[X]$ represent the discrete Fourier transform and the inverse discrete Fourier transform respectively.

Figure 2.7 shows the displacement time-history response for the substructure model depicted in Figure 2.2c, calculated using the frequency domain method outlined above. The figure highlights the effects of inertial SSI. In this figure,

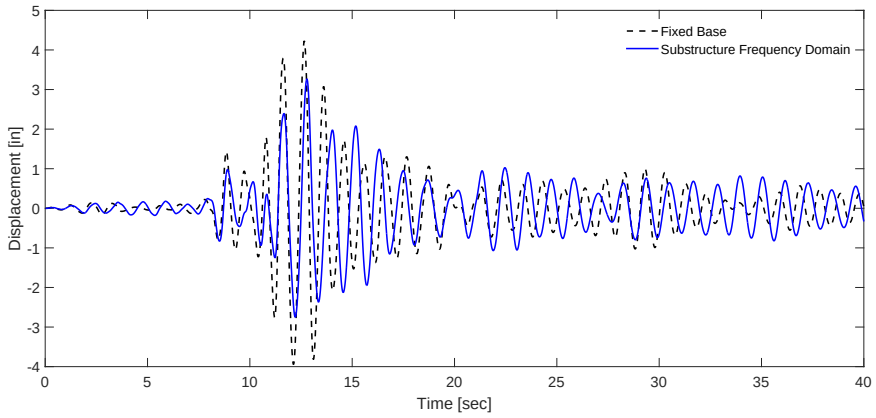

Figure 2.7: *Frequency domain method time-history response of SDOF structure subjected to horizontal ground acceleration.*

the solid line representing the SSI response reveals a maximum displacement of $\tilde{u}_{1,max} = 3.27$ inches compared to a maximum displacement of $u_{1,max} = 4.23$ inches for the fixed base response. The effects of inertial SSI are also visible in the computed response's Fourier amplitude spectrum, which is depicted in Figure 2.8. As expected, the response's period lengthens, in this case from $T_p = 0.97$ seconds to $\tilde{T}_p = 1.17$ seconds.

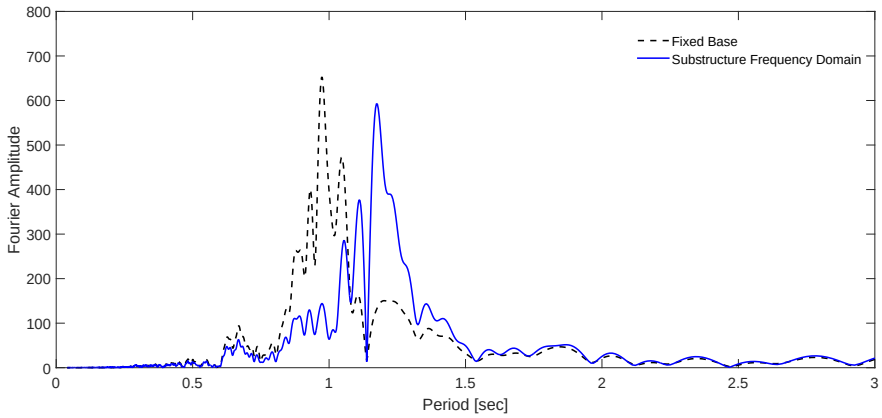

Figure 2.8: *Fourier amplitude spectrum of frequency domain method time-history response of SDOF structure subjected to horizontal ground acceleration.*

2.2.3 Substructure Convolution Response

It is, of course, also possible to solve the equations of motion found in (2.10) by executing the convolution between the impedance functions and the foundation displacements in the time domain. To do so (considering the horizontal), begin by expressing the foundation impedance function at each frequency l as

$$\bar{k}_{x,l} = k_{x,l} + i\omega_l \hat{c}_{x,l} \qquad \text{where} \qquad \hat{c}_{x,l} = \frac{a_{0,l} c_{x,l}}{\omega_l} \tag{2.27}$$

and ω represents frequency in radians per second. Accordingly, the spring force generated by the foundation impedance function may be expressed in the frequency domain as

$$\bar{k}_{x,l} u_{f,l} = (k_{x,l} + i\omega_l \hat{c}_{x,l}) u_{f,l}\,. \tag{2.28}$$

Noting that multiplication in the frequency domain equates to convolution in the time domain, (2.28) may be expressed in the time domain as

$$\bar{k}_{x,n} * u_{f,n} = k_{x,n} * u_{f,n} + \hat{c}_{x,n} * \dot{u}_{f,n} \tag{2.29}$$

where $k_{x,n}$ and $\hat{c}_{x,n}$ represent the inverse discrete Fourier transforms, or impulse responses, of k_l and $\hat{c}_l$ respectively. Expanding the convolutions on the right-hand

side yields

$$\bar{k}_{x,n} * u_{f,n} = k_{x,0}u_{f,n} + \sum_{j=1}^{n-1} k_{x,j}u_{f,n-j} + \hat{c}_{x,0}\dot{u}_{f,n} + \sum_{j=1}^{n-1} \hat{c}_{x,j}\dot{u}_{f,n-j} \,. \tag{2.30}$$

For convenience, the zeroth term of both convolutions are expressed outside their respective summations as at every time step n. When executing a numerical integration scheme to solve the equations of motion, displacements at all past time steps are known quantities. Thus, concerning the right-hand of (2.30), the displacements inside the summations at time steps $n - l$ are known, while those outside at time step n are unknown. This expression, along with a similar representation of the force generated by the rotational impedance may then be substituted into (2.10) to yield the modified equations of motion

$$\begin{bmatrix} m & 0 & 0 \\ 0 & m_f & 0 \\ 0 & 0 & I_f \end{bmatrix} \begin{Bmatrix} \ddot{u}_{1,n} \\ \ddot{u}_{f,n} \\ \ddot{\theta}_{f,n} \end{Bmatrix} + \begin{bmatrix} c & -c & -ch \\ -c & c + \hat{c}_{x,0} & ch \\ -ch & ch & ch^2 + \hat{c}_{\theta,0} \end{bmatrix} \begin{Bmatrix} \dot{u}_{1,n} \\ \dot{u}_{f,n} \\ \dot{u}_{\theta,n} \end{Bmatrix} + \begin{bmatrix} k & -k & -kh \\ -k & k + k_{x,0} & kh \\ -kh & kh & kh^2 + k_{\theta,0} \end{bmatrix} \begin{Bmatrix} u_{1,n} \\ u_{f,n} \\ \theta_{f,n} \end{Bmatrix} = \begin{Bmatrix} -m \\ -m_f \\ 0 \end{Bmatrix} \ddot{u}_{g,n} - \begin{Bmatrix} 0 \\ \sum_{j=1}^{n-1} \hat{c}_{x,j}\dot{u}_{f,n-j} + \sum_{j=1}^{n-1} k_{x,j}u_{f,n-j} \\ \sum_{j=1}^{n-1} \hat{c}_{\theta,j}\dot{\theta}_{f,n-j} + \sum_{l=1}^{n-1} k_{\theta,j}\theta_{f,n-j} \end{Bmatrix} \tag{2.31}$$

where the unknown displacement terms (time step n) are grouped on the left-hand side inside the structural stiffness and damping matrices and the known terms (time steps $n - l$) are grouped on the left-hand side. In this form, the

equations of motion may now be solved via Newmark's numerical integration technique outlined in §2.2.1.

2.2.3.1 Uncorrected Convolution Response

Figure 2.9 displays the time history response for the soil-foundation-structure system depicted in Figure 2.2. Also plotted for reference are the fixed base and rep-

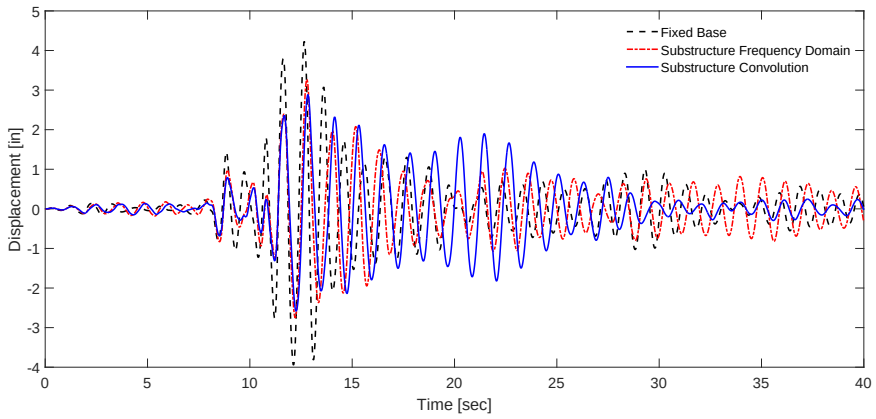

Figure 2.9: *Time history response of SDOF system computed using uncorrected convolution solution.*

resentative frequency responses. Note that although the maximum displacement of the convolution response (3.33 inches) is closer to that of the frequency domain response than that of the fixed base response, its general trend deviates significantly from the frequency domain solution. These differences are further apparent in the Fourier amplitude spectra depicted in Figure 2.10. From these spectra, it is clear that the convolution response contains significant errors as compared to its frequency domain counterpart. These errors are resulting from inaccuracies during the inverse discrete Fourier transform of the foundation impedance functions due to the phenomenon known as time domain leakage.

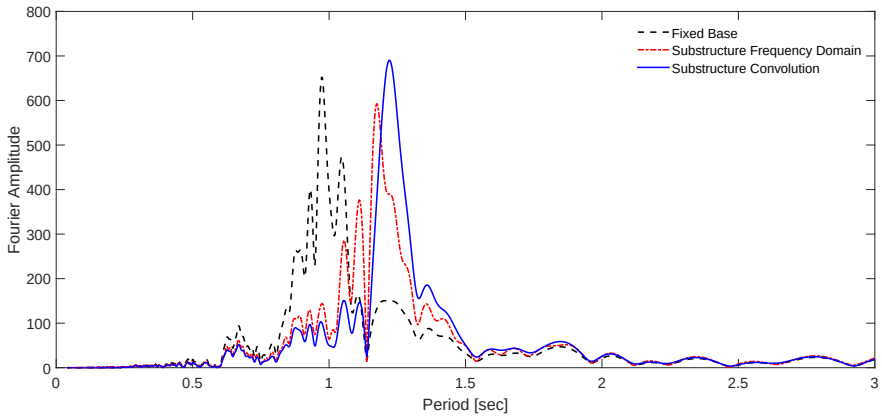

Figure 2.10: *Fourier amplitude spectrum of convolution method time-history response of SDOF structure subjected to horizontal ground acceleration.*

2.2.3.2 Time Domain Leakage

The inverse discrete Fourier transform requires knowledge of frequency data over the interval $-\infty \leq \omega \leq \infty$. Unfortunately, impedance data is often band-limited, or only defined over a finite interval such as $0 \leq a_0 \leq 8$. Application of the IDFT to band-limited frequency data can lead to a non-causal time domain impedance realization where current displacement depends on future, as well as past, displacements.

Figure 2.11 demonstrates this phenomenon. Pictured are the corrected and uncorrected impulse responses of the real component of the rocking foundation impedance. The uncorrected impulse response is clearly non-causal. It contains significant non-zero stiffness values at negative time steps. To be viable for use with a time-stepping numerical integration scheme, such a response must be adjusted to be made causal. The most straightforward (and often the most inaccurate) method of doing this involves simply truncating, or setting equal to zero, the non-causal portion of the time domain impedance realization. Other methods range from conditioned IDFTs—such as those proposed by Paronesso and

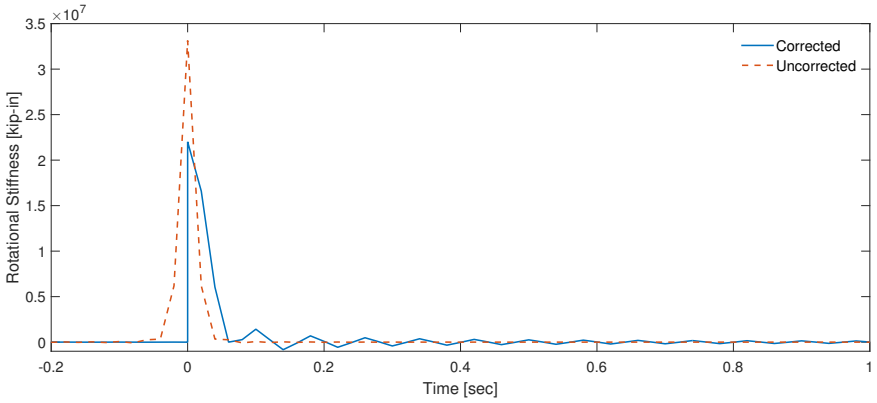

Figure 2.11: *Corrected and uncorrected impulse responses of the real component of rocking foundation impedance.*

Wolf [20] or Hayashi and Katukura [21]—that modify application the IDFT in such a manner as to yield a causal result, to curve-fitting solutions—such as that offered by Nakamura [22] that avoid the IDFT altogether.

The present work uses a modified version of an iterative technique that is borrowed from the signal processing community as outlined in the following section.

2.2.3.3 Causality Correction

The causality correction adopted for this work is based on a method developed Luo and Chen for extraction of causal time domain parameters based on band-limited frequency domain data [23]. In general terms, the method involves successive iterations of the IDFT and DFT, over a frequency range extended beyond that over which the original frequency data is defined. During each iteration, causality is enforced and adjustments are applied both within and outside the original frequency domain. The iterations terminate when the DFT of the impulse response of the adjusted data is within a desired tolerance of the original frequency data over the original range of interest.

The original method by Luo and Chen is modified by here, because the impulse

responses in (2.29) are generated from real, as opposed to complex, data.

To demonstrate the correction technique, consider the case of a notional band-limited data sequence Y_l. Assume this sequence contains real-valued data at discrete frequencies l from zero to some cutoff frequency ω_c, after which it assumes zero values up to a maximum frequency of ω_L. Begin by applying the IDFT to compute the sequence's impulse response:

$$y_n = \mathcal{F}^{-1}[Y_l]\,. \tag{2.32}$$

Next, compute a causal approximation of this impulse response by setting all values occurring at negative time steps to zero according to:

$$\hat{y}_n = y_n \mathcal{H}_n \tag{2.33}$$

where $\mathcal{H}_n$ is a Heaviside function defined as

$$\mathcal{H}_n = \begin{cases} 0 & \text{if } \; n < 0\,, \\ 1 & \text{if } \; n \geq 0\,. \end{cases} \tag{2.34}$$

Then transform this causal approximation back into the frequency domain using the DFT to yield an approximation of the original sequence Y_l,

$$\hat{Y}_l = \mathcal{F}[\hat{y}_n]\,. \tag{2.35}$$

Next compute the difference between the original sequence and approximation:

$$\Delta Y_l = Y_l - \hat{Y}_l\,. \tag{2.36}$$

Use this difference to determine the maximum absolute error between the original sequence and the approximation over the original frequency range of interest ($0 \leq l \leq \omega_c$)

$$\varepsilon = \max\left[\frac{\Delta Y_l}{Y_l}\right]\,. \tag{2.37}$$

If ε is within a desired tolerance, then $\hat{y}_n$ is the desired causal time domain impulse response. If not, then a correction is applied to $\hat{Y}_l$. Note that this correction is

applied differently for values of $\hat{Y}_l$ inside and outside the original frequency band of interest. Inside the band of interest, the correction is

$$\hat{Y}_l = \hat{Y}_l - \Delta\hat{Y}_l \tag{2.38}$$

where

$$\Delta\hat{Y}_l = \alpha_k \Delta Y_l \tag{2.39}$$

and α is a weight factor computed during each iteration as

$$\alpha = \alpha - \varepsilon \tag{2.40}$$

with a seed value of $\alpha = 1$. Outside the frequency range of interest ($\omega_c < l \leq \omega_L$), the correction is

$$\hat{Y}_l = \hat{Y}_l - 0.99\Delta\hat{Y}_{l-1} \tag{2.41}$$

with the constant 0.99 selected to both damp $\hat{Y}_l$ as l approaches L and to assure a smooth transition from inside to outside the frequency range of interest. This procedure is summarized in Figure 2.12.

2.2.3.4 Corrected Convolution Solution

Figures 2.13 and 2.14 depict the time-history response and Fourier amplitude spectrum of the convolution solution, computed using the corrected impulse responses of both the horizontal and rocking impulse responses. The corrected convolution response yields a maximum displacement of $\tilde{u}_{1,max} = 3.10$ inches and a predominant period of $\tilde{T}_p = 1.18$ seconds. This result conforms much better to that of the frequency domain solution than its uncorrected counterpart.

Let $\alpha = 1$;
Compute impulse response $y_n = \mathcal{F}^{-1}[Y_l]$;
while *ε is outside desired tolerance* **do**
    Force causality $\hat{y}_n = \mathcal{H}_n y_n$;
    Update frequency response $\hat{Y}_l = \mathcal{F}[\hat{y}_n]$;
    Compute ϵ using (2.37) ;
    Update α using (2.40);
    Correct $\hat{Y}_l$ inside frequency range of interest using (2.38);
    Correct $\hat{Y}_l$ outside frequency range of interest using (2.41);
    Compute impulse response $y_n = \mathcal{F}^{-1}[\hat{Y}_l]$;
end

Figure 2.12: *Algorithm to estimate causal impulse response from band-limited frequency data.*

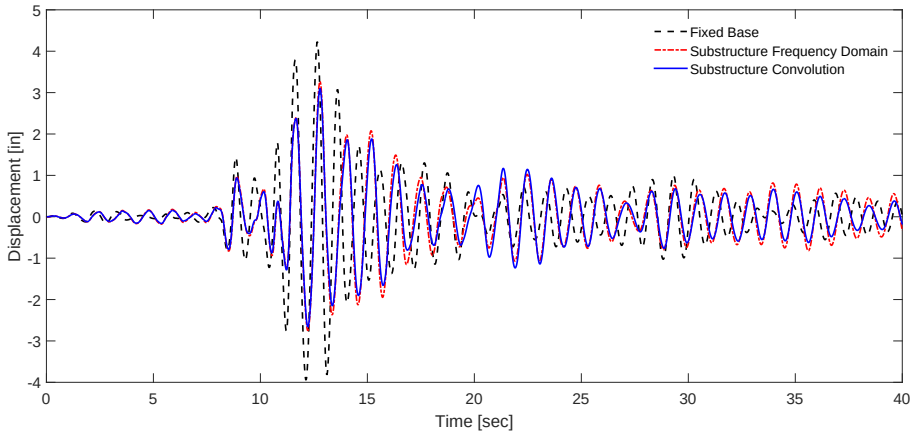

Figure 2.13: *Time history response of SDOF system computed using convolution of corrected impulse responses.*

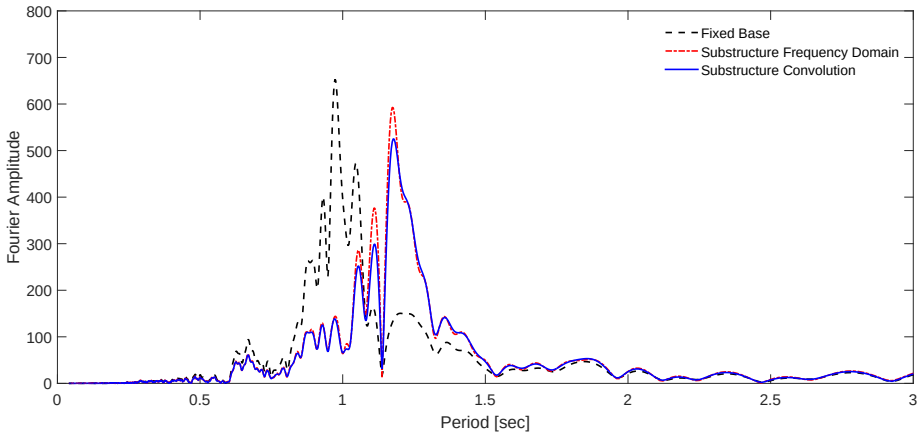

Figure 2.14: *Fourier amplitude spectrum of convolution solution computed using corrected impulse responses.*

2.2.4 Substructure Representative Frequency Response

Perhaps the most popular method currently used in engineering practice for conducting the third step of the substructure method involves removing frequency dependence from the foundation impedance functions by evaluating them at some representative frequency. This is often taken as the structure's first mode flexible-base natural frequency [7]. In the case of the structure depicted in Figure 2.2, the flexible-base period is computed via

$$\tilde{T} = T\sqrt{1 + \frac{k}{\bar{k}_{x,r}} + \frac{kh^2}{\bar{k}_{\theta,r}}} \tag{2.42}$$

in which $\bar{k}_{x,r}$ and $\bar{k}_{\theta,r}$ represent the scalar-sampled versions of $\bar{k}_x$ and $\bar{k}_\theta$. As the former are frequency-dependent, this calculation requires a brief iterative procedure, such as that outlined in Figure 2.15.

An alternative method, offered by Ghannad et al. [16], uses an eigenvalue analysis to determine the flexible-base period. This procedure is outlined in Figure 2.16. For the system in Figure 2.2, both methods result in a flexible-base period of $\tilde{T}_p = 1.69$ seconds. Evaluating the foundation impedance functions

```
1 Assume initial value of flexible-base period T̃;
2 while T̃ is outside a desired tolerance do
3 |   evaluate foundation impedance functions k̄_x and k̄_θ at assumed value of
  |   T̃;
4 |   update T̃ using (2.42);
5 end
```

Figure 2.15: *Standard method for estimation of the flexible-base period.*

```
1 Assume initial value of flexible-base period T̃;
2 while T̃ is outside a desired tolerance do
3 |   evaluate foundation impedance functions k̄_x and k̄_θ at assumed value of
  |   T̃;
4 |   determine eigenvalues of equations of motion as stated in (2.10) using
  |   sampled impedance values k̄_{x,r} and k̄_{θ,r};
5 |   update T̃ using period corresponding to minimum eigenvalue;
6 end
```

Figure 2.16: *Standard method for estimation of the flexible-base period.*

at the frequency (in radians) corresponding to this period yields scalar-valued impedances of $\bar{k}_{x,r} = 3.88(10)^3 + 1.87(10)^2 i$ kips/inch and $\bar{k}_{\theta,r} = 4.65(10)^7 + 2.25(10)^6 i$ kip-inches. These values may then be inserted into (2.10), leaving a set of equations of motions that are solely dependent on time, and may be numerically integrated to determine the system's response history.

Figure 2.17 adds the representative frequency response history analysis of the soil-foundation-structure system depicted in Figure 2.2 to those obtained using the

fixed-base and frequency domain methods, along with these computed responses' Fourier amplitude spectra. Note the general agreement with the frequency domain response in both figures. The representative frequency method yields a maximum displacement of $\tilde{u}_{1,max} = 3.33$ inches and a predominant period of $\tilde{T}_p = 1.17$ seconds, which closely match the values computed using the frequency domain.

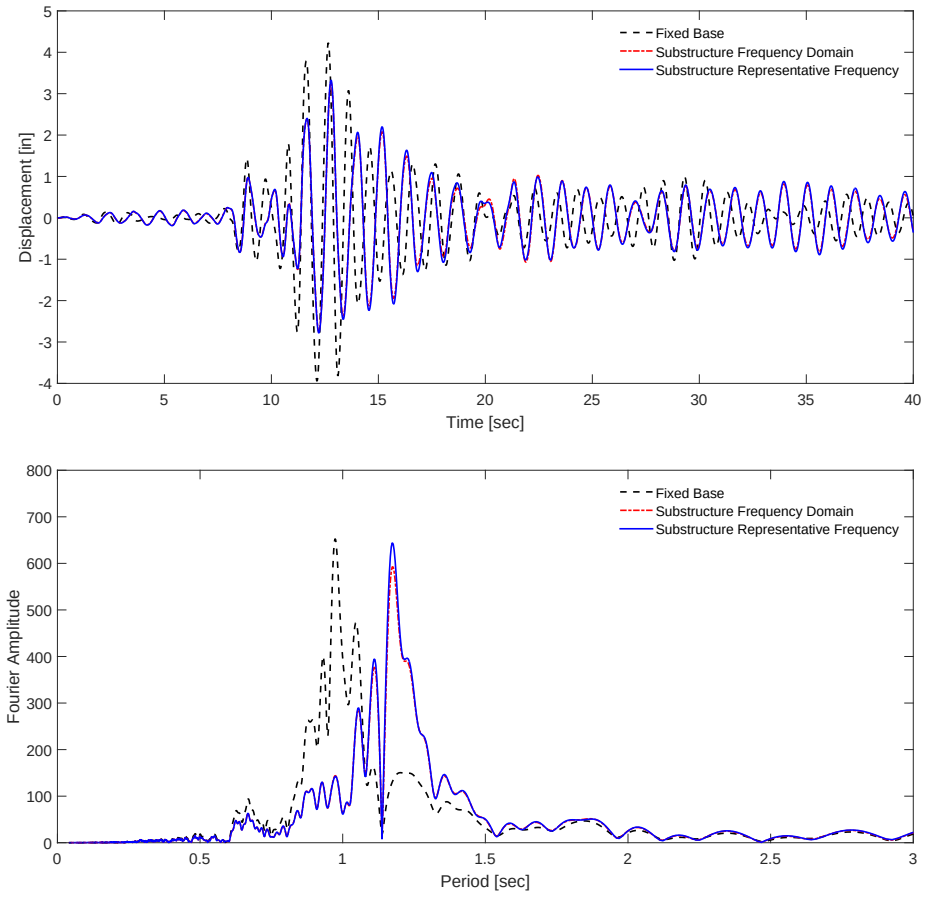

Figure 2.17: *Representative frequency response-history analysis of an SDOF structure subjected to horizontal ground acceleration (top) and the Fourier amplitude spectra of these responses (bottom).*

2.2.5 Substructure Lumped Parameter Model

The final state-of-practice method in this investigation is the lumped parameter—a.k.a., the monkey tail—model. As mentioned in §2.1.3, this method seeks to remove frequency dependence from the foundation impedance functions through the addition of internal degrees of freedom that contain notional springs, dashpots, and masses. The springs represent the system's static stiffness for each direction of foundation movement. The values of the masses and dashpots are determined through a process that includes approximating the impedance functions using a ratio of complex polynomials, as outlined in Appendix B of Wolf's book: *Foundation Vibration Analysis Using Simple Physical Models* [24]. The most basic, or fundamental, lumped parameter model for horizontal and rocking motion is show in Figure 2.18.

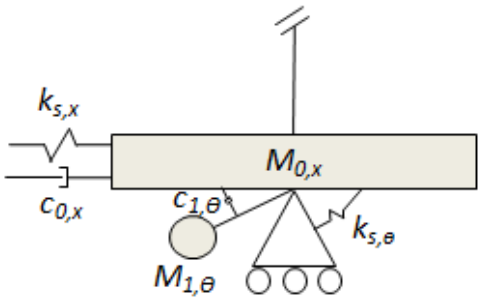

Figure 2.18: *Fundamental lumped parameter model for rocking and horizontal motion of rigid disk resting on elastic half-space.*

The static stiffness are calculated using

$$k_{s,x} = \frac{8Gr}{2-\nu}\,, \tag{2.43a}$$

$$k_{s,\theta} = \frac{8Gr^3}{3-3\nu}\,. \tag{2.43b}$$

These are identical to the leading terms of Equations (2.8) and (2.9) as Wolf used Veletsos and Verbic's impedance functions for his rigid disk on uniform half-space formulations. The masses and dashpots are calculated according to

$$c_{0,j} = \frac{r}{V_s}\gamma_{0,j}k_{s,j} \tag{2.44a}$$

$$c_{1,j} = \frac{r}{V_s}\gamma_{1,j}k_{s,j} \tag{2.44b}$$

$$m_{0,j} = \frac{r^2}{V_s^2}\mu_{0,j}k_{s,j} \tag{2.44c}$$

$$m_{1,j} = \frac{r^2}{V_s^2}\mu_{1,j}k_{s,j} \tag{2.44d}$$

where j represents the foundation displacement directions x or θ and the coefficients $\gamma_{0,j}$, $\gamma_{1,j}$, $\mu_{0,j}$, and $\mu_{1,j}$ are calculated according to Table 2.2.

Table 2.2: *Fundamental lumped parameter coefficients for rigid disk resting on uniform half-space.*

j	$\gamma_{0,j}$	$\gamma_{1,j}$	$\mu_{0,j}$	$\mu_{1,j}$
x - Horizontal	$0.78 - .04\nu$	0	0	0
θ - Rocking	0	$0.42 - 0.3\nu^2$	0	$0.34 - 0.2\nu^2$

The equations of motion for the fundamental lumped parameter model asso-

ciated with the system in Figure 2.2 are

$$\begin{bmatrix} m & 0 & 0 & 0 \\ 0 & m_{0,x} & 0 & 0 \\ 0 & 0 & m_{1,\theta} & 0 \\ 0 & 0 & 0 & m_{0,\theta} \end{bmatrix} \ddot{\boldsymbol{u}}_n + \begin{bmatrix} c & -c & 0 & -ch \\ -c & -c + c_{0,x} & 0 & ch \\ 0 & 0 & c_{1,\theta} & -c_{1,\theta} \\ -ch & ch & -c_{1,\theta} & c_{1,\theta} + ch^2 \end{bmatrix} \dot{\boldsymbol{u}}_n$$

$$\begin{bmatrix} k & -k & 0 & -kh \\ -k & -k + k_{s,x} & 0 & kh \\ 0 & 0 & 0 & 0 \\ -kh & kh & 0 & k_{s,\theta} + kh^2 \end{bmatrix} \boldsymbol{u}_n = - \begin{Bmatrix} m \\ m_{0,x} \\ m_{1,\theta} \\ m_{0,\theta} \end{Bmatrix} \ddot{u}_{g,n} \quad (2.45)$$

where

$$\boldsymbol{u}_n = \begin{Bmatrix} u_{t,n} & u_{f,m} & \theta_{1,n} & \theta_{f,n} \end{Bmatrix}^T$$

$$\dot{\boldsymbol{u}}_n = \begin{Bmatrix} \dot{u}_{t,n} & \dot{u}_{f,m} & \dot{\theta}_{1,n} & \dot{\theta}_{f,n} \end{Bmatrix}^T$$

$$\ddot{\boldsymbol{u}}_n = \begin{Bmatrix} \ddot{u}_{t,n} & \ddot{u}_{f,m} & \ddot{\theta}_{1,n} & \ddot{\theta}_{f,n} \end{Bmatrix}^T .$$

Applying the system parameters from Table 2.1 and numerically integrating (2.45) using $\beta = 0.25$ and $\gamma = 0.5$ yields the response history. The lumped parameter model's computed time-domain response is shown together with the fixed base model and frequency domain solutions Figure 2.19. The same figure also displays the Fourier spectra of these responses.

The lumped parameter method yields a maximum displacement of $u_{1,max} = 3.32$ inches and a predominant period of $\tilde{T}_p = 1.17$ seconds. As with the representative frequency method, these values closely match those obtained in the frequency domain.

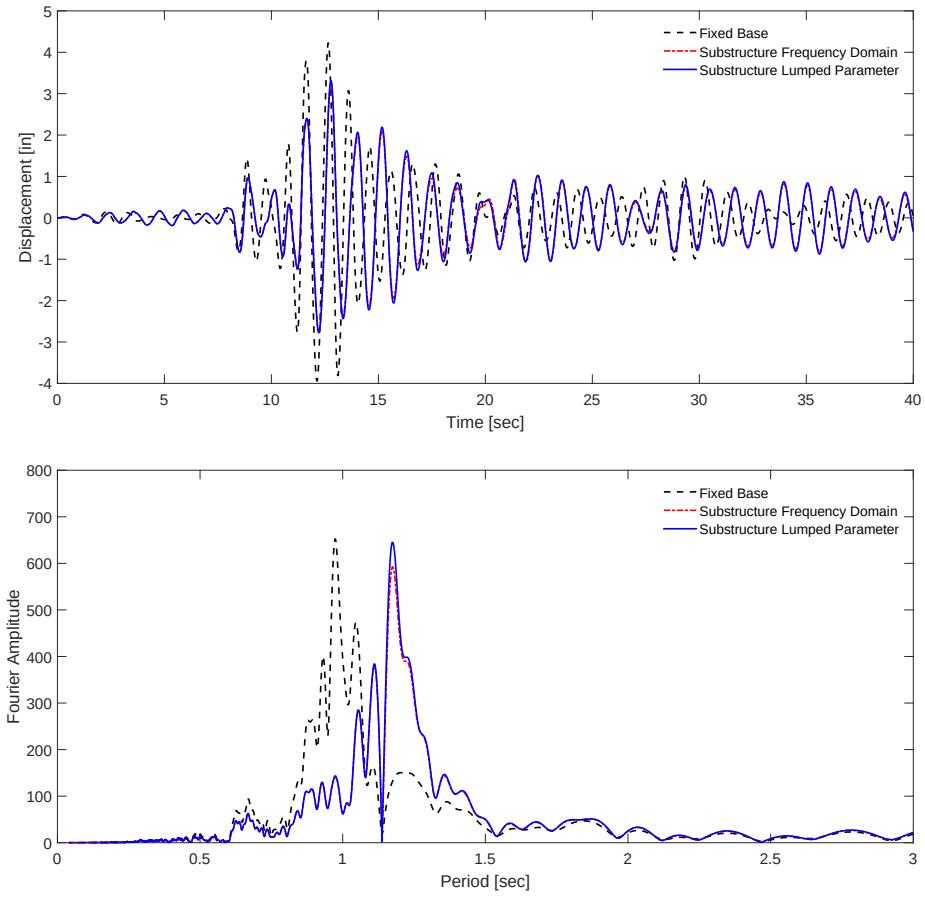

Figure 2.19: *Lumped parameter model response history of SDOF system (top) and its corresponding Fourier amplitude spectrum (bottom); along with the same for the fixed base model and frequency domain solutions.*

2.2.6 Comparison of Methods

Table 2.3 compares the maximum structural displacement and predominant periods for all four methods investigated in this chapter. All substructure methods yield the same period elongation of ~ 0.2 seconds as compared to the fixed base predominant period. All methods also offer an $\sim 8\%$ reduction in reduction in maximum structural displacement.

Table 2.3: *Comparison of time-history response parameters for SDOF system subjected to horizontal ground motion.*

Model	Predominant Period [sec]	Max. Structural Displacement [in]
Fixed-Base	0.97	4.23
Frequency Domain	1.17	3.27
Corrected Convolution	1.18	3.10
Representative Frequency	1.17	3.33
Lumped Parameter	1.17	3.32

CHAPTER 3

The Discrete-Time Filter Method

3.1 Safak's Idea

In 2006 Erdal Safak, then a researcher for the United States Geological Survey (USGS), proposed an innovative means of incorporating frequency-dependent foundation impedance functions into time domain analyses. His idea was to use signal processing theory to approximate the spring force generated by impedance functions as discrete-time digital filters [25]. Such filters are essentially mathematical tools that convert inputs into desired outputs. Safak proposed using present and past values of foundation displacement, coupled with past values of spring force as the inputs to predict, as output, the current value of force generated by the impedance function. Accordingly, in the time domain, the spring force generated in the impedance function $\bar{k}_n$ would take the form

$$\bar{k}_n * u_{f,n} \approx f_n = b_0 u_{f,n} + b_1 u_{f,n-1} + \cdots + b_j u_{f,n-j} - a_1 f_{n-1} - \cdots - a_j \; f_{n-j} \,, \quad (3.1)$$

or more compactly

$$\bar{k}_n * u_{f,n} \approx f_n = b_0 u_{f,n} + \sum_{j=1}^{J} b_p u_{f,n-j} - \sum_{j=1}^{J} a_q f_{n-j} \quad (3.2)$$

where J represents the filter order. Note the similarity between these relations and those for the convolution solution given in (2.29) and (2.30). Equation (3.2) may be inserted in a similar manner into a numerical integration scheme, such as eqs. (2.16) to (2.18), and used to conduct time-history analyses in the time domain in a manner similar to that employed for the convolution solution.

The idea of approximating frequency-dependent impedance functions with recursive relations in the time domain is not new. Indeed, the lumped parameter models discussed in the previous chapter are derived in a similar manner. In their 1989 publication titled *"[r]ecursive evaluation of interaction forces ...,"* Wolf and Motosaka [26] outline a method for determining what they term as *rational approximations* of frequency dependent impedance functions. These rational approximations may be applied as recursive relations or algebraically manipulated into lumped parameter models. Paronesso and Wolf [27] extend this idea by offering further detail on determination of the rational approximations and by extending the method to account for coupled (or matrix) impedances.[1] For the latter, they offer two methods: the first being to approximate each element of the impedance matrix with a separate rational expression; the second being a means of diagonalizing the impedance matrices prior to approximation. Ruge et al. [28] offer an alternative method of deriving rational approximations for impedance matrices using a multi-variable approach. Du and Zhao [29] add a condition to Wolf's process that assures a stable approximation.

The rational approximations yielded by all these aforementioned studies are derived using *continuous frequency*. As such, they yield *continuous-time* filters, and thus, before they can be used as recursive relations within a numerical integration scheme, they must be transformed into discrete-time filters. In 2008, Du et al. [30] offered a means of doing so through application of the bilinear transform. The major difference between these works and the method proposed by Safak is that Safak's method executes the approximation using discrete frequency, thus directly yielding discrete-time filters and avoiding the need to apply the bilinear transform.

[1] For further details on coupled impedances see §4.4

3.2 Coefficient Estimation

Algorithms for estimation of discrete-time recursive filter coefficients using magnitude and phase data are abound in signal processing, control systems, and system identification literature. Many are based on the least-squares method of complex curve fitting outlined by Levy in his 1959 work *Complex Curve Fitting* [31]. What follows is a discrete-time implementation of Levy's method demonstrated using a horizontal impedance function. To begin, note that the Z-transform follows the rule

$$X(z) = \mathbb{Z}\{x_n\} = \sum_{n=0}^{\infty} x_n z^{-n} \quad \text{where} \quad z = e^{i\Omega_l} \quad \text{and} \quad i = \sqrt{-1} \tag{3.3}$$

and is subject to linearity and time-shift properties as follows

$$\mathbb{Z}\{c_1 x_{1,n} + c_2 x_{2,n}\} = c_1 X_1(z) + c_2 X_2(z) \quad \text{and} \quad \mathbb{Z}\{x_{n-k}\} = z^{-k} X(z)\,. \tag{3.4}$$

Using (3.3) and (3.4) the Z-transform of both sides of (3.1) is (with the subscript x dropped for brevity)

$$\bar{k}_l \boldsymbol{U}(z) \approx \boldsymbol{F}(z) = b_0 + b_1 \boldsymbol{U}(z) z^{-1} + \cdots + b_j \boldsymbol{U}(z) z^{-j} - a_1 \boldsymbol{F}(z) z^{-1} - \cdots - a_j \boldsymbol{F}(z) z^{-j}\,. \tag{3.5}$$

At this point, it is important to differentiate between continuous frequency, represented in this work by the Greek symbol (ω), and discrete frequency which will be represented by (Ω). Continuous frequency, over which impedance functions are typically defined, takes values from $0 \to \pm\infty$. Sequences of continuous frequency samples are mapped to sequences of discrete frequency samples over within the interval $0 \to \pm\pi$ according to

$$\Omega_l = 2 \arctan \frac{\omega_l}{2 f_s} \tag{3.6}$$

where f_s denotes sampling frequency, which is equal to twice the maximum frequency, in Hertz, over which the impedance function is defined [32]. Note that the

selection of a sampling frequency equal to the inverse of time step (Δ_t) ensures the domain of the impedance function covers the entirety of the domain of the response's frequency content. Rearranging (3.5) to isolate the impedance $\bar{k}_l$ on the left-hand side leads (with the subscript l now dropped for brevity) to

$$\bar{k} \approx \frac{\boldsymbol{F}(z)}{\boldsymbol{U}(z)} = \frac{b_0 + b_1 z^{-1} + \cdots + b_j z^{-j}}{1 + a_1 z^{-1} + \cdots + a_j z^{-j}} \,. \tag{3.7}$$

Letting N and D represent the complex polynomials in the numerator and denominator of the right-hand side of (3.7), the error between the actual impedance function and its approximation becomes

$$\epsilon = \bar{k} - \frac{N}{D} \,. \tag{3.8}$$

After multiplying both sides by D the square of the absolute value of (3.8) may be expressed as

$$\left|D\epsilon\right|^2 = \left|D\bar{k} - N\right|^2 \,. \tag{3.9}$$

Summing (3.9) over all discrete frequencies, Ω_l yields

$$E = \sum_{l=1}^{L} \left|D\epsilon\right|^2 = \sum_{l=1}^{L} \left|D\bar{k} - N\right|^2 \tag{3.10}$$

where L represents the total number of discrete frequencies. The coefficients b_j and a_j can now be found by minimizing E. To do so, partial derivatives of E with respect to b_j and a_j are evaluated and set equal to zero, as in

$$\begin{aligned}
\tfrac{\partial E}{\partial a_1} &= \textstyle\sum_{l=1}^{L} 2(D\bar{k} - N)(z^{-1}\bar{k}) = 0 \\
&\vdots \\
\tfrac{\partial E}{\partial a_j} &= \textstyle\sum_{l=1}^{L} 2(D\bar{k} - N)(z^{-j}\bar{k}) = 0 \\
\tfrac{\partial E}{\partial b_0} &= \textstyle\sum_{l=1}^{L} 2(D\bar{k} - N)(z^{0}) = 0 \\
\tfrac{\partial E}{\partial b_1} &= \textstyle\sum_{l=1}^{l} 2(D\bar{k} - N)(z^{-1}) = 0 \\
&\vdots \\
\tfrac{\partial E}{\partial b_j} &= \textstyle\sum_{l=1}^{l} 2(D\bar{k} - N)(z^{-j}) = 0
\end{aligned} \tag{3.11}$$

and are arranged in matrix form as

$$\boldsymbol{A} \cdot \boldsymbol{B} = \boldsymbol{C} \tag{3.12}$$

where

$$\boldsymbol{A} = 2\sum_{j=1}^{m} \begin{bmatrix} \bar{k}^2 z^{-2} & \cdots & \bar{k}^2 z^{-(j+1)} & -\bar{k} z^{-1} & -\bar{k} z^{-2} & \cdots & -\bar{k} z^{-(j+1)} \\ \vdots & & \vdots & \vdots & \vdots & & \vdots \\ \bar{k}^2 z^{-(1+j)} & \cdots & \bar{k}^2 z^{-2j} & -\bar{k} z^{-j} & -\bar{k} z^{-(j+1)} & \cdots & -\bar{k} z^{-2j} \\ \bar{k} z^{-1} & \cdots & \bar{k} z^{-j} & -z^{0} & -z^{-1} & \cdots & -z^{-j} \\ \bar{k} z^{-2} & \cdots & \bar{k} z^{-(1+j)} & -z^{-1} & -z^{-2} & \cdots & -z^{-(1+j)} \\ \vdots & & \vdots & \vdots & \vdots & & \vdots \\ \bar{k} z^{-(1+j)} & \cdots & \bar{k} z^{-2j} & -z^{-j} & -z^{-(j+1)} & \cdots & -z^{-2j} \end{bmatrix}$$

$$\boldsymbol{B} = \begin{Bmatrix} a_1 \\ \vdots \\ a_j \\ b_0 \\ b_1 \\ \vdots \\ b_j \end{Bmatrix} \qquad \boldsymbol{C} = -2\sum_{l=1}^{L} \begin{Bmatrix} \bar{k}^2 z^{-1} \\ \vdots \\ \bar{k}^2 z^{-j} \\ \bar{k} z^{-1} \\ \bar{k} z^{-1} \\ \vdots \\ \bar{k} z^{-j} \end{Bmatrix} .$$

The filter coefficients (contained in $\boldsymbol{B}$) are estimated by computing the Moore-Penrose inverse of $\boldsymbol{A}$, according to

$$\boldsymbol{B} = \left[\boldsymbol{A}^{\mathrm{T}} \boldsymbol{A} \right]^{-1} \boldsymbol{A}^{\mathrm{T}} \boldsymbol{C} \,. \tag{3.13}$$

3.3 Safak's Examples

In his 2006 paper, Safak demonstrated his method for approximating impedance functions using discrete-time filters through the use of several examples. The following sections reproduce the results of two, a rigid disk resting on an elastic half-space and a rigid disk founded on an elastic soil layer overlying bedrock.

3.3.1 Rigid Disk on Elastic Half-space

Safak's first example sought to approximate the horizontal foundation impedance function for a rigid disk resting on a uniform, elastic soil half-space. Several variations of the impedance function for this foundation/soil geometry exist in the literature. This work already introduced one in §2.2. Safak chose to use a similar version, offered by Veletsos and Wei [10]. As in §2.2, the foundation impedance function takes the form

$$\bar{k}_x = K_x \left[k_x + i a_0 c_x \right] \tag{3.14}$$

where K_x, the impedance function's static stiffness or value at loading frequency of zero, is calculated according to

$$K_x = \frac{8Gr}{2-\nu} \,. \tag{3.15}$$

The stiffness function, k_x, and the damping function, c_x, are depicted in Figure 3.1. Given the values listed in Table 3.1, the static stiffness is evaluated as $K_x = 1399$ kip/in. Application of the complex least-squares algorithm outlined in §3.2 yields the filter coefficients shown in Table 3.2.

Table 3.1: *Soil and foundation values for rigid disk resting on uniform elastic half-space.*

G - Soil Bulk Modulus	2.4285 kip/in^2
V_s - Shear Wave Velocity	1000 ft/sec
ν - Poisson's Ratio	1/3
r - Foundation Radius	10 ft

This result was obtained by first sampling the impedance function $\bar{k}$ is at a total of $L = 100$ frequency values beginning at $\omega_0 = 0$ and ending with $\omega_L = 800$ rad/sec

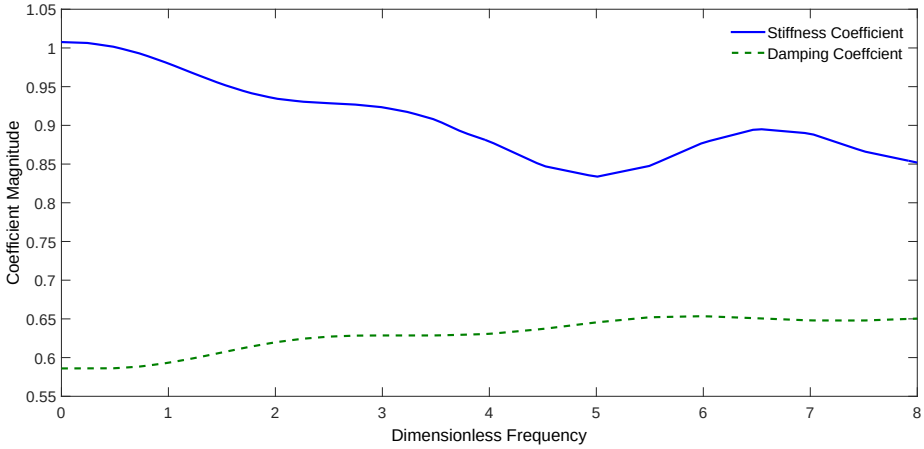

Figure 3.1: *Stiffness and damping coefficients for rigid disk resting on uniform elastic half-space.*

Table 3.2: *Discrete-time recursive filter coefficients approximating foundation impedance function for rigid disk resting on uniform soil half-space.*

j	a_j	b_j $(\times 10^{-4})$
0	$1.0000 + 0.0000i$	$0.5939 + 0.0009i$
1	$-0.4865 - 2.2399i$	$-1.2151 - 1.3415i$
2	$-2.4944 + 0.9438i$	$-0.1234 + 2.672i$
3	$1.1043 + 2.2855i$	$1.6896 - 1.6365i$
4	$1.4206 - 1.1443i$	$-1.2842 + 0.0958i$
5	$-0.6806 - 0.2758i$	$0.3579 + 0.2249i$
6	$0.0637 + 0.1317i$	$-0.0291 - 0.0583i$

(which corresponds to a dimensionless frequency of $a_{0,L} = 8$) to yield the sequence of impedance values $\bar{k}_l$. The sampling frequency (twice ω_L) of $f_s = 254.65$ Hz was used to map the sequence of continuous frequencies ω_l to the sequence of discrete frequencies Ω_l according to (3.6). As seen in Figure 3.2, the fits between the

real and imaginary components of both the original impedance function and this sixth-order filter approximation are quite good across the entire frequency domain. Note in the figure, the imaginary components are normalized by dimensionless frequency a_0.

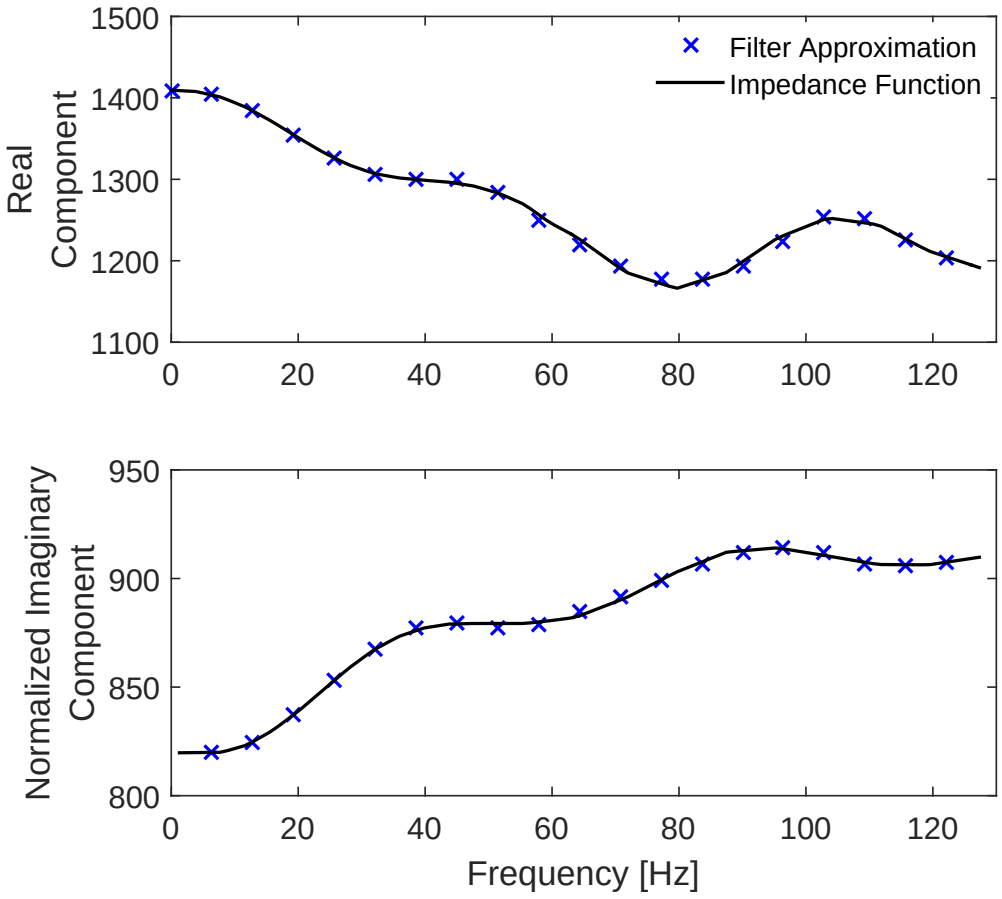

Figure 3.2: *Comparison of foundation impedance function and filter approximation for rigid disk resting on uniform soil half-space.*

3.3.2 Rigid Disk on Elastic Soil Layer Above Bedrock

Another of Safak's examples approximates the horizontal impedance impedance function for a rigid disk foundation resting on an elastic soil layer that overlies

bedrock. The impedance function for this foundation-soil system takes the form

$$\bar{k}_{x,l} = K_x(1 + 2i\xi)\left[k_x + ia_{0,l}c_x\right] . \tag{3.16}$$

In this case, ξ represents damping in the soil layer and h represents the layer's thickness. The static stiffness is defined as

$$K_x = \frac{8Gr}{2-\nu}\left(1 + \frac{r}{2h}\right) . \tag{3.17}$$

The values of the relevant parameters are found in Table 3.3. This impedance function demonstrates considerable variation with respect to frequency as can be seen by the values of the stiffness and damping functions, shown in Figure 3.3.

Table 3.3: *Soil and foundation values for rigid disk resting on uniform elastic half-space.*

G - Soil Bulk Modulus	2.4285 kip/in^2
V_s - Shear Wave Velocity	1000 ft/sec
ν - Poisson's Ratio	1/3
h - Soil Layer Thickness	20 ft
ξ - Soil Layer Damping	0.05
r - Foundation Radius	10 ft

Due to the said variation, a more robust least-squares algorithm is needed to obtain a suitable fit when determining the filter coefficients. The coefficients in Table 3.4 were obtained using an iterative procedure derived by Sanathanan and Koerner [33] that weights the error function (3.10) using the denominator polynomial at each iteration, according to

$$E = \sum_{l=1}^{L} |D\epsilon|^2 \frac{1}{|D|^2} = \sum_{l=1}^{L} \left|D\bar{k}_l - N\right|^2 \frac{1}{|D|^2} . \tag{3.18}$$

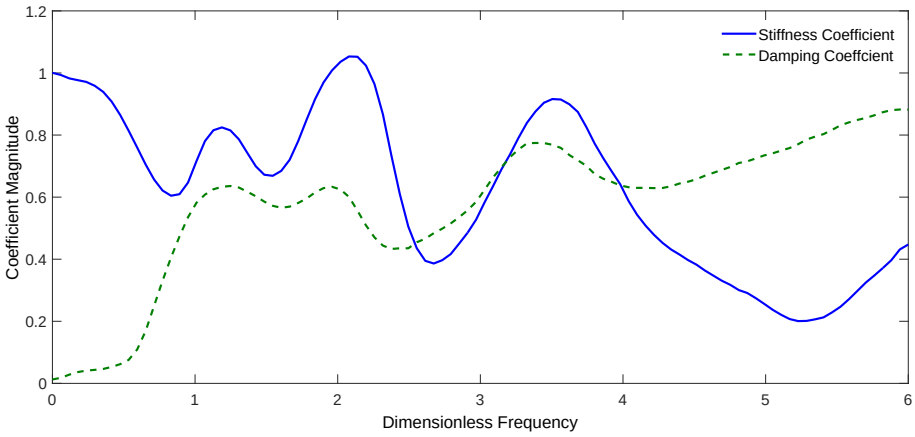

Figure 3.3: *Foundation impedance function stiffness and damping coefficients for rigid disk resting on elastic soil layer above bedrock.*

The first iteration begins with the assumption that all the coefficients $a_q = 1$. The iterations continue until subsequent sets of coefficients vary within a desired tolerance.

Table 3.4: *Coefficients of discrete-time filter approximating foundation impedance function for rigid disk resting on elastic soil layer above bedrock.*

j	a_j	$b_j(10^{-4})$
0	$1.0000 + 0.0000i$	$0.5551 - 0.1012i$
1	$-0.6130 - 3.1801i$	$-1.7562 - 1.4035i$
2	$-4.7253 + 0.9583i$	$0.5262 + 4.0887i$
3	$0.3419 + 5.0870i$	$2.5708 - 4.0988i$
4	$4.1273 - 0.1530i$	$-3.9145 + 1.2880i$
5	$-0.3623 - 2.0078i$	$2.1605 + 1.0797i$
6	$-0.4087 + 0.1878i$	$-0.1967 - 0.8064i$
7	0.0000	$-0.0750 + 0.0952i$

Figure 3.4 depicts a comparison of the impedance function with the filter approximation as with the previous example, the imaginary components are normalized by dimensionless frequency a_0. For this case, a seventh-order filter was required to obtain an adequate fit. Used were $L = 100$ frequency samples from $\omega_0 = 0$ to $\omega_L = 600$ radians per second which corresponds to a sampling frequency of $f_s = 190.99$ hertz.

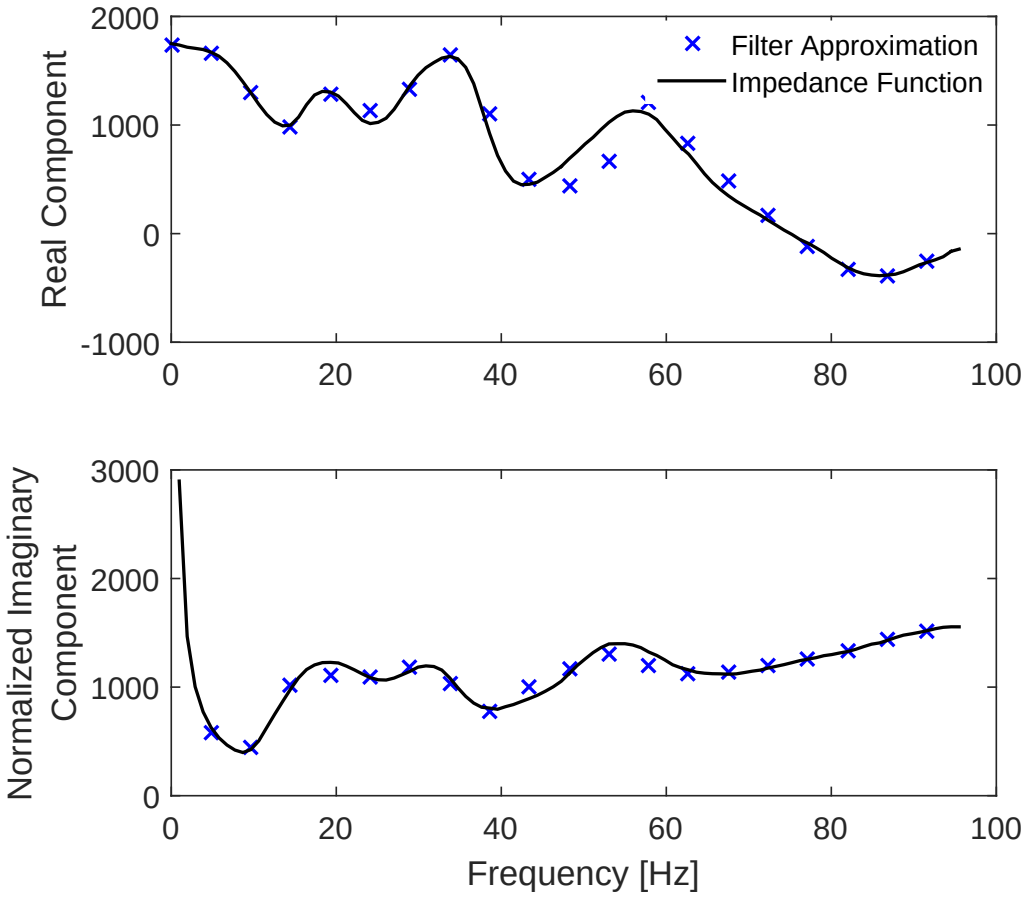

Figure 3.4: *Comparison of foundation impedance function and filter approximation for rigid disk resting on elastic soil layer above bedrock.*

CHAPTER 4

Elastic Implementation

Safak's published work on the filter method concludes with his demonstration of how to approximate various foundation impedance functions with discrete time filters. This chapter builds upon that foundation and achieves the method's implementation for soil-foundation-structure systems subject to elastic structural deformations. This is done using both single and multiple degree-of-freedom (MDOF) structures. The time-history responses obtained are verified through comparison to those generated using the state-of-practice methods outlined in Chapter 2. Also included are detailed analytical and numerical stability analyses of the combined filter-numerical integration algorithm.

4.1 Single Degree of Freedom Systems

Recall the soil-foundation-structure system shown in Figure 2.2. The equations of motion for the substructure model of this system, also given in (2.10), are

$$\begin{bmatrix} m & 0 & 0 \\ 0 & m_f & 0 \\ 0 & 0 & I_f \end{bmatrix} \begin{Bmatrix} \ddot{u}_{1,n} \\ \ddot{u}_{f,n} \\ \ddot{\theta}_{f,n} \end{Bmatrix} + \begin{bmatrix} c & -c & -ch \\ -c & c & ch \\ -ch & ch & ch^2 \end{bmatrix} \begin{Bmatrix} \dot{u}_{1,n} \\ \dot{u}_{f,n} \\ \dot{\theta}_{f,n} \end{Bmatrix} + \begin{bmatrix} k & -k & -kh \\ -k & k & kh \\ -kh & kh & kh^2 \end{bmatrix} \begin{Bmatrix} u_{1,n} \\ u_{f,n} \\ \theta_{f,n} \end{Bmatrix} + \begin{Bmatrix} 0 \\ f_{x,n} \\ f_{\theta,n} \end{Bmatrix} = - \begin{Bmatrix} m \\ m_f \\ 0 \end{Bmatrix} \ddot{u}_{g,n} \quad (4.1)$$

Also recall from Chapter 3 that the filters approximating the spring force generated by the horizontal and rocking foundation impedance functions take the form

$$f_{x,n} \approx b_{x,0} u_{f,n} + \sum_{j=1}^{J} b_{x,p} u_{f,n-j} - \sum_{j=1}^{J} a_{x,j} f_{x,n-j} \tag{4.2}$$

for the horizontal direction and

$$f_{\theta,n} \approx b_{\theta,0} \theta_{f,n} + \sum_{j=1}^{J} b_{\theta,p} \theta_{f,n-p} - \sum_{j=1}^{J} a_{\theta,j} f_{\theta,n-j} \tag{4.3}$$

for the rocking direction. When conducting a time-history analysis using numerical integration, past values of the foundation displacements u_f and θ_f and the spring forces f_f and f_θ are known quantities. Given this, substituting (4.2) and (4.3) into (4.1) and grouping these known values on the right-hand side of the resulting equations yields

$$\begin{bmatrix} m & 0 & 0 \\ 0 & m_f & 0 \\ 0 & 0 & I_f \end{bmatrix} \begin{Bmatrix} \ddot{u}_{t,n} \\ \ddot{u}_{f,n} \\ \ddot{\theta}_{f,n} \end{Bmatrix} + \begin{bmatrix} c & -c & -ch \\ -c & c & ch \\ -ch & ch & ch^2 \end{bmatrix} \begin{Bmatrix} \dot{u}_{t,n} \\ \dot{u}_{f,n} \\ \dot{\theta}_{f,n} \end{Bmatrix}$$
$$+ \begin{bmatrix} k & -k & -kh \\ -k & k + b_{x,0} & kh \\ -kh & kh & kh^2 + b_{\theta,0} \end{bmatrix} \begin{Bmatrix} u_{t,n} \\ u_{f,n} \\ \theta_{f,n} \end{Bmatrix} = - \begin{Bmatrix} m \\ m_f \\ 0 \end{Bmatrix} \ddot{u}_g + \begin{Bmatrix} 0 \\ \hat{f}_{x,n} \\ \hat{f}_{\theta,n} \end{Bmatrix} \tag{4.4}$$

where

$$\hat{f}_{x,n} = \sum_{p=1}^{P} b_{x,p} \theta_{f,n-p} - \sum_{q=1}^{Q} a_{x,q} f_{x,n-q}$$
$$\hat{f}_{\theta,n} = \sum_{p=1}^{P} b_{\theta,p} \theta_{f,n-p} - \sum_{q=1}^{Q} a_{\theta,q} f_{\theta,n-q} \, .$$

Stated in matrix from, these equations of motion become

$$\boldsymbol{M}\ddot{\boldsymbol{u}}_n + \boldsymbol{C}\dot{\boldsymbol{u}}_n + \hat{\boldsymbol{K}}\boldsymbol{u}_n = \hat{\boldsymbol{P}}_n \tag{4.5}$$

where $\boldsymbol{M}$ is the system mass matrix, $\boldsymbol{C}$ is the system damping matrix. The filter adjusted stiffness matrix and force are $\hat{\boldsymbol{K}}$ and $\hat{\boldsymbol{P}}_n$ respectively and the acceleration, velocity, and displacement vectors are likewise $\ddot{\boldsymbol{u}}_n$, $\dot{\boldsymbol{u}}_n$, and $\boldsymbol{u}_n$.

Using these equations of motion, the system's time-history response may now be determined through application of Newmark's numerical time-stepping integration method in a manner similar to that used in §2.2.1 for the fixed-base response. To do so, begin by restating (4.5) at time $n+1$ as

$$\boldsymbol{M}\ddot{\boldsymbol{u}}_{n+1} + \boldsymbol{C}\dot{\boldsymbol{u}}_{n+1} + \hat{\boldsymbol{K}}\boldsymbol{u}_{n+1} = \hat{\boldsymbol{P}}_{n+1}\,. \tag{4.6}$$

Next, recall that displacement and velocity at time $n+1$ are defined by Newmark's Method as

$$\dot{\boldsymbol{u}}_{n+1} = \dot{\boldsymbol{u}}_n + (1-\gamma)\Delta_t\ddot{\boldsymbol{u}}_n + \gamma\Delta_t\ddot{\boldsymbol{u}}_{n+1} \tag{4.7}$$

and

$$\boldsymbol{u}_{n+1} = \boldsymbol{u}_n + \Delta_t\dot{\boldsymbol{u}}_n + \Delta_t^2\left(\frac{1}{2}-\beta\right)\ddot{\boldsymbol{u}}_n + \Delta_t^2\beta\ddot{\boldsymbol{u}}_{n+1} \tag{4.8}$$

where Δ_t represents the time step and β and γ are Newmark's integration and damping constants respectively. Substituting (4.7) and (4.8) into (4.6) and solving for acceleration at time $n+1$ yields

$$\ddot{\boldsymbol{u}}_{n+1} = \tilde{\boldsymbol{M}}^{-1}\hat{\boldsymbol{P}}_{n+1} - \boldsymbol{C}(\dot{\boldsymbol{u}}_n + (1-\gamma)\Delta_t\ddot{\boldsymbol{u}}_n) - \hat{\boldsymbol{K}}(\boldsymbol{u}_n + \Delta_t\dot{\boldsymbol{u}}_n + \left(\frac{1}{2}-\beta\right)\Delta_t^2\ddot{\boldsymbol{u}}_n) \tag{4.9}$$

$$\text{where} \quad \tilde{\boldsymbol{M}} = \boldsymbol{M} + \gamma\Delta_t\boldsymbol{C} + \beta\Delta_t^2\hat{\boldsymbol{K}}\,.$$

Iterating equations (4.7), (4.8), and (4.9) from initial conditions will yield the system's time-history response.

4.1.1 Implementation Example

To demonstrate the procedure outlined in the previous section, once again recall the system depicted in Figure 2.2, the accompanying values listed in Table 2.1, and the input ground motion shown in Figure 2.3. The substructure model of this system contains the horizontal foundation impedance function

$$\bar{k}_x = K_x\left[k_x + ia_0c_x\right] \tag{4.10}$$

where

$$K_x = \frac{8Gr}{2-\nu} \qquad k_x = 1 \qquad c_x = 0.65 \qquad a_0 = \frac{\omega r}{V_s}$$

and the rocking foundation impedance function

$$\bar{k}_\theta = K_\theta \left[k_\theta + i a_0 c_\theta \right] \tag{4.11}$$

where

$$K_\theta = \frac{8Gr^3}{3-3\nu} \qquad k_{\theta,l} = 1 - \frac{\beta_1(\beta_2 a_0)^2}{1+\beta_2 a_0)^2} \qquad c_\theta = \frac{\beta_1\beta_2(\beta_2 a_0)^2}{1+\beta_2 a_0)^2}$$

$$\beta_1 = 0.8 \qquad \beta_2 = 0.5 \qquad a_0 = \frac{\omega r}{V_s}\,.$$

Applying the algorithm outlined in §3.2 to the horizontal impedance function yields the second-order filter coefficients contained in Table 4.1. The magnitude and phase components of both the original impedance function and the filter approximation are shown in Figure 4.1. The fit is quite good across the entire frequency range. It should be noted that the least-squares algorithm returned a negligible imaginary component (on the order of 10^{-12}) for each coefficient, thus producing what is in essence a real filter.

Table 4.1: *Coefficients of discrete-time filters approximating horizontal and rocking impedance functions for rigid disk resting on uniform soil half-space.*

j	$a_{x,j}$	$b_{x,j}$ $(\times 10^3)$	$a_{\theta,j}$	$b_{\theta,j}$ $(\times 10^8)$
1	1.0000	8.9369	$1.0000 + 0.0000i$	$0.4665 + 0.0000i$
2	0.9580	-1.5411	$2.4172 - 0.0023i$	$1.1272 - 0.0011i$
3	-0.0420	0.0490	$1.2505 - 0.0073i$	$0.5827 - 0.0034i$
4			$-0.7505 - 0.0076i$	$-0.3500 - 0.0036i$
5			$-0.5838 - 0.0027i$	$-0.2721 - 0.0012i$

The rocking impedance function was more difficult to approximate. As with the second example in Chapter 2, it required use of the recursive algorithm given

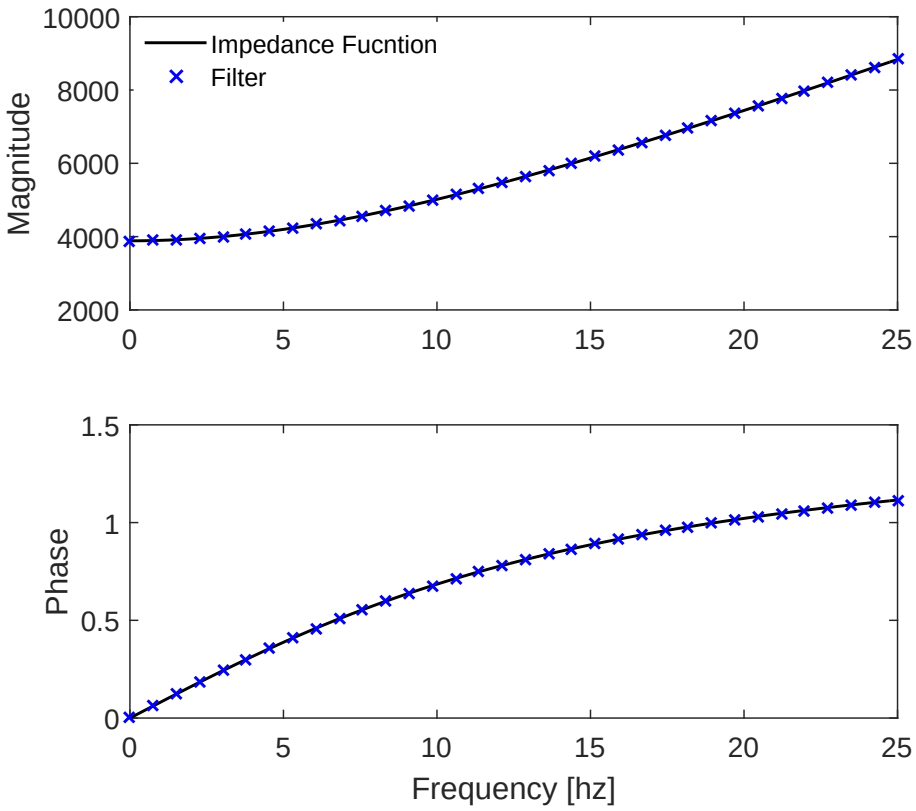

Figure 4.1: *Comparison of foundation impedance function and filter approximation for rigid disk resting on uniform soil half-space.*

by Equation (3.18). Applying this yields the fourth-order filter coefficients also found in Table 4.1. The original rocking impedance function and the filter approximation are shown in Figure 4.2. Notice that the while the fit is generally good over the lower two-thirds of the frequency domain it deteriorates significantly in the upper third, beginning at around 18 Hertz. Fortunately, recalling Figure 2.4, nearly all of the input motion's frequency content is found below this threshold with the majority occurring from 0 to 5 Hertz.

Figure 4.3 shows the time-history response obtained using the filter method compared with both the fixed base response the substructure response computed using the frequency domain method. The filter method's response closely resem-

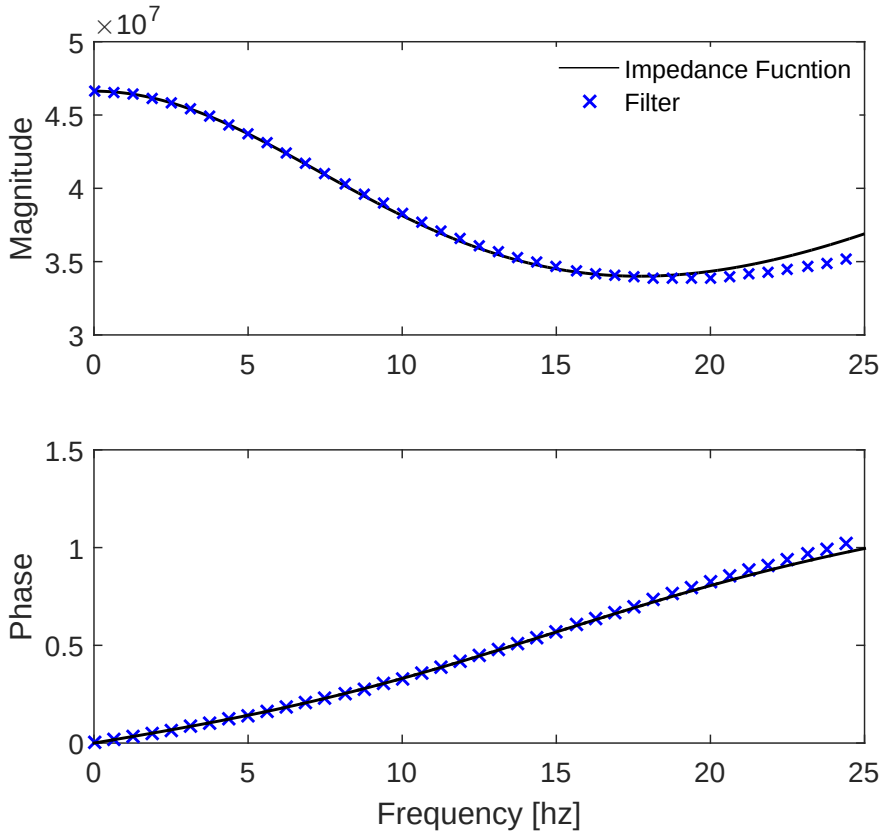

Figure 4.2: *Comparison of rocking foundation impedance function and filter approximation for rigid disk resting on uniform soil half-space.*

bles that obtained using the frequency domain. Table 4.2 contains a comparison of the maximum displacement and predominant period between the three methods.

4.1.2 Results at Various Structure-to-Soil Stiffness Ratios

The so-called *structure-to-soil* stiffness ratio offers engineers a quantifiable metric of a soil-foundation-structure system's susceptibility to inertial soil structure interaction. Defined as

$$\sigma^{-1} = \frac{h}{V_s T} \tag{4.12}$$

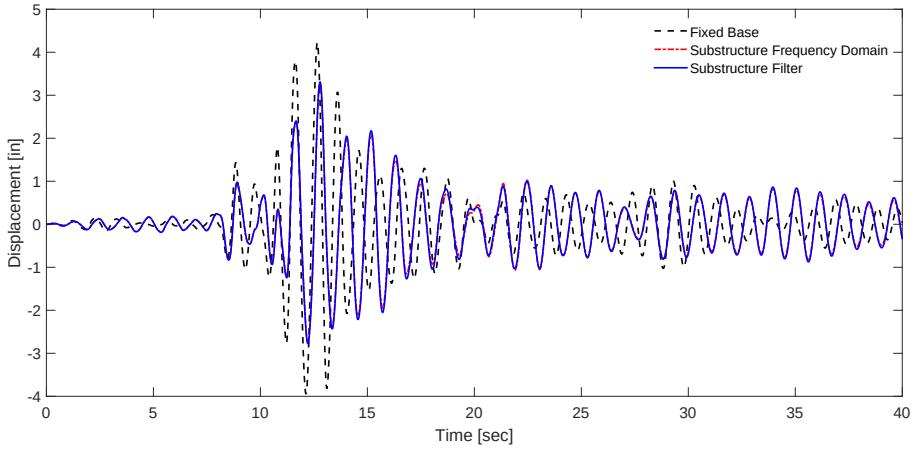

Figure 4.3: *Time history response of SDOF structure with rigid disk foundation resting on uniform half-space.*

Table 4.2: *Response parameters for SDOF system subjected to horizontal ground motion.*

Model	Predominant Period [sec]	Max. Structural Displacement [in]
Fixed-Base	0.97	4.18
Frequency Domain	1.18	3.15
Impedance Filter	1.17	3.31

where r represents foundation radius, V_s represents soil shear wave velocity, and T represents the structure's fundamental period, the lower a system's σ^{-1}, the lower its risk of susceptibility. To wit, a relatively flexible structure founded on rock would have a lower σ^{-1} than a stiff structure founded on soft soil. Thus, to be functional, the impedance filter method should produce responses that approach the fixed base response at low σ^{-1} values and demonstrate the most divergence from the fixed base response at high σ^{-1} values.

Figure 4.4 shows that this is indeed the case. The figure was generated by holding all system parameters constant except shear wave velocity, which was allowed to vary from 300 to 1600 ft/sec. The figure shows that all three impedance-based response calculation methods (frequency domain, representative frequency, and filter) approach the fixed base response at low values of σ^{-1} and diverge from the fixed base response as σ^{-1} increases.

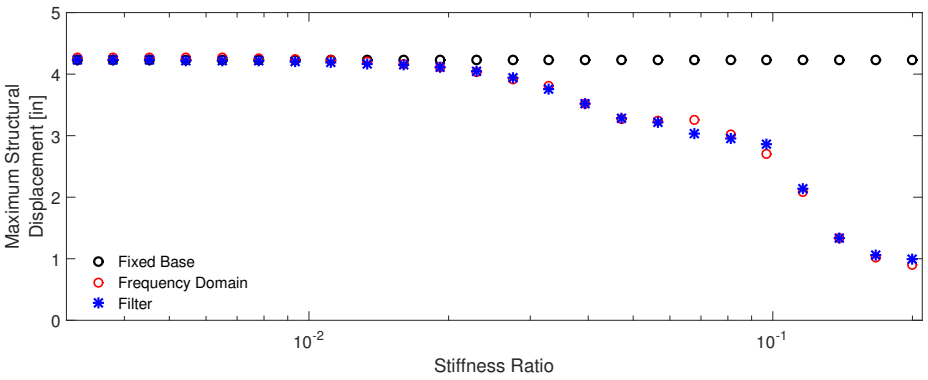

Figure 4.4: *Maximum top story displacement relative to base at varying soil to structure stiffness ratios.*

4.2 Multiple Degree of Freedom Systems

The procedures outlined in §4.1 are easily expanded to accommodate soil-foundation-structure systems in which the structure contains multiple degrees of freedom. To demonstrate this consider the system depicted in Figure 4.5. Figure 4.5(a) contains a shear building with an arbitrary number of stories. The building is founded on a rigid rectangular foundation, which is embedded in a uniform soil half-space. Figure 4.5(b) shows the fixed-base model of the system, and Figure 4.5(c) shows the system's substructure model. The substructure model contains the horizontal foundation impedance function, $\bar{k}_x$, and the rocking impedance function, $\bar{k}_\theta$.

For the fixed-base case, the system's equations of motion may be expressed in

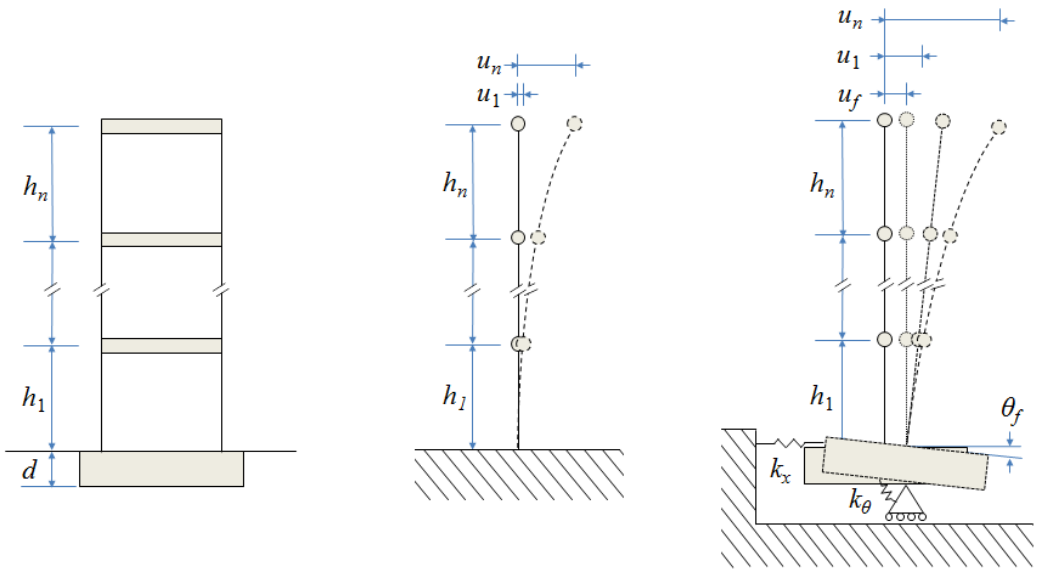

(a) Soil-Foundation-Structure System

(b) Fixed Base Model

(c) Substructure Model

Figure 4.5: *A multiple degree of freedom soil-foundation-structure system with fixed base and substructure models.*

terms of relative displacements as

$$\boldsymbol{M}_s\ddot{\boldsymbol{u}}_{s,n} + \boldsymbol{C}_s\dot{\boldsymbol{u}}_{s,n} + \boldsymbol{K}_s\boldsymbol{u}_{s,n} = \boldsymbol{P}_{s,n} \tag{4.13}$$

where

$$\boldsymbol{u}_{s,n} = \begin{Bmatrix} u_{J,n} \\ u_{J-1,n} \\ \vdots \\ u_2 \\ u_1 \end{Bmatrix} \boldsymbol{M}_s = \begin{bmatrix} m_J & 0 & \dots & 0 & 0 \\ 0 & m_{J-1} & \dots & 0 & 0 \\ \vdots & \vdots & \ddots & 0 & 0 \\ 0 & 0 & 0 & m_2 & 0 \\ 0 & 0 & 0 & 0 & m_1 \end{bmatrix} \quad \boldsymbol{P}_{s,n} = - \begin{bmatrix} m_J \\ m_{J-1} \\ \vdots \\ m_2 \\ m_1 \end{bmatrix} \ddot{u}_{g,n}$$

$$\boldsymbol{K}_s = \begin{bmatrix} k_j & -k_j & \dots & 0 & 0 \\ -k_j & k_j + k_{j-1} & \dots & 0 & 0 \\ \vdots & \vdots & \ddots & -k_3 & 0 \\ 0 & 0 & -k_3 & k_3 + k_2 & -k_2 \\ 0 & 0 & 0 & -k_2 & k_2 + k_1 \end{bmatrix} \quad \text{and} \quad \boldsymbol{C}_s = \frac{2\xi}{\omega_n}\boldsymbol{K}_s$$

with g representing the acceleration due to gravity, ω_n representing the structure's natural frequency, and the subscript s denoting that the respective matrices represent the structure only. Likewise, the equations of motion for the substructure model are

$$\begin{bmatrix} \boldsymbol{M}_s & \boldsymbol{M}_{sf} \\ \boldsymbol{M}_{fs} & \boldsymbol{M}_f \end{bmatrix} \begin{Bmatrix} \ddot{\boldsymbol{u}}_{s,n} \\ \ddot{\boldsymbol{u}}_{f,n} \end{Bmatrix} + \begin{bmatrix} \boldsymbol{C}_s & \boldsymbol{C}_{sf} \\ \boldsymbol{C}_{fs} & \boldsymbol{C}_f \end{bmatrix} \begin{Bmatrix} \dot{\boldsymbol{u}}_{s,n} \\ \dot{\boldsymbol{u}}_{f,n} \end{Bmatrix} + \begin{bmatrix} \boldsymbol{K}_s & \boldsymbol{K}_{sf} \\ \boldsymbol{K}_{fs} & \boldsymbol{K}_f \end{bmatrix} \begin{Bmatrix} \boldsymbol{u}_{s,n} \\ \boldsymbol{u}_{f,n} \end{Bmatrix} + \begin{bmatrix} 0 \\ \boldsymbol{F}_{f,n} \end{bmatrix} = \begin{bmatrix} \boldsymbol{P}_{s,n} \\ \boldsymbol{P}_{f,n} \end{bmatrix} \quad (4.14)$$

where

$$\boldsymbol{M}_{sf} = \boldsymbol{M}_{sf}^\top = \boldsymbol{0} \quad \boldsymbol{M}_f = \begin{bmatrix} m_f & 0 \\ 0 & I_f \end{bmatrix} \quad \boldsymbol{P}_{f,n} = -\begin{bmatrix} m_f \\ \sum m_j h_j \end{bmatrix} \ddot{u}_{g,n} \quad \boldsymbol{u}_{f,n} = \begin{bmatrix} u_{f,n} \\ \theta_{f,n} \end{bmatrix}$$

$$\boldsymbol{C}_{sf} = \boldsymbol{C}_{fs}^\top = \begin{bmatrix} 0 & -c_J h_J \\ 0 & -c_{J-1}h_{J-1} + c_J h_J \\ \vdots & \vdots \\ -c_1 & -c_1 h_1 + c_2 h_2 \end{bmatrix} \boldsymbol{C}_f = \begin{bmatrix} c_1 & 0 \\ 0 & \sum c_j h_j^2 \end{bmatrix} \quad c_j = \frac{2\xi}{\omega_n} k_j$$

$$\boldsymbol{K}_{sf} = \boldsymbol{K}_{fs}^\top = \begin{bmatrix} 0 & -k_J h_J \\ 0 & -k_{J-1}h_{J-1} + k_J h_J \\ \vdots & \vdots \\ -k_1 & -k_1 h_1 + k_2 h_2 \end{bmatrix} \boldsymbol{K}_f = \begin{bmatrix} k_1 + \bar{k}_x & 0 \\ 0 & \sum k_j h_j^2 + \bar{k}_\theta \end{bmatrix}$$

$$\boldsymbol{F}_{f,n} = \begin{bmatrix} f_{x,n} \\ f_{\theta,n} \end{bmatrix}$$

with the subscript f identifying matrices are representing the foundation. Likewise, the subscripts, fs and sf represent foundation-structure coupling matrices.

Adapting these expressions for the filter method yields

$$\begin{bmatrix} \boldsymbol{M}_s & \boldsymbol{M}_{sf} \\ \boldsymbol{M}_{fs} & \boldsymbol{M}_f \end{bmatrix} \begin{Bmatrix} \ddot{\boldsymbol{u}}_s \\ \ddot{\boldsymbol{u}}_f \end{Bmatrix} + \begin{bmatrix} \boldsymbol{C}_s & \boldsymbol{C}_{sf} \\ \boldsymbol{C}_{fs} & \boldsymbol{C}_f \end{bmatrix} \begin{Bmatrix} \dot{\boldsymbol{u}}_s \\ \dot{\boldsymbol{u}}_f \end{Bmatrix} + \begin{bmatrix} \boldsymbol{K}_s & \boldsymbol{K}_{sf} \\ \boldsymbol{K}_{fs} & \hat{\boldsymbol{K}}_f \end{bmatrix} \begin{Bmatrix} \boldsymbol{u}_s \\ \boldsymbol{u}_f \end{Bmatrix} = \begin{bmatrix} \boldsymbol{P}_{s,n} \\ \boldsymbol{P}_{f,n} + \hat{\boldsymbol{F}}_{f,n} \end{bmatrix} \tag{4.15}$$

where

$$\hat{\boldsymbol{K}}_f = \begin{bmatrix} k_1 + b_{x,0} & 0 \\ 0 & \sum k_j h_j^2 + b_{\theta,0} \end{bmatrix} \quad \hat{\boldsymbol{F}}_{f,n} = \begin{bmatrix} \hat{f}_{x,n} \\ \hat{f}_{\theta,n} \end{bmatrix}$$

$$\hat{f}_{x,n} = \sum_{j=1}^{k} b_{x,j} u_{f,n-j} - \sum_{j=1}^{l} a_{x,j} f_{x,n-j}$$

$$\hat{f}_{\theta,n} = \sum_{j=1}^{k} b_{\theta,j} \theta_{f,n-j} - \sum_{j=1}^{l} a_{\theta,j} f_{\theta,n-j} \, .$$

In matrix form, (4.15) is expressed as

$$\boldsymbol{M}\ddot{\boldsymbol{u}}_n + \boldsymbol{C}\dot{\boldsymbol{u}}_n + \hat{\boldsymbol{K}}\boldsymbol{u}_n = \hat{\boldsymbol{P}}_n \tag{4.16}$$

where $\boldsymbol{M}$ contains the mass matrices, $\boldsymbol{M}_s$, $\boldsymbol{M}_{sf}$, $\boldsymbol{M}_{fs}$, and $\boldsymbol{M}_f$ with the damping matrix $\boldsymbol{C}$, the filter-adjusted stiffness matrix $\hat{\boldsymbol{K}}$ and force vector $\hat{\boldsymbol{P}}_n$ and the acceleration, velocity, and displacement vectors $\ddot{\boldsymbol{u}}_n$, $\dot{\boldsymbol{u}}_n$, and $\boldsymbol{u}_n$ assembled in a similar manner. Equation (4.16) may now be used in conjunction with (4.7), (4.8), and (4.9) to determine the system's response history.

4.2.1 Implementation Example

This next example demonstrates use of the filter method to determine the response history of a soil-foundation-structure system with multiple structural degrees of freedom. In doing so, the values found in Table 4.3 are applied to the system

shown in Figure 4.5. The system will be excited by the east-west acceleration record from the 1994 Northridge Earthquake as recorded at California Strong Motion Instrumentation Program Station No. 24538 on the grounds of the Santa Monica City Hall.

Table 4.3: *Multiple degree-of-freedom system model parameters.*

Geology	
G: Soil Bulk Modulus	6.7458 kip/in^2
V_s: Shear Wave Velocity	1100 ft/sec
ν: Poisson's Ratio	1/3
Structure	
n: Number of Stories	3
W: Story Weight	2000 kips
W_f: Foundation Weight	1000 kips
h: Story Height	12 ft
k: Story Stiffness	500 kip/in
ξ: Damping Ratio	0.03
$2B$: Foundation Width	15 ft
$2L$: Foundation Length	20 ft
D: Foundation Embedment	5 ft

During this event, the site felt a maximum horizontal acceleration of $0.29g$. The event's acceleration record and its Fourier amplitude spectrum are plotted in Figure 4.6

In its publication, *Soil-Structure Interaction for Building Structures*, the National Earthquake Hazard Reduction Program (NEHRP) offers foundation impedance functions, originally derived by Pais and Kausel [13], for a rigid rectangular foun-

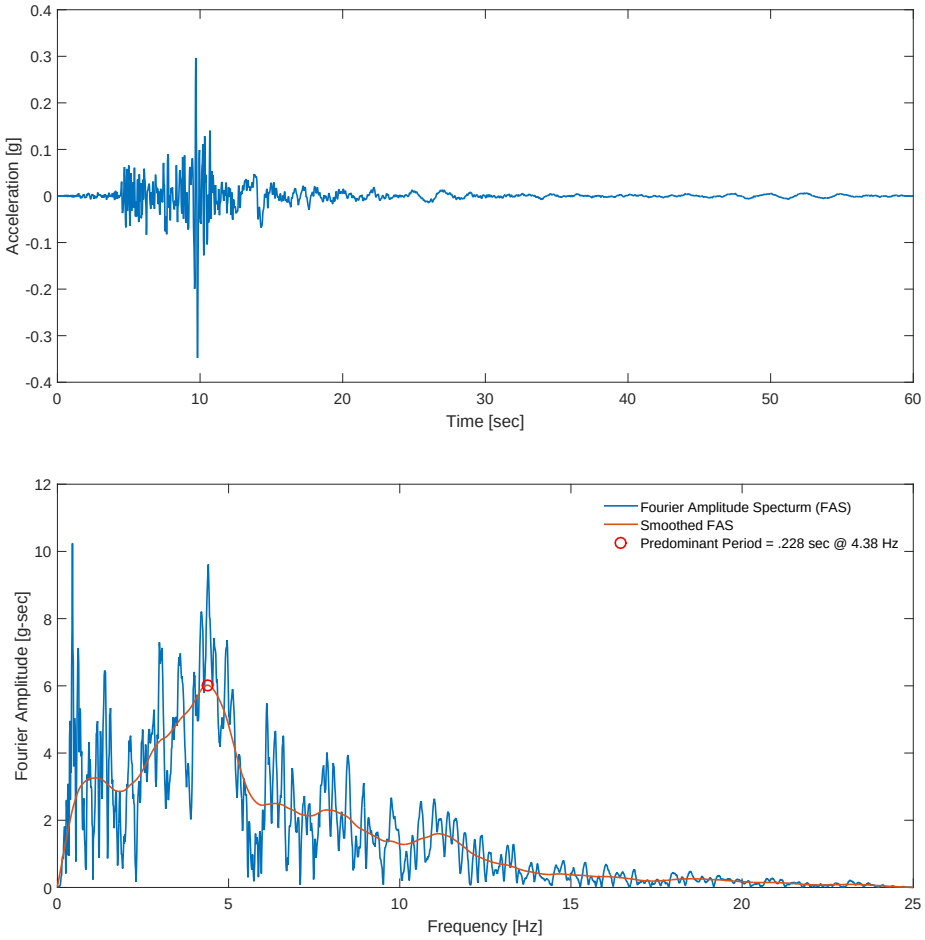

Figure 4.6: *East-west ground acceleration as recorded on the grounds of Santa Monica City Hall during the 1994 Northridge Earthquake (top) and the Fourier amplitude spectrum of this record (bottom).*

dation embedded in a uniform soil half-space. They take the form

$$\bar{k}_j = K_j \alpha_j \eta_j [1 + 2i\beta_j] \tag{4.17}$$

where K_j represents static stiffness, η_j represents an embedment modifier, α_j represents a surface stiffness modifier, and β_j represents the foundation's radiation damping ratio [7].

For the horizontal direction, these parameters are calculated via

$$K_x = \frac{GB}{2-\nu}\left[6.8\left(\frac{L}{B}\right)^{0.65} + 2.4\right] \tag{4.18}$$

$$\eta_x = 1 + \left[.33 + \frac{1.34}{1+\frac{L}{B}}\right]\left[\frac{D}{B}\right]^{0.8} \tag{4.19}$$

$$\alpha_x = 1.0 \tag{4.20}$$

$$\beta_x = \frac{4\left[\frac{L}{B} + \frac{D}{B}\left(\psi + \frac{L}{B}\right)\right]}{\frac{K_x \eta_x}{GB}}\left(\frac{a_0}{2\alpha_x}\right) \tag{4.21}$$

in which

$$\psi = \sqrt{\frac{2(1-\nu)}{1-2\nu}} \leq 2.5 \qquad \text{and} \qquad a_0 = \frac{\omega B}{V_s}\,.$$

Likewise, for the rocking direction

$$K_\theta = \frac{GB^3}{1-\nu}\left[3.73\left(\frac{L}{B}\right)^{2.4} + 0.27\right] \tag{4.22}$$

$$\eta_\theta = 1 + \frac{D}{B} + \left[\frac{1.6}{0.35 + (\frac{L}{B})^4}\right]\left[\frac{D}{B}\right]^2 \tag{4.23}$$

$$\alpha_\theta = 1 - \frac{.55 a_0^2}{\left(0.6 + \frac{1.4}{(\frac{L}{B})^3 + a_0^2}\right)} \tag{4.24}$$

$$\beta_\theta = \left\{\frac{\frac{4}{3}\left[(\frac{L}{B})^3\frac{D}{B} + \psi(\frac{D}{B})^3\frac{L}{B} + (\frac{D}{B})^3 + 3(\frac{L}{B})^2\frac{D}{B} + \psi(\frac{L}{B})^3\right]a_0^2}{\frac{K_\theta \eta_\theta}{GB^3}\left[\frac{1.8}{1+1.75(\frac{L}{B}-1)} + a_0^2\right]}\right\}\left(\frac{a_0}{2\alpha_\theta}\right) + \left\{\frac{\frac{4}{3}(\frac{L}{B}+\psi)(\frac{D}{B})^3}{\frac{K_\theta \eta_\theta}{GB^3}}\right\}\left(\frac{a_0}{2\alpha_\theta}\right)\,. \tag{4.25}$$

Given these impedance formulas and the values in Table 4.3, it is possible to approximate $\bar{k}_x$ with a first-order filter and $\bar{k}_\theta$ with a fourth-order filter. The coefficients of both are found in Table 4.4. Figures 4.7 and 4.8 depict the horizontal and rocking impedance functions and their filter approximations, respectively.

As with the rigid disk on half-space, the filter approximating the horizontal impedance function offers a better fit over the entirety of the frequency domain.

Table 4.4: *Discrete-time filter coefficients approximating horizontal and rocking foundation impedance functions for rectangular foundation embedded in uniform soil half-space.*

j	$a_{x,j}$	$b_{x,j}$ $(\times 10^4)$	$a_{\theta,j}$	$b_{\theta,j}$ $(\times 10^9)$
1	1.0000	4.7879	1.0000	0.4191
2	1.0000	−2.6604	3.0007	1.2576
3			3.0015	1.2580
4			1.0007	0.4195
5			0.0000	−0.0265

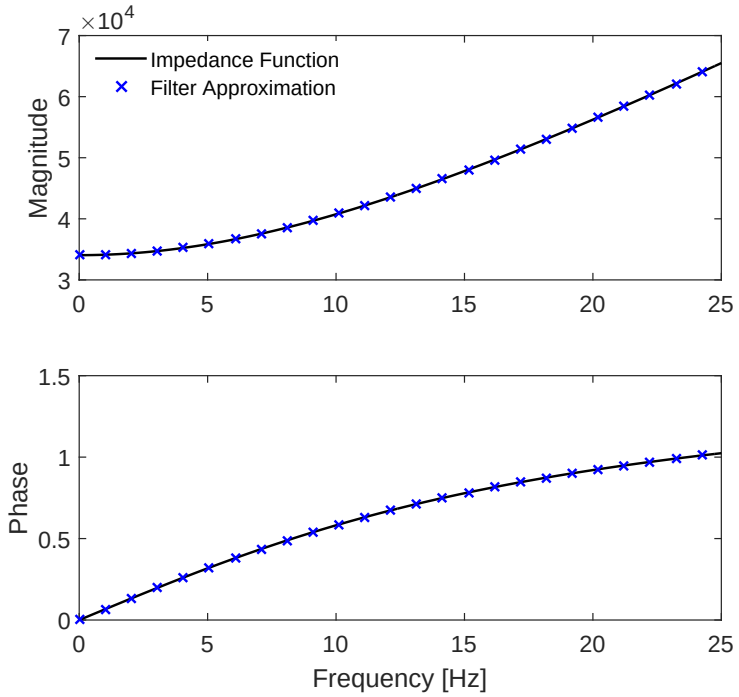

Figure 4.7: *Horizontal foundation impedance function and first-order filter approximation for rigid rectangular embedded in uniform half-space.*

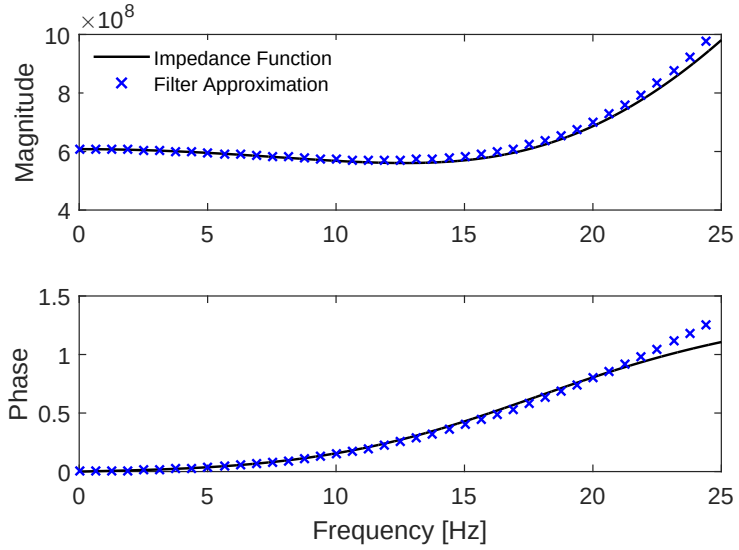

Figure 4.8: *Rocking foundation impedance function and fourth-order filter approximation for rigid rectangular embedded in uniform half-space.*

The filter approximating the rocking impedance function fits well over lower frequencies. Once again, this is sufficient as the majority of the frequency content of the input motion occurs over those frequencies where the fit is good. Figure 4.9 shows the time history analysis computed using the filter approximations. Also shown are the fixed base time history analysis and a substructure time history analysis computed using the frequency domain. Peak top story and displacement and predominant period for all three responses are listed in Table 4.5. The frequency domain and filter solutions show similar period elongation. They also show similar top story displacements and drifts.

4.2.2 Implementation at Various Structure-to-Soil Stiffness Ratios

Figure 4.10 depicts the maximum displacements of the MDOF soil-foundation-structure system at various structure-soil-stiffness ratios. As with with SDOF case in §1.1.4, both the filter and frequency domain responses agree with the fixed-base response at low values of σ^{-1} and diverge at higher values. Interestingly, for this

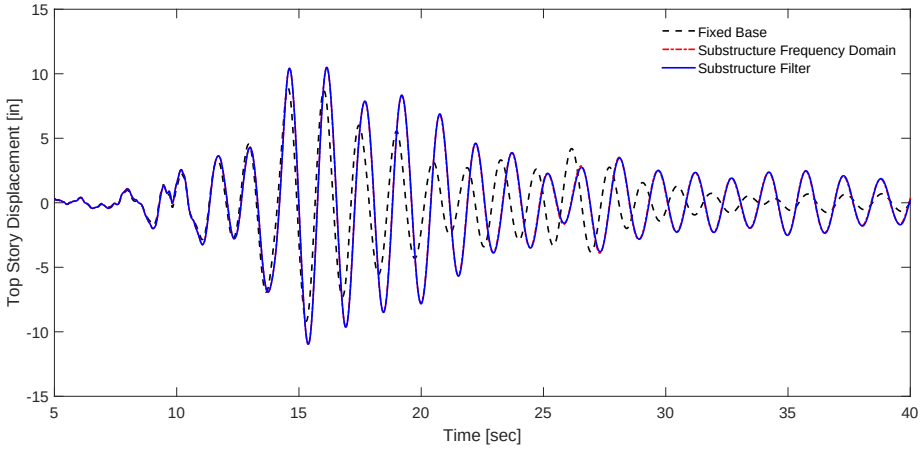

Figure 4.9: *Time history analysis of MDOF soil-foundation-structure system subjected to horizontal ground motion.*

Table 4.5: *Response parameters for MDOF system subjected to horizontal ground motion.*

Model	Predominant Period [sec]	Max. Top Story Displacement [in]	Max. Top Story Drift [in]
Fixed-Base	1.43	9.18	1.84
Frequency Domain	1.63	10.98	2.83
Impedance Filter	1.62	10.97	2.81

case, both substructure models show an increase in structural response as the effects SSI become manifest.

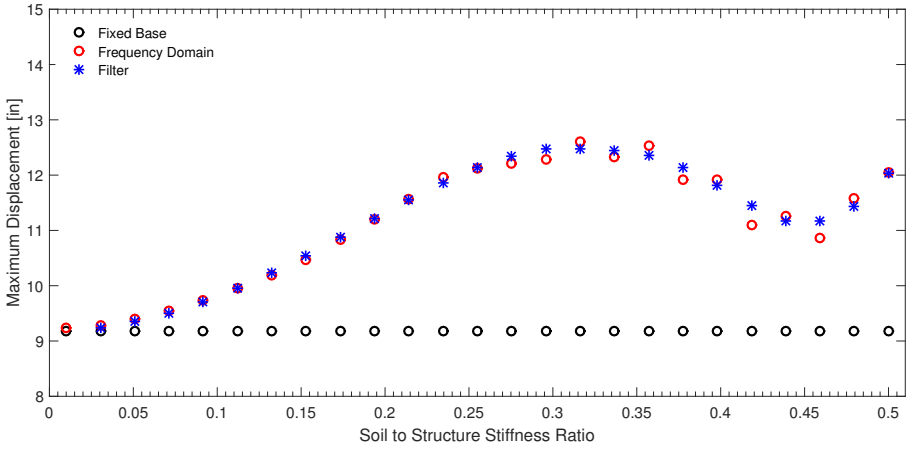

Figure 4.10: *Maximum top-story total displacement of multiple degree-of-freedom soil-foundation-structure system at various soil-to-structure stiffness ratios.*

4.3 Stability

Stability of Newmark integration is well understood [34]. For an implicit scheme used by itself, selection of $\beta = 0.25$ and $\gamma = 0.5$ will yield stable results. Likewise, a recursive digital filter is considered stable if all its poles—i.e., the roots of the denominator polynomial, found in Eq. (3.7)—lie within a complex unit circle [32]. Unfortunately, as will be demonstrated, meeting these two criteria will not necessarily assure the stability of the combined method.

To examine why, consider the uncoupled horizontal free vibration of the foundation, with the structure removed, induced by an initial unit velocity pulse. The equation of motion for such a system is

$$m_f \ddot{u}_{f,n} + f_n = 0 \quad \text{with} \quad u_{f,0} = 0 \quad \text{and} \quad \dot{u}_{f,0} = 1 \tag{4.26}$$

where f_n represents the filter approximating the spring force in the foundation impedance function (note that in following derivation, the subscript f denoting the foundation degree of freedom is dropped for brevity). Selecting integration

and damping constants of $\beta = 0.5$ and $\gamma = 0.5$ yields a stable implicit scheme and simplifies the ensuing algebra. Evaluating (2.16) and (2.17) as such yields,

$$\dot{u}_{n+1} = \dot{u}_n + \Delta_t[\frac{1}{2}\ddot{u}_{n-1} + \frac{1}{2}\ddot{u}_{n+1}]\,, \tag{4.27}$$

$$u_{n+1} = u_n + \Delta_t\dot{u}_n + \Delta_t^2[\frac{1}{2}\ddot{u}_{n+1}]\,. \tag{4.28}$$

Now, following the procedure outlined in [35], it is possible, through a series of substitutions, to reduce (4.26), (4.27), and (4.28) to a linear constant coefficient difference equation for displacement. To do so, take the difference of (4.28) evaluated at times $n+1$ and n to get

$$u_{n+1} - u_n = u_n - u_{n-1} + \Delta_t[\dot{u}_n - \dot{u}_{n-1}] + \Delta_t^2[\frac{1}{2}\ddot{u}_{n+1}]\,. \tag{4.29}$$

Next replace the velocity difference in (4.29) with (4.27) evaluated at time n and rearrange the result, grouping displacements on the left-hand side and accelerations and the right-hand side to get

$$u_{n+1} - 2u_n + u_{n-1} = \frac{\Delta_t^2}{2}[\ddot{u}_{n+1} + \ddot{u}_{n-1}]\,. \tag{4.30}$$

4.3.1 Stability of Integrator with First-Order Filter

At this point, for derivation purposes, assume that f_n is approximated by the following first-order filter

$$f_n = b_0u_n + b_1u_{n-1} - a_1f_{n-1} \tag{4.31}$$

Substituting (4.31) into (4.26) and the subsequent result evaluated at both time $n+1$ and time $n-1$ into (4.30) yields,

$$u_{n+1} - 2u_n + u_{n-1} = -\frac{\Delta_t^2}{2m}[b_0u_{n+1} + b_1u_n - a_1f_n + b_0u_{n-1} + b_1u_{n-2} - a_1f_{n-2}] \tag{4.32}$$

Next, eliminate f_n and f_{n-2} by substituting (4.26) evaluated at times n and $n-2$ into (4.30) and substituting this result into (4.32). Grouping the like terms yields

the following linear, constant-coefficient difference equation for the displacement u_{n+1} in terms of the previous displacements from time n to time $n-2$:

$$\phi_1 u_{n+1} + \phi_2 u_n + \phi_3 u_{n-1} + \phi_4 u_{n-2} = 0 \tag{4.33}$$

where

$$\phi_1 = 1 + \frac{\Delta_t^2 b_0}{2m} \quad \phi_2 = -2 + \frac{\Delta_t^2 b_1}{2m} + a_1 \quad \phi_3 = 1 + \frac{\Delta_t^2 b_1}{2m} - 2a_1 \quad \phi_4 = \frac{\Delta_t^2 b_1}{2m} + a_1 \,.$$

As established in [36], such a difference equation is said to be stable if it satisfies

$$|\lambda_j| < 1 \quad \text{where} \quad j = 1, 2, \cdots, O \tag{4.34}$$

where O is the order of the difference equation and ρ_j are the roots of the characteristic polynomial

$$\sum_{j=1}^{O+1} \phi_j \lambda^{O-j+1} \,. \tag{4.35}$$

Thus, for this case of a first-order filter combined with a Newmark integration scheme of $\beta = 0.5$ and $\gamma = 0.5$ stability is governed by the roots of the cubic equation

$$\phi_1 \lambda^3 + \phi_2 \lambda^2 + \phi_3 \lambda + \phi_4 \tag{4.36}$$

and is a function of the integration time step, the filter coefficients, and the foundation mass.

4.3.2 Stability of Integrator with Arbitrary Order Filter

As a first-order filter offers a poor approximation of most impedance functions, it is necessary to expand the stability derivation to account for filters of arbitrary order, N. Following the logic outlined above, the characteristic polynomial for such a filter, again combined with a Newmark integration scheme of $\beta = 0.5$ and $\gamma = 0.5$, takes the form

$$\phi_1 \lambda^{N+2} + \phi_2 \lambda^{N+1} + \cdots + \phi_{N+2} \lambda + \phi_{N+3} \tag{4.37}$$

where

$$\phi_1 = 1 + \frac{\Delta_t^2 b_0}{2m}$$

$$\phi_2 = -2 + \frac{\Delta_t^2 b_1}{2m}$$

$$\phi_3 = 1 + \frac{\Delta_t^2 b_2}{2m} + \frac{\Delta^2 b_0}{2m} - 2a_1 + a_0$$

$$\phi_j = \frac{\Delta_t^2 b_{j-3}}{2m} + \frac{\Delta^2 b_{j-1}}{2M} + a_{j-3} - 2a_{j-2} + a_{j-1}$$

$$\text{where} \quad j = 4 \rightarrow J+3 \quad \ni b_j = a_j = 0 \quad \forall \quad j > J$$

As before, the method will be stable if the magnitude of all the roots of the polynomial (4.37) are less than one. Furthermore, this stability is *also* a function of the time step, the filter coefficients, and the foundation mass. Note that a filter of order J yields a characteristic polynomial of order $O = N + 3$. As such, the algebra involved in determining the roots complicates determination of any closed-form solution for stability criteria. That said, Eq. (4.37) is still of value as it may be used either as a constraint on the curve fitting algorithm used to determine the filter coefficients or as an *a posteriori* check on whether a filter-integrator algorithm will yield stable time history analyses.

4.3.3 Stability Demonstration

Close inspection of Figure 4.10 reveals a missing data point for the filter method at $\sigma^{-1} = 0.01$. The maximum characteristic root of the filter-integrator of the horizontal impedance function at that stiffness ratio is $\lambda_{max} = 1.0018$. As predicted by §1.3.2, the result is unstable! Figure 4.11 displays a stability map for stiffness ratio. The map, which is unique to the soil and foundation properties of the substructure system, is generated by varying integration time step, Δ_t, and the frequency step, Δ_ω, used to the sample the impedance function prior to mapping

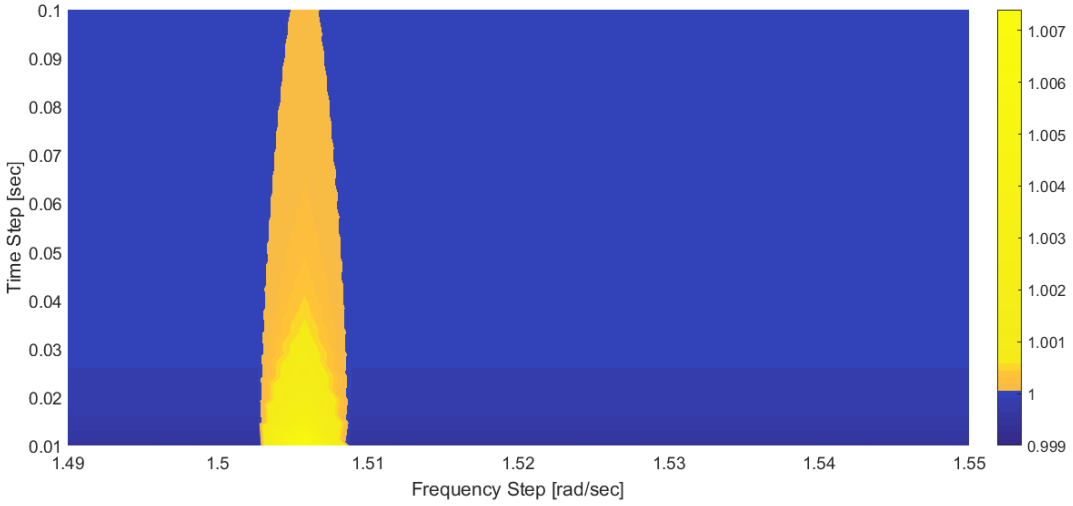

Figure 4.11: *Stability map for horizontal filter at structure-to-soil stiffness ratio of 0.01. Color bar on right represents maximum characteristic root magnitude.*

from continuous to discrete frequency. As such, each frequency step represents a distinct filter design. The color bar on the right side of the figure represents the maximum characteristic root value for each filter. The figure shows a band of instability between frequency steps of approximately 1.505 and 1.51 radians per second. To remedy the issue, the filter must be redesigned using a frequency step outside the instability band. Indeed, selecting a frequency step of 1.52 radians per second yields a filter-integrator with a maximum characteristic root value of $\lambda_{max} = 0.9998$. The coefficients of both filters are displayed in Table 4.6.

Table 4.6: *Coefficients of original (unstable) and revised (stable) filters approximating foundation impedance function for soil-to-structure stiffness ratio of 0.01.*

	Original Filter		Revised Filter	
j	$a_{x,j}$	$b_{x,j}$ $(\times 10^{-6})$	$a_{x,j}$	$b_{x,j}$ $(\times 10^{-6})$
0	1.0000	7.4793	1.0000	7.4776
1	1.0000	6.4627	1.0000	6.4644

For verification, consider Figure 4.12. Figure 4.12(a) depicts the time-history response for the MDOF substructure system subjected to a unit velocity pulse as computed using the original filter. The result is clearly unstable, with displacement increasing without bound. Figure 4.12(b) depicts the same, this time with a stable result, for the redesigned filter.

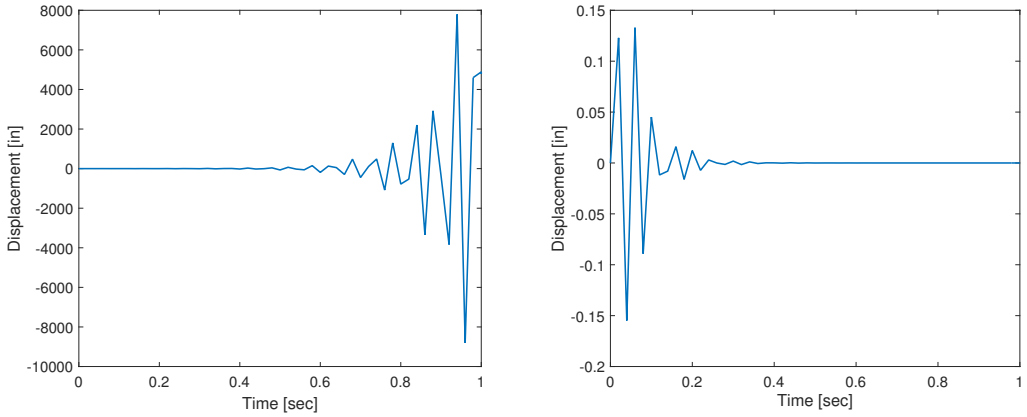

(a) Unstable system **(b)** Stable system

Figure 4.12: *Displacement of foundation with horizontal impedance function at structure-to-soil stiffness ratio of 0.01.*

4.4 Coupled Impedance Systems

Up to this point, all the soil-foundation-structure systems in this work have been modeled using uncoupled horizontal and rocking impedances. In such systems the forces generated in the foundation impedance functions may be represented in the frequency domain as

$$\begin{Bmatrix} F_{x,l} \\ F_{\theta,l} \end{Bmatrix} = \begin{bmatrix} \bar{k}_{x,l} & 0 \\ 0 & \bar{k}_{\theta,l} \end{bmatrix} \begin{Bmatrix} U_{f,l} \\ \Theta_{f,l} \end{Bmatrix} \tag{4.38}$$

with zeros in for the off-diagonal terms in what may be called the impedance matrix. From a signal processing perspective these forces can be thought of as the

resultants of two independent single-input, single-output (SISO) systems. Conversely, the forces in a coupled system are the resultants of what is termed a multiple-input, multiple output (MIMO) system. For such systems, the forces are,

$$\begin{Bmatrix} F_{x,l} \\ F_{\theta,l} \end{Bmatrix} = \begin{bmatrix} \bar{k}_{x,l} & \bar{k}_{x\theta,l} \\ \bar{k}_{\theta x,l} & \bar{k}_{\theta,l} \end{bmatrix} \begin{Bmatrix} U_{f,l} \\ \Theta_{f,l} \end{Bmatrix} \tag{4.39}$$

in which the coupling terms $\bar{k}_{x\theta,l}$ and $\bar{k}_{\theta x,l}$ indicate an interaction between horizontal and rocking motion. As impedance matrices are generally symmetric in the following these coupling terms are referred to as $\bar{k}_{c,l}$ in the frequency domain and $\bar{k}_{c,n}$ in the time domain. The presence of these terms somewhat complicates analysis and as they are generally relatively small as compared to the on-diagonal impedance terms, they are often ignored in practice. That said, all of the methods examined in Chapter 2 can be modified to accommodate coupled systems. This section formulates and demonstrates implementation of the filter method for coupled systems.

4.4.1 Formulation

The equations of motion for the substructure model of a coupled single degree of freedom soil-foundation-structure structure system are similar to that of the uncoupled case. In matrix form, they are

$$\boldsymbol{M}\ddot{\boldsymbol{u}}_n + \boldsymbol{C}\dot{\boldsymbol{u}}_n + \boldsymbol{K}\boldsymbol{u}_n + \boldsymbol{f}_n = \boldsymbol{p}_n \tag{4.40}$$

where $\boldsymbol{f}_n$ contains the time domain representation of (4.42):

$$\boldsymbol{f}_n = \begin{Bmatrix} f_{x,n} \\ f_{\theta,n} \end{Bmatrix} = \begin{bmatrix} \bar{k}_{x,n} & \bar{k}_{c,n} \\ \bar{k}_{c,n} & \bar{k}_{\theta,n} \end{bmatrix} \begin{Bmatrix} u_{f,n} \\ \theta_{f,n} \end{Bmatrix}, \tag{4.41}$$

and $\boldsymbol{M}$, $\boldsymbol{C}$, and $\boldsymbol{K}$ represent the mass, damping, and stiffness matrices as shown in (4.1). Following the methodology outlined in Section 4.1 these are adapted for

the filter method as:

$$\boldsymbol{M}\ddot{\boldsymbol{u}}_n + \boldsymbol{C}\dot{\boldsymbol{u}}_n + \hat{\boldsymbol{K}}\boldsymbol{u}_n + \boldsymbol{f}_n = \hat{\boldsymbol{p}}_n \tag{4.42}$$

in which

$$\hat{\boldsymbol{K}} = \begin{bmatrix} k & -k & -kh \\ -k & k + b_{x,0} & kh + b_{c,0} \\ -kh & kh + b_{c,0} & kh^2 + b_{\theta,0} \end{bmatrix}, \tag{4.43}$$

and

$$\hat{\boldsymbol{p}}_n = -\begin{Bmatrix} m \\ m_f \\ 0 \end{Bmatrix} \ddot{u}_{g,n} + \begin{Bmatrix} 0 \\ \hat{f}_{x,n} + \hat{f}_{c,n} \\ \hat{f}_{\theta,n} + \hat{f}_{c,n} \end{Bmatrix}. \tag{4.44}$$

Formulating the equations in this manner allows approximation of the MIMO system via approximation its component SISO systems, these being,

$$\bar{k}_{x,n} * u_{f,n} = f_{x,n} \approx b_{x,0} u_{f,n} + \sum_{j=1}^{k} b_{x,j} u_{f,n-j} - \sum_{j=1}^{l} a_{x,j} f_{x,n-j} = b_{x,0} + \hat{f}_{x,n}\,, \tag{4.45}$$

$$\bar{k}_{x\theta,n} * \theta_{f,n} = \bar{k}_{\theta x,n} * u_{f,n} = f_{c,n} \approx b_{c,0}\theta_{f,n} + \sum_{j=1}^{k} b_{c,j}\theta_{f,n-j} - \sum_{j=1}^{l} a_{c,j} f_{c,n-j} = b_{c,0} + \hat{f}_{c,n}\,, \tag{4.46}$$

and

$$\bar{k}_{\theta,n} * \theta_{f,n} = f_{\theta,n} \approx b_{\theta,0}\theta_{f,n} + \sum_{j=1}^{k} b_{\theta,j}\theta_{f,n-j} - \sum_{j=1}^{l} a_{\theta,j} f_{\theta,n-j} = b_{\theta,0} + \hat{f}_{\theta,n}\,. \tag{4.47}$$

4.4.2 Implementation Example

To demonstrate implementation, consider a single degree of freedom structure supported by a rigid disk foundation resting on a uniform soil half-space, the key physical properties of which are found in Table 4.7.

Table 4.7: *Key physical properties of soil-foundation-structure system for coupled impedance implementation example*

Geology	
G: Soil Shear Modulus	2.68 ($\times 10^5$) kPa
V_s: Soil Shear Wave Velocity	200 m/sec
ν: Soil Poisson Ratio	1/3
Structure	
T_n: Structural Period	1 sec
ξ: Damping Ratio	3.0 %
h: Structure Height	50 m
w: Structure Weight	1 kN
Foundation	
r: Foundation Radius	5 m
t: Foundation Thickness	1 m
w_f: Foundation Weight	0.1 kN

The impedance functions for this system are taken from Veletsos and Wei [10]. The system's impedance matrix takes the form

$$\bar{\boldsymbol{k}} = \begin{bmatrix} \bar{k}_x & \bar{k}_c \\ \bar{k}_c & \bar{k}_\theta \end{bmatrix} = \begin{bmatrix} (k_{11} + ia_0 c_{11})K_x & (k_{21} + ia_0 c_{21})K_x r \\ (k_{21} + ia_0 c_{21})K_x r & (k_{22} + ia_0 c_{22})K_\theta \end{bmatrix} \tag{4.48}$$

in which the coefficients k_{11}, k_{21}, and k_{22} representing the horizontal, coupling, and rocking stiffnesses and c_{11}, c_{21}, and c_{22} representing the same for damping are found in Figure 4.14. The constants K_x and K_θ take the form

$$K_x = \frac{8Gr}{2-\nu} \quad \text{and} \quad K_\theta = \frac{8Gr^3}{3-3\nu}\,. \tag{4.49}$$

As indicated in (4.45), (4.46), and (4.47) three discrete-time filters are required

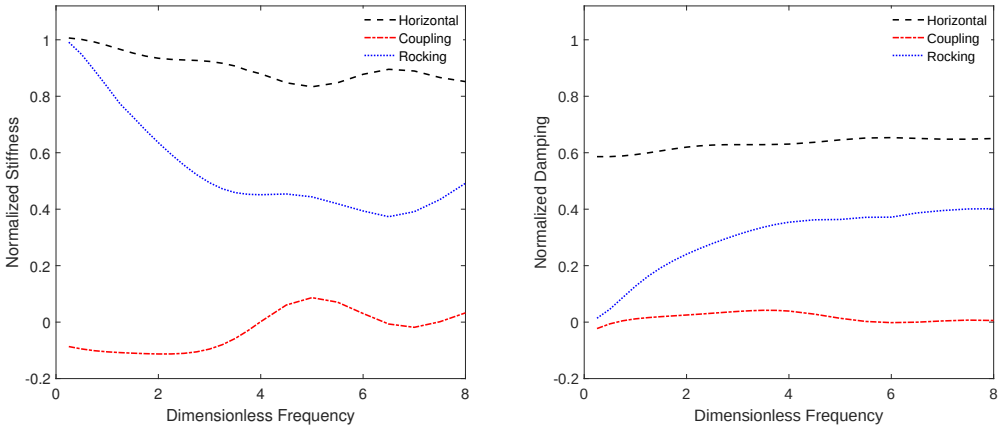

(a) Stiffness Coefficients **(b)** Damping Coefficients

Figure 4.13: *Stiffness and damping impedance coefficients for rigid disk resting on elastic soil half-space.*

to approximate $\bar{\boldsymbol{k}}$. The coefficients of these filters are presented in Table 4.8 with the corresponding curve fits found in Figure 4.14.

Figure 4.15 shows the total displacement time-history response for the structure when subjected to the Loma Prieta SFA ground motion. Plotted are the fixed-base response, the response computed ignoring the coupling terms (assuming $\bar{k}_c = 0$), and the coupled response. Figure 4.16 shows the Fourier amplitude spectra of the same three responses. Considering both figures, it is apparent that the coupled and uncoupled responses are quite similar. The coupled response does exhibit slightly more damping and period elongation than the uncoupled response. This is confirmed by Table 4.9 which compares the key response parameters. Thus for this case, ignoring the coupling terms could be considered a conservative assumption.

Table 4.8: *Coefficients of discrete-time filters approximating horizontal, coupling, and rocking impedance functions for rigid disk foundation resting on uniform soil half-space.*

	Horizontal Filter		Coupling Filters		Rocking Filter	
j	$a_{x,j}$	$b_{x,j}$ $(\times 10^{-4})$	$a_{c,j}$	$b_{c,j}$ $(\times 10^{-3})$	$a_{\theta,j}$	$b_{\theta,j}$ $(\times 10^{-5})$
0	1.0000	2.7220	1.0000	−0.8950	1.0000	3.4365
1	0.3336	−3.3358	−1.6272	−0.7195	0.5669	−3.1817
2	0.4322	4.0570	2.6572	0.1501	0.3142	3.7139
3	0.1320	−4.3011	−3.7285	−0.4008	0.2435	−2.8721
4	−0.2906	3.3368	3.5038	2.7206	−0.2564	2.0023
5	0.2805	−2.0997	−3.6980	−1.0432	0.1293	−0.8476
6	−0.2083	1.0916	2.9264	2.4274	−0.1431	0.2297
7	0.1331	−0.3863	−1.9238	−2.3913	−0.0090	0.0000
8	−0.0447	0.0593	1.2955	0.9807		
9	−0.0035	0.0000	−0.5638	−1.4341		
10			0.2361	0.5892		
11			−0.0716	0.0000		

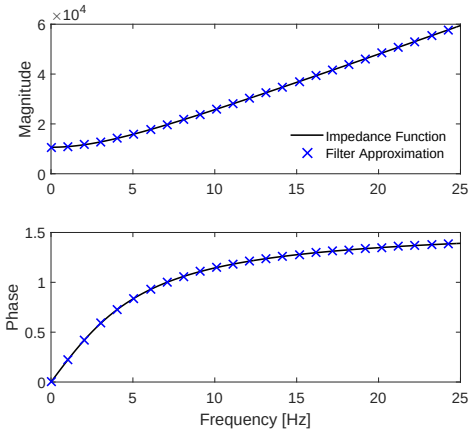

(a) Horizontal Filter

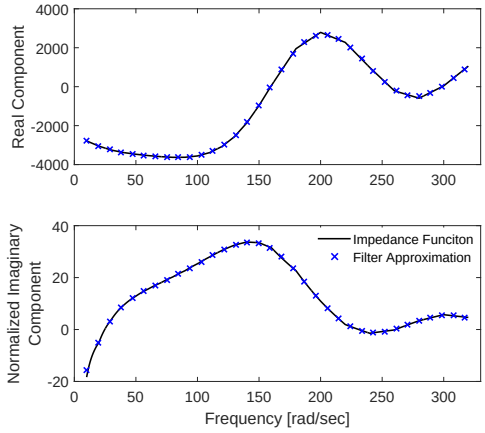

(b) Coupling Filters

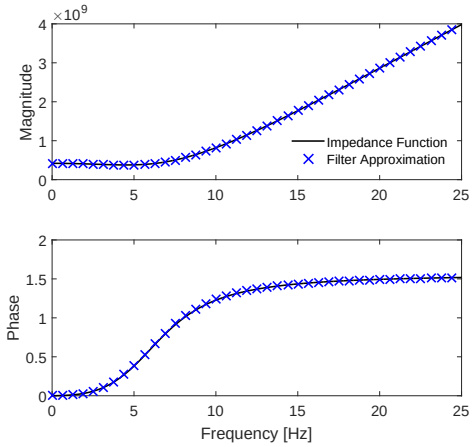

(c) Rocking Filter

Figure 4.14: *Real and frequency normalized imaginary components of discrete-time filters approximating horizontal, coupling, and rocking impedance functions for rigid disk foundation resting on a uniform soil half-space.*

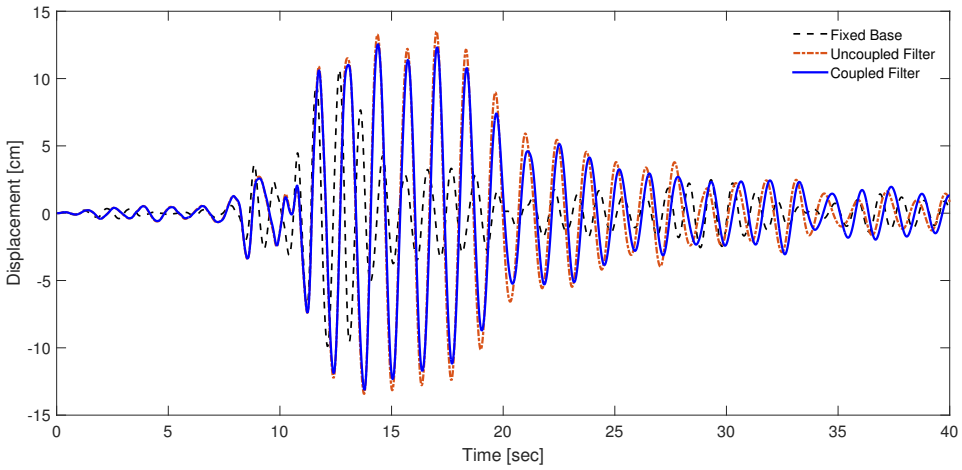

Figure 4.15: *Time history response of soil-foundation-structure system consisting of single degree of freedom structure founded on rigid disk resting on uniform soil half-space.*

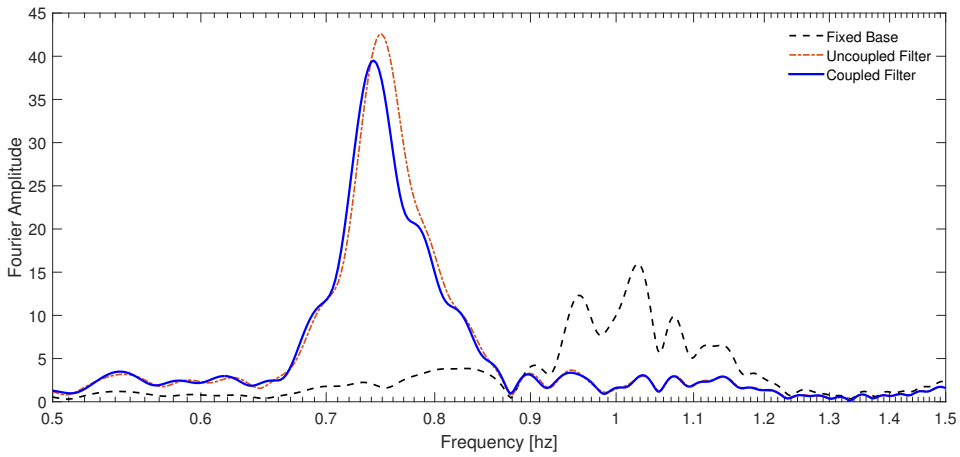

Figure 4.16: *Fourier Amplitude spectrum of time history response of soil-foundation-structure system consisting of single degree of freedom structure founded on rigid disk resting on uniform soil half-space.*

Table 4.9: *Key response parameters for soil-foundation-structure system with coupled impedance.*

Model	Predominant Period [sec]	Max. Total Displacement [cm]
Fixed-Base	0.97	10.65
Uncoupled	1.35	13.50
Coupled	1.33	13.30

CHAPTER 5

Inelastic Implementation

This chapter explores implementation of the filter method for soil-foundation-structure systems in which the systems' structures are subjected to deformations beyond their elastic limits. The confluence of two major factors has served to fuel demand for such analyses. The first is the realization that, contrary to the guidelines offered in many prescriptive design documents, inertial SSI, under the right conditions, has the potential to significantly increase structural response. The second is the continued trend within the civil engineering community toward performance-based design.

Prior to the turn of the century, most building codes offered prescriptive design methodologies that allowed engineers to either ignore inertial SSI or apply a blanket reduction in expected demand when considering its effects on inelastic structures [37, 38]. In 2000, Mylonakis pointed out the danger of this approach by showing that substructure analyses of stiff inelastic structures subjected to long period motion may demonstrate increased response when compared to corresponding fixed-base cases [2]. These results have been confirmed through similar works by the likes of Aviles and Perez-Rocha [39] and Khoshnoudian and Behmanesh [40].

These revelations coincided with emergence of performance-based methods as the future of seismic design [41, 42]. Generally speaking, performance based seismic design (PBSD) seeks to ensure structures meet required performance levels when subjected to various levels of hazard, in this case from earthquake induced

ground shaking. Figure 5.1, adopted from the Structural Engineers of America's *Vision 2000* [43], depicts this concept graphically with desired performance on the horizontal axis and earthquake hazard on the vertical axis. Structures falling in the *operational*, *life safety*, and *near collapse* categories all may experience some form of damage that would require inelastic vice elastic analysis. Furthermore, structures with active or passive damping systems that absorb vibrational energy may require inelastic analyses in the fully functional performance category.

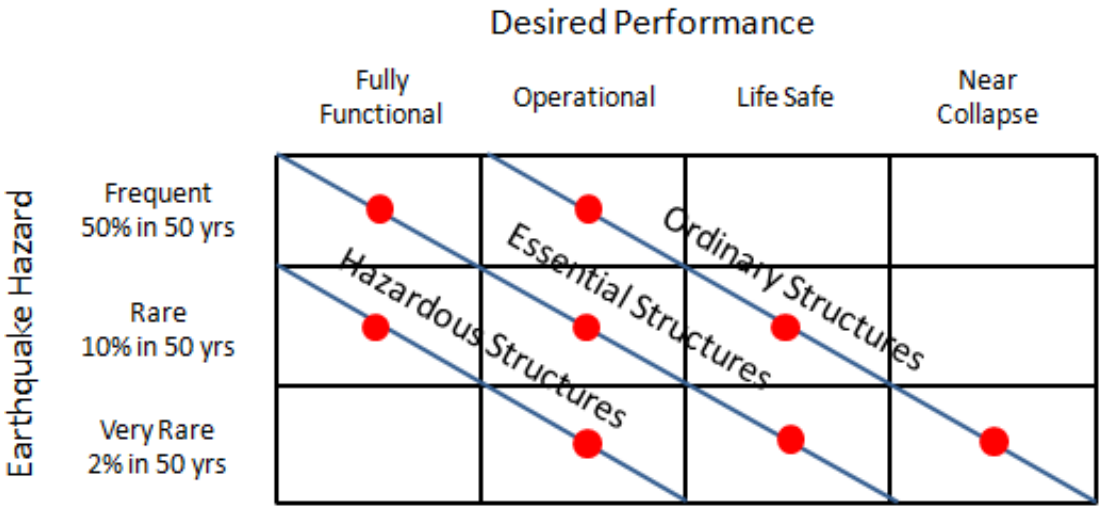

Figure 5.1: *Performance Based Seismic Design (adapted from SEAOC Vision 2000).*

Recall from Chapter 2 that the challenge in applying substructure analyses to determine structural response histories involves addressing the frequency dependence of the foundation impedance functions. As with elastic analysis, the current state of practice for inelastic analysis includes several options of doing so. These include sampling the impedance function, either at the structure's flexible base period [7] or a period adjusted for inelastic effects [44], use of replacement oscillators [39], and use of lumped parameter models [24]. For the inelastic case, these methods are subject to the same detractors identified in Chapter 2 with the replacement oscillator methods similar to the representative frequency methods

in that they effectively sample the impedance function at a single frequency. Note also that the frequency domain method is not listed among these options as it is incapable of accounting for the time-dependent nature of inelastic deformations.

Chapter 4 used the frequency domain method as a baseline substructure solution with which to verify the effectiveness of the filter method. As the frequency domain is incapable of accounting for structural inelasticity, this chapter will use the time domain convolution solution in its place.

5.1 Elastoplastic SDOF Systems

To demonstrate inelastic implementation, consider the soil-foundation-structure system depicted in Figure 5.2(a) and the corresponding system parameters found in Table 5.2. This system is identical to that in found in Figure 2.2 with the

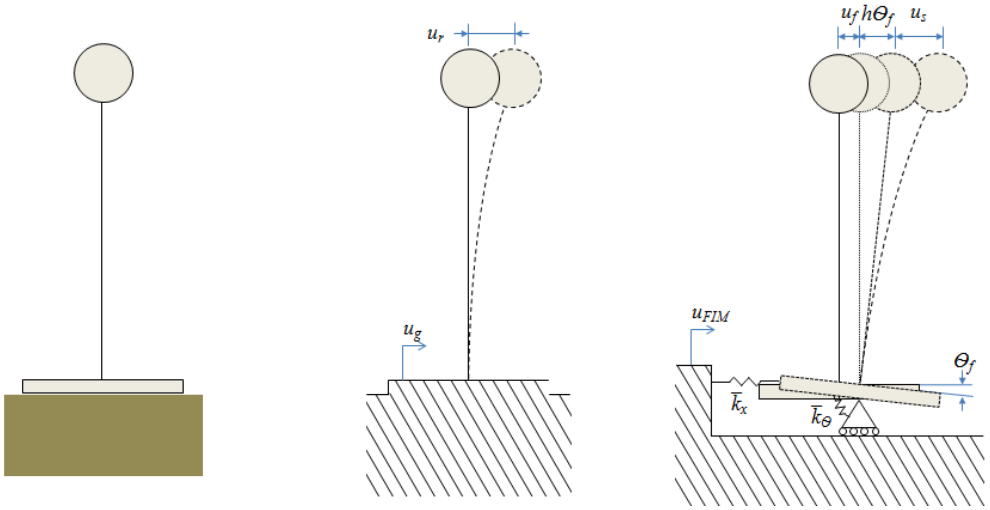

(a) Soil-Foundation-Structure System **(b)** Fixed Base Model **(c)** Substructure Model

Figure 5.2: *A simple soil-foundation-structure system with fixed base and substructure models.*

exception that the structure is now constrained to perform in an elasto-plastic

Table 5.1: *Inelastic Soil-Foundation-Structure System Parameters.*

Geology	
G: Soil Bulk Modulus	2.4285 kip/in^2
V_s: Shear Wave Velocity	1000 ft/sec
ν: Poisson's Ratio	1/3
Structure	
w: Structure Weight	1000 kips
w_f: Foundation Weight	100 kips
h: Structure Height	30 ft
T: Structural Period	1 sec
ξ: Damping Ratio	0.03
$\bar{f}_y$: Normalized Structural Yield Strength	0.5
r: Foundation Radius	10 ft

manner by the normalized yield strength $\bar{f}_y$. Note that structural displacement is also defined differently in Figure 5.2. Introduced is the parameter u_s as a measure of the structures displacement *relative* to its base. Use of this relative displacement in formulation of the substructure system's equations of motion will facilitate numerical integration of the resulting nonlinear system of equations. Note that for the fixed base case, u_1, the displacement from Figure 2.2, is equivalent to u_s. For the substructure case however,

$$u_s = u_1 - u_f - h\theta_f \,. \tag{5.1}$$

5.1.1 Plasticity Function

Following the conventions outlined by Chopra [45], $\bar{f}_y$ is defined as

$$\bar{f}_y = \frac{f_y}{f_o} \tag{5.2}$$

in which f_y denotes structural yield strength and f_o denotes the maximum structural resistance force assumed to be generated if the structure were to remain elastic. The structural resistance force at any time n is thus

$$f_{s,n} = \begin{cases} ku_{s,n} & u_{s,n} < u_{s,y} \\ ku_{s,y} & u_{s,n} \geq u_{s,y} \end{cases} \tag{5.3}$$

where k is the structure's elastic stiffness computed according to (2.6), $u_{s,n}$ is the structural displacement at any given time n, and u_y is the structural yield displacement defined as

$$u_y = \frac{f_y}{k} \tag{5.4}$$

Note that for the case of the substructure model, $u_{s,n}$ denotes only the relative motion of the structure compared to the foundation and does not include either the rigid body displacement or rotation caused SSI. Two other parameters related to normalized yield strength are the yield strength reduction factor R_y and ductility factor μ. Computed as

$$R_y = \frac{f_0}{f_y} \quad \text{and} \quad \mu = \frac{u_{s,max}}{u_{s,y}} \tag{5.5}$$

where $u_{s,max}$ refers to the maximum inelastic structural deformation, these factors offer convenient means of quantifying inelastic structural response.

For an elastoplastic system, the structural restive force, $f_{s,n}$ can be found at any time n given the system's displacement history according to Simo's return mapping algorithm [46], which is outlined in Figure 5.3. Adopting his notation, the algorithm uses current structural displacement $u_{s,n}$ and the past value of the structure's plastic displacement u^p_{n-1} to compute the current value of the

Compute trial force: $f_{s,n}^{Trial} = k(u_{s,n} - u_{s,n-1}^{p})$;
Compute trial yield condition: $f_n^{Trial} = |f_{s,n}^{Trial}| - f_y$;
if $f_n^{Trial} \leq 0$ **then**
    Elastic Step:
    Compute resistive force: $f_{s,n} = f_{s,n}^{Trial}$;
    Compute plastic displacement: $u_{s,n}^{p} = u_{s,n-1}^{p}$;
    Set tangent stiffness to elastic stiffness: $k_{t,n} = k$;
else
    Plastic Step:
    Compute resistive force: $f_{s,n} = \left[1 - \frac{f^{Trial}}{f_{s,n}^{Trial}}\right] f_{s,n}^{Trial}$;
    Compute plastic displacement: $u_{s,n}^{p} = u_{s,n-1}^{p} + \frac{f^{Trial}}{k}\text{sign}(f_{s,n}^{Trial})$;
    Set tangent stiffness to plastic stiffness: $k_{t,n} = 0$;
end

Figure 5.3: *Return mapping algorithm for elasto-plastic system, adapted from Simo and Hughes [46].*

structure's resistance force $f_{s,n}$ by computing a trial resistive force $f_{s,n}^{Trial}$ and subsequent trial yield condition f_y^{Trial}. If the yield condition is less than or equal zero, the structure is assumed to be undergoing elastic displacement between $u_{s,n-1}$ and $u_{s,n}$ and the trial force is kept. If not, the displacement is assumed to be plastic and the return mapping is used to update $f_{s,n}$ and $u_{s,n}^{p}$. For both cases, the algorithm also provides a tangent stiffness, $k_{t,n}$ at each time which represents an estimate of the stiffness between any two successive displacements, u_{n-1} and u_n. As an illustrative example, Figure 5.4 depicts the force-deformation relationship for the system in Figure 5.2 when subjected to the displacement-based CUREE loading protocol [47]. The linearly elastic, perfectly plastic nature of the structure is clearly evident from the bilinear behavior of exhibited in plot. In the following,

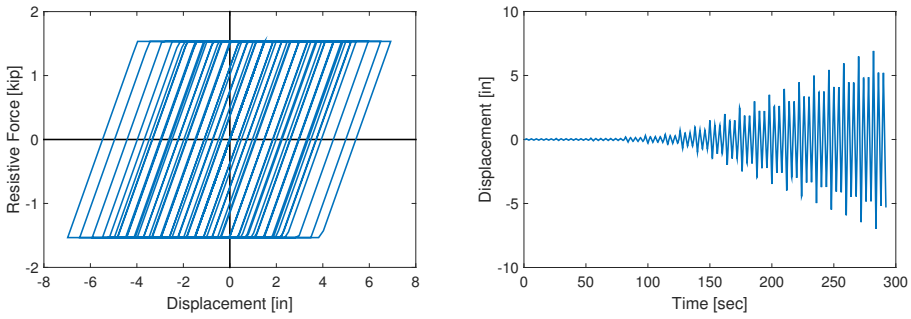

(a) **(b)**

Figure 5.4: *Force-deformation relationship (a) for elasto-plastic system subjected to CUREE loading protocol (b).*

this algorithm will be used to compute structural resistance force for both the fixed base and substructure cases. Both formulations will be modular, allowing for use with any plasticity scheme of similar construct.

5.1.2 Fixed Base Case

Returning to the system in Figure 5.2, the equation of motion for the fixed base model is:

$$m\ddot{u}_{s,n} + c\dot{u}_{s,n} + f_{s,n} = p_n \tag{5.6}$$

in which m and c represent structural mass and damping (with both calculated according to (2.6)). The term p_n represents the external force applied to the system at each time step n. It is calculated according to

$$p_n = -m\ddot{u}_{FIM,n} \tag{5.7}$$

with $\ddot{u}_{FIM,n}$ representing the foundation input motion. As with Chapters 2 and 4, the foundation input is assumed to equal the free-field motion thus ignoring the kinematic interaction effects.

Numerical integration of this partial differential equation is complicated by

the nonlinear nature of the restive force $f_{s,n}$. It is typically accomplished using an iterative, incremental version of the Newmark scheme outlined in Chapter 2 such as that offered by Chopra [45] and outlined in Figure 5.5. Steps 9 through 14 include a Newton-Raphson iteration scheme intended to reduce errors induced through use of the tangent stiffness $k_{t,n}$ as an estimate of structural stiffness and through use of a constant time step Δ_t which may delay identification of stiffness changes [45, 48].

The time-history response for the inelastic soil-foundation-structure system shown in Figure 5.2 when subjected to the Loma Prieta SFA ground motion (recall Figure 2.3) is shown in Figure 5.6. The system's elastic fixed-base response is included in the plot for comparison. The major differences in the inelastic response compared to that of the elastic system are a noticeable decrease in maximum displacement and the addition of a permanent displacement which manifests as the non-zero displacement at the end of the time-history. The maximum displacement of the inelastic response is $u_{s,max} = 3.17$ inches as compared to the elastic maximum of 4.23 inches. The permanent inelastic displacement, resultant from unrecoverable yield deformations within the structure, is $u_{s,final} = 1.10$ inches.

Another way to quantify the effects of inelasticity on structural response is by examining the energy dissipated during yielding. Calculated as

$$E_y = \sum_{j=1}^{n} \dot{u}_{s,j} f_{s,j} - \frac{1}{2k} f_{s,j}^2 \tag{5.8}$$

this represents the cumulative energy dissipated through yielding of the structural system. For the fixed base case this amounts to $E_y = 663.2$ kips.

5.1.3 Substructure Case

Using the relative displacement convention, the time domain equations of motion for the substructure model are:

$$\begin{bmatrix} m & m & mh \\ m & m+m_{f,} & mh \\ mh & mh & mh^2+I_f \end{bmatrix} \begin{Bmatrix} \ddot{u}_{s,n} \\ \ddot{u}_{f,n} \\ \ddot{\theta}_{f,n} \end{Bmatrix} + \begin{bmatrix} c & 0 & 0 \\ 0 & 0 & 0 \\ 0 & 0 & 0 \end{bmatrix} \begin{Bmatrix} \dot{u}_{s,n} \\ \dot{u}_{f,n} \\ \dot{\theta}_{f,n} \end{Bmatrix} + \begin{Bmatrix} f_{s,n} \\ f_{x,n} \\ f_{\theta,n} \end{Bmatrix} = - \begin{Bmatrix} m \\ m+m_f \\ mh \end{Bmatrix} \ddot{u}_{FIM,n} \quad (5.9)$$

where $f_{x,n}$ and $f_{\theta,n}$ represent the forces generated in the horizontal and rocking foundation impedance functions, I_f represents the foundation's mass moment of inertia, and θ represents foundation rotation. Recall for the filter solution, these forces are approximated by the recursive relations

$$f_{x,n} \approx b_{x,0} u_{f,n} + \sum_{j=1}^{J} b_{x,j} u_{x,n-j} - \sum_{j=1}^{J} a_{x,j} f_{x,n-j} \quad (5.10)$$

and

$$f_{x\theta,n} \approx b_{\theta,n} \theta_{f,n} + \sum_{j=1}^{J} b_{\theta,j} \theta_{f,n-j} - \sum_{j=1}^{J} a_{\theta,j} f_{\theta,n-j} \quad (5.11)$$

in which the leading teams are kept out of each summation as they involve the unknown displacements $u_{f,n}$ and $\theta_{f,n}$ where as past values of displacement $u_{f,n-}$ and $\theta_{f,n-j}$ are known at each time step n during numerical integration. Inserting these into the equations of motion and arranging the known values on the left-hand

side and the unknowns on the right-hand side yields

$$\begin{bmatrix} m & m & mh \\ m & m+m_{f,} & mh \\ mh & mh & mh^2+I_f \end{bmatrix} \begin{Bmatrix} \ddot{u}_{s,n} \\ \ddot{u}_{f,n} \\ \ddot{\theta}_{f,n} \end{Bmatrix} + \begin{bmatrix} c & 0 & 0 \\ 0 & 0 & 0 \\ 0 & 0 & 0 \end{bmatrix} \begin{Bmatrix} \dot{u}_{s,n} \\ \dot{u}_{f,n} \\ \dot{\theta}_{f,n} \end{Bmatrix} + \begin{Bmatrix} f_{s,n} \\ b_{x,0}u_{f,n} \\ b_{\theta,0}\theta_{f,n} \end{Bmatrix} = - \begin{Bmatrix} m \\ m+m_f \\ mh \end{Bmatrix} \ddot{u}_{FIM,n} - \begin{Bmatrix} 0 \\ \hat{f}_{x,n} \\ \hat{f}_{\theta,n} \end{Bmatrix} \quad (5.12)$$

where

$$\hat{f}_{x,n} = \sum_{j=1}^{J} b_{x,j}u_{x,n-j} - \sum_{j=J}^{l} a_{x,j}f_{x,n-j} \quad (5.13)$$

and

$$\hat{f}_{\theta,n} = \sum_{j=1}^{J} b_{\theta,j}\theta_{f,n-j} - \sum_{j=1}^{J} a_{\theta,j}f_{\theta,n-j}\,. \quad (5.14)$$

Stated in matrix form, these become

$$\boldsymbol{M}_r\ddot{\boldsymbol{u}}_{s,n} + \boldsymbol{C}_r\dot{\boldsymbol{u}}_{s,n} + \boldsymbol{f}_{s,n} = \boldsymbol{p}_{r,n} \quad (5.15)$$

with the subscript r added to the mass and damping matrices and the external force vector to differentiate them from those used in the total displacement formulation of the equations of motion used in Chapters 2 and 4.

Figure 5.7 contains the algorithm used to solve the equations of motion. It is conceptually similar to that used for the fixed base case (Figure 5.5) with the latter's scalar quantities replaced by the appropriate vectors and matrices. There are, however, several changes worth noting. In Step 8 for instance, computation of the the external force includes execution of the recursive filter at each time step without the leading terms, $b_{x,0}$ and $b_{\theta,0}$. Accordingly,

$$\boldsymbol{p}_{r,n} = - \begin{Bmatrix} m \\ m+m_f \\ mh \end{Bmatrix} \ddot{u}_{FIM,n} - \begin{Bmatrix} 0 \\ \hat{f}_{x,n} \\ \hat{f}_{\theta,n} \end{Bmatrix}\,. \quad (5.16)$$

The leading coefficients, associated with the unknown displacement terms at time n, are instead included in the tangent stiffness matrix:

$$\boldsymbol{K}_{t,n} = \begin{bmatrix} k_{t,n} & 0 & 0 \\ 0 & b_{x,0} & 0 \\ 0 & 0 & b_{\theta,0} \end{bmatrix} . \tag{5.17}$$

Also, the scalar residual R from the fixed base algorithm is replaced by the vector residual $\boldsymbol{R}$. The Newton-Raphson iterations continue until the maximum value of this vector is within the desired tolerance.

The time-history response for the SDOF implementation system computed using the filter method is depicted in Figure 5.8. The impedance functions used were those for a rigid disk resting on an elastic half-space outlined in (4.10) and (4.11) and approximated by the coefficients in Table 4.1. Plotted for comparison are the fixed-base inelastic response and substructure inelastic response computed using the convolution method. The filter response generally conforms with the convolution response, exhibiting a maximum displacement of $u_{s,max} = 2.55$ inches and a cumulative energy dissipated through yielding of $E_y = 258.5$ kips compared to the convolution obtained values of $u_{s,max} = 2.46$ inches and $E_y = 280.4$ kips. Table 5.2 compares these values with the fixed base response.

Table 5.2: *Response parameters for MDOF system subjected to horizontal ground motion.*

Model	Cumulative Yield Energy	Max. Structural Displacement [in]
Fixed-Base	663.2	3.17
Convolution	280.4	2.46
Impedance Filter	258.5	2.55

Another means of juxtaposing inelastic responses is through comparison of their force-deformation relationships. Figure 5.9 depicts these for each of the three response histories. The fixed-base case's comparatively greater energy dissipated through yielding is evident in its larger hysteresis loops. As with the displacement versus time plot, the filter and convolution responses generally conform, exhibiting relatively smaller hysteresis loops.

This result tends to confirm the assumption that inertial soil-structure interaction reduces structural response for inelastic systems. Indeed, the substructure system exhibits a lower maximum displacement and less energy dissipated through yielding than that exhibited by the fixed base system. Thus, for the case of this particular soil-foundation-structure system, excited by this ground motion, an engineer could conservatively choose to ignore inertial SSI during the design process. Mylonakis and Gazetas, however, caution that this may not always be the case [2]. For the first application in the following chapter, the filter method is used to explore this assertion and highlight under which conditions inertial SSI may lead to an increase in structural response for inelastic systems.

Select Newmark integration and damping constants: β, γ;

Execute plasticity function to compute initial restive force and tangent stiffness: $f_{s,0}, k_{t,0}$;

Compute initial acceleration: $\ddot{u}_{s,0} = m^{-1}(p_0 - c\dot{u}_{s,0} - f_{s,0})$;

Compute: $a = \frac{1}{\beta\Delta_t}m + \frac{\gamma}{\beta}c$;

Compute: $b = \frac{1}{2\beta}m + \Delta_t\left(\frac{\gamma}{2\beta} - 1\right)c$;

for *Time steps* $n = 2$ *to* $n = N$ **do**

  Guess differential displacement: $\Delta u_{n,s} = 0$;

  Compute differential effective force:$\Delta\hat{p}_n = p_n - p_{n-1} + a\dot{u}_{s,n} + b\ddot{u}_{s,n}$;

  repeat

    Compute current displacement: $u_{s,n} = u_{s,n} - \Delta u_{n,s}$;

    Execute plasticity function to compute resistive force and tangent stiffness: $f_{s,n}, k_{t,n}$;

    Compute residual: $R = \frac{a}{\Delta_t}\Delta u_{s,n} + f_{s,n} - f_{s,n-1} - \Delta\hat{p}_n$;

    Update differential displacement: $\Delta u_{s,n} = \Delta u_{s,n} - \left(\frac{a}{\Delta - t} + k_{t,n}\right)^{-1} R$

  until *Residual is within desired tolerance*;

  Compute current velocity:
  $\dot{u}_{s,n} = \dot{u}_{s,n-1} - \frac{\gamma}{\beta\Delta_t}\Delta u_{s,n} - \frac{\gamma}{\beta}\dot{u}_{s,n-1} + \Delta_t\left(1 - \frac{\gamma}{2\beta}\right)\ddot{u}_{s,n}$;

  Compute current acceleration: $\ddot{u}_{s,n} = \frac{1}{\beta(\Delta_t)^2}\Delta u_{s,n} - \frac{1}{\beta\Delta_t}\dot{u}_{s,n} - \frac{1}{2\beta}\ddot{u}_{s,n}$;

end

Figure 5.5: *Incremental, iterative Newmark integration scheme for inelastic systems. Adapted from Chopra [45].*

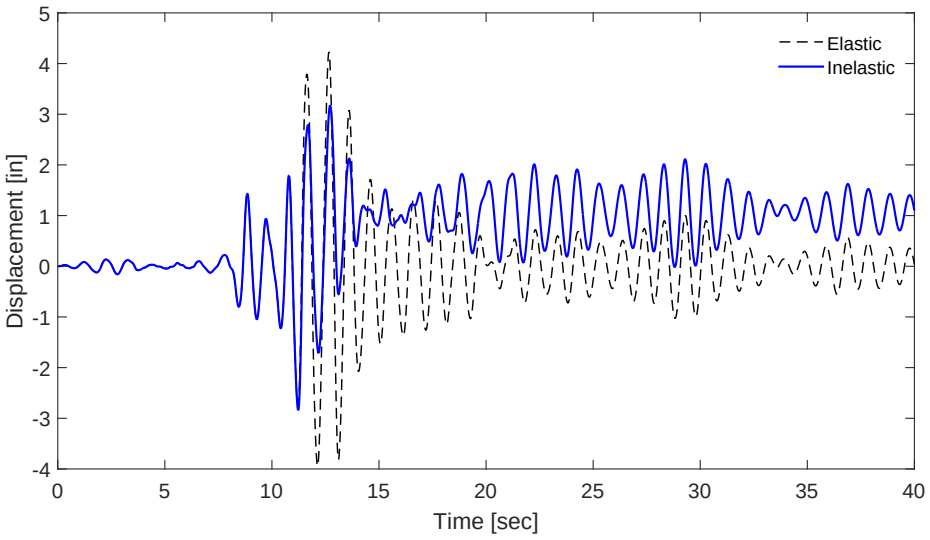

Figure 5.6: *Time history response of fixed-base model of inelastic SDOF soil-foundation-structure system.*

Select Newmark integration and damping constants: β, γ;

Execute plasticity function to compute initial restive force and tangent stiffness: $f_{s,0}, k_{t,0}$;

Compute initial acceleration: $\ddot{\boldsymbol{u}}_{s,0} = \boldsymbol{M}_r^{-1}(\hat{\boldsymbol{p}}_{r,0} - \boldsymbol{C}_r\dot{\boldsymbol{u}}_{s,0} - \boldsymbol{f}_{s,0})$;

Compute: $\boldsymbol{a} = \frac{1}{\beta\Delta_t}\boldsymbol{M}_r + \frac{\gamma}{\beta}\boldsymbol{C}_r$;

Compute: $\boldsymbol{b} = \frac{1}{2\beta}\boldsymbol{M}_r + \Delta_t\left(\frac{\gamma}{2\beta} - 1\right)\boldsymbol{C}_r$;

for *Time steps* $n = 2$ *to* $n = N$ **do**

  Guess differential displacement: $\Delta\boldsymbol{u}_{n,s} = [0\ 0\ 0]^{\mathrm{T}}$;

  Execute filter recursion and compute external force: $\boldsymbol{p}_{r,n}$;

  Compute differential effective force:

  $\Delta\hat{\boldsymbol{p}}_{r,n} = \boldsymbol{p}_{r,n} - \boldsymbol{p}_{r,n-1} + \boldsymbol{a}\dot{\boldsymbol{u}}_{s,n} + \boldsymbol{b}\ddot{\boldsymbol{u}}_{s,n}$;

  repeat

    Compute current displacement: $\boldsymbol{u}_{s,n} = \boldsymbol{u}_{s,n} - \Delta\boldsymbol{u}_{n,s}$;

    Execute plasticity function to compute resistive force and tangent stiffness: $f_{s,n}, k_{t,n}$;

    Assemble internal stiffness force vector: $\boldsymbol{f}_{s,n} = [f_{s,n}\ b_{x,0}u_{f,n}\ b_{\theta,0}\theta_{f,n}]^{\mathrm{T}}$;

    Compute residuals: $\boldsymbol{R} = \frac{\boldsymbol{a}}{\Delta_t}\Delta\boldsymbol{u}_{s,n} + \boldsymbol{f}_{s,n} - \boldsymbol{f}_{s,n-1} - \Delta\hat{\boldsymbol{p}}_{r,n}$;

    Assemble tangent stiffness matrix: $\boldsymbol{K}_{t,n} = \mathrm{diag}[k_{t,n}\ b_{x,0}\ b_{\theta,0}]$;

    Update differential displacement: $\Delta\boldsymbol{u}_{s,n} = \Delta\boldsymbol{u}_{s,n} - \left[\frac{\boldsymbol{a}}{\Delta_t} + \boldsymbol{K}_{t,n}\right]^{-1}\boldsymbol{R}$

  until *Maximum residual is within desired tolerance*;

  Compute current velocity:

  $\dot{\boldsymbol{u}}_{s,n} = \dot{\boldsymbol{u}}_{s,n-1} - \frac{\gamma}{\beta\Delta_t}\Delta\boldsymbol{u}_{s,n} - \frac{\gamma}{\beta}\dot{\boldsymbol{u}}_{s,n-1} + \Delta_t\left(1 - \frac{\gamma}{2\beta}\right)\ \ddot{\boldsymbol{u}}_{s,n}$;

  Compute current acceleration: $\ddot{\boldsymbol{u}}_{s,n} = \frac{1}{\beta(\Delta_t)^2}\Delta\boldsymbol{u}_{s,n} - \frac{1}{\beta\Delta_t}\dot{\boldsymbol{u}}_{s,n} - \frac{1}{2\beta}\ddot{\boldsymbol{u}}_{s,n}$;

end

Figure 5.7: *Incremental, iterative Newmark integration scheme for inelastic systems including impedance filters.*

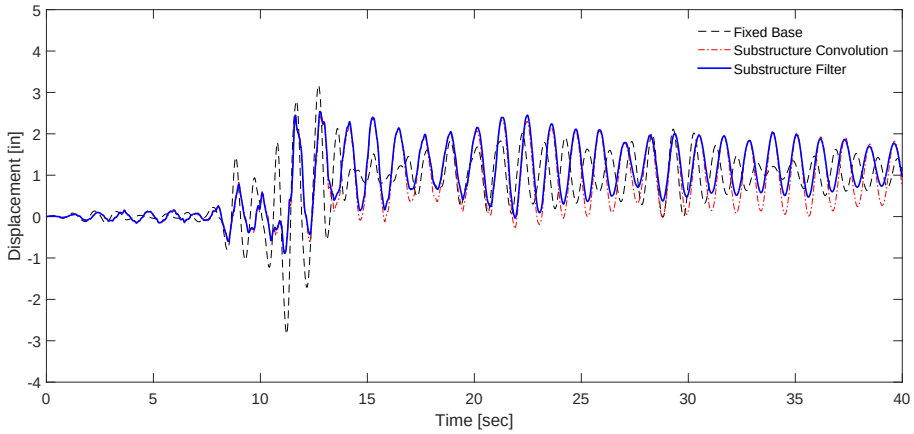

Figure 5.8: *Time history response of substructure model of inelastic SDOF soil-foundation-structure system*

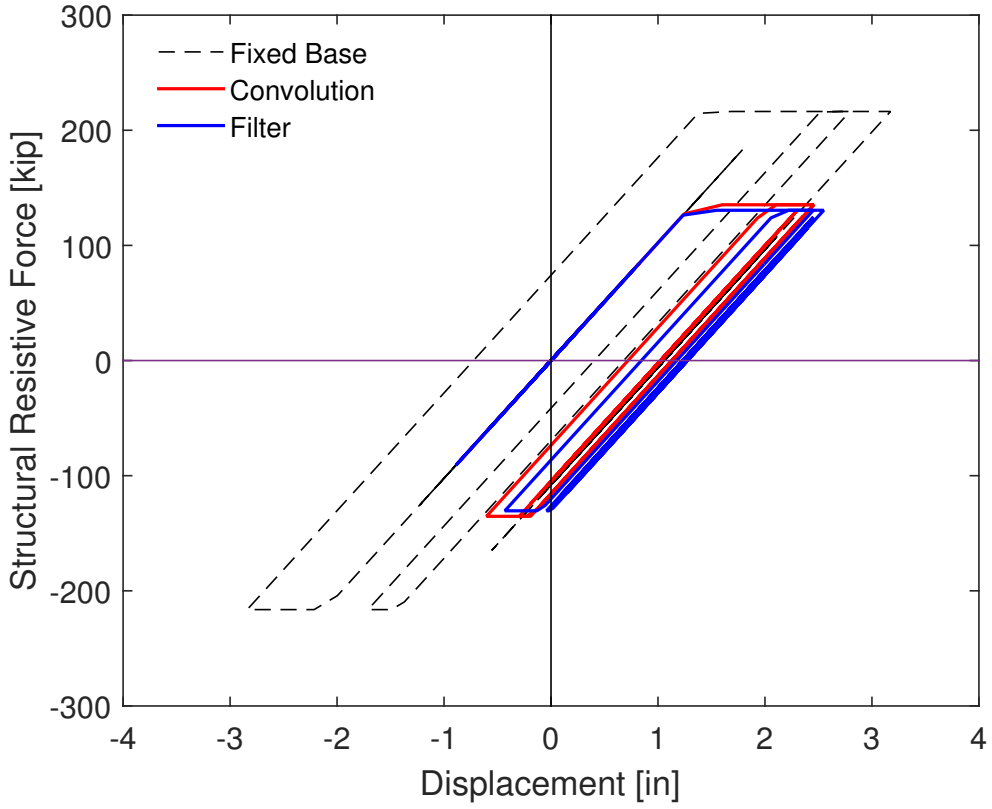

Figure 5.9: *Time history response of fixed-base model of inelastic SDOF soil-foundation-structure system.*

CHAPTER 6

Applications of the Filter Method

This chapter includes three practical applications of the filter method. In the first application, the filter method is used to graphically investigate the effects of inertial SSI on inelastic systems through generation of so-called ductility maps that present a system's ductility demand for a range of both structural and input periods. The maps give insight into the answer of the question "Is inertial SSI beneficial or detrimental?" to inelastic systems. The second application demonstrates how the current state-of-practice for generating constant ductility spectra of inelastic soil-foundation-structure systems can be improved through use of the filter method. The final application is a case study involving the Millikan Library on the campus of The California Institute of Technology that evaluates the filter method's effectiveness in predicting a measured structural response.

6.1 Ductility Mapping: Is Inertial Soil-Structure Interaction Beneficial or Detrimental?

This section borrows its tile from a seminal work published by Mylonakis and Gazetas in 2000 entitled *Seismic Soil-Structure Interaction: Beneficial or Detrimental?* In it, the authors challenged the prevailing notion that consideration of inertial soil-structure interaction leads to a decrease in structural response for yielding systems. Exemplifying this, *Minimum Design Loads for Buildings and other Structures - ASCE 7-10* states that "an SSI reduction shall be permitted

where determined using Chapter 19 or other generally accepted procedure approved by the authority having jurisdiction [37]." Mylonakis and Gazetas asserted that for short period inelastic structures excited by long period motion, such a reduction is not appropriate. They further demonstrated that such systems may indeed experience a significant increase in structural response as compared to the fixed base case. The filter method offers a means of investigating this assertion through generation of ductility maps.

Ductility maps, shown in Figure 6.1, are a graphical representations of the effects of soil-structure interaction on a system's ductility demand. Recall from

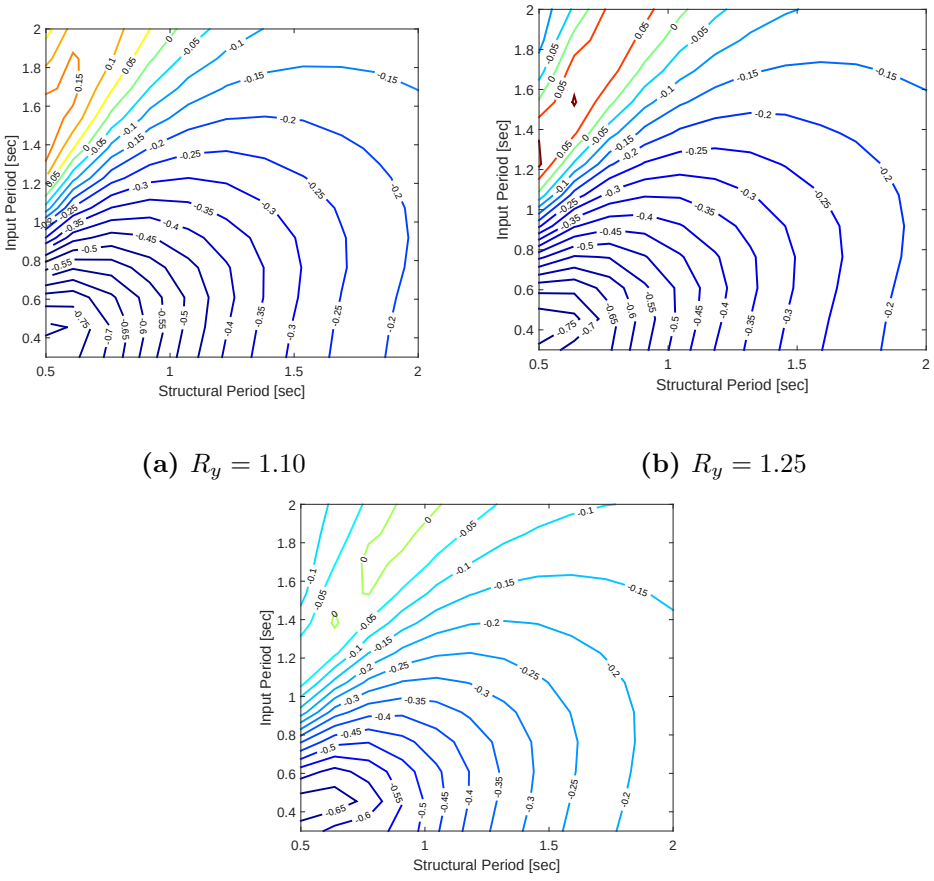

(a) $R_y = 1.10$ **(b)** $R_y = 1.25$

(c) $R_y = 1.50$

Figure 6.1: *Ductility maps for various yield strengths strength reduction factors.*

(5.5) that ductility demand is the ratio of a structure's maximum inelastic deformation to its yield deformation. Ductility demands greater than one indicate a yielding system, while ductility demands less than or equal to one indicate that a given system has remained elastic. The maps in Figure 6.1 were generated by comparing a system's the fixed base ductility demand to a relative ductility demand computed for the corresponding substructure model at various structural and input periods. The SSI ductility demands are qualified as relative as they are computed using the ratio of inelastic SSI deformation to fixed base yield deformation.[1] Each map is created for a unique yield strength reduction factor R_y of a given soil-foundation-structure system. Figure 6.1 shows maps generated for $R_y = 1.10, 1.25,$ and 1.50 for the soil-foundation-structure system depicted in Figure 5.2 subject to the parameters in Table 5.2. The filter coefficients used are those found in Table 4.1. The plotted data represent a ductility demand reduction ratio R_μ computed as

$$R_\mu = \frac{\tilde{\mu}_r - \mu}{\mu} \tag{6.1}$$

in which μ represents fixed base ductility demand and $\tilde{\mu}_r$ represents SSI ductility demand relative to fixed based yield deformation. Thus, values of R_μ less than one represent cases where the effects of SSI are beneficial in that they reduce the ductility demand compared to that generated by the fixed base case. Conversely, values over one indicate instances where the effects SSI are detrimental, increasing ductility demand.

For each map, structural period is varied via modifying structural stiffness according to (2.6). The inputs are supplied through use of a suite of Ricker

[1]Typically SSI-related ductility demands are computed as the ratio of inelastic SSI deformation to yield deformation computed as a percentage of maximum deformation of the corresponding elastic SSI system [7]. This relative ductility demand uses of the same yield strength for the fixed base and SSI cases, allowing the effects of SSI to be quantified as the difference between the fixed base and relative ductility demands.

wavelets generated according to

$$\ddot{u}_{g,n} = g\left(1 - \frac{\tau^2\pi^2}{T_p}\right) e^{\left(\frac{T_p}{\tau^2\pi^2}\right)} \tag{6.2}$$

where

$$\tau = n\Delta t - t_0\,, \tag{6.3}$$

and t_0 represents the desired central time of the pulse and g represents the acceleration due to gravity. Figure 6.2 depicts the time history and Fourier amplitude spectrum of such a wavelet with a predominant period of $T_p = 1$ and central time of $t_0 = 10$ seconds. Based on the work of geophysicist Norman Ricker [49], Ricker

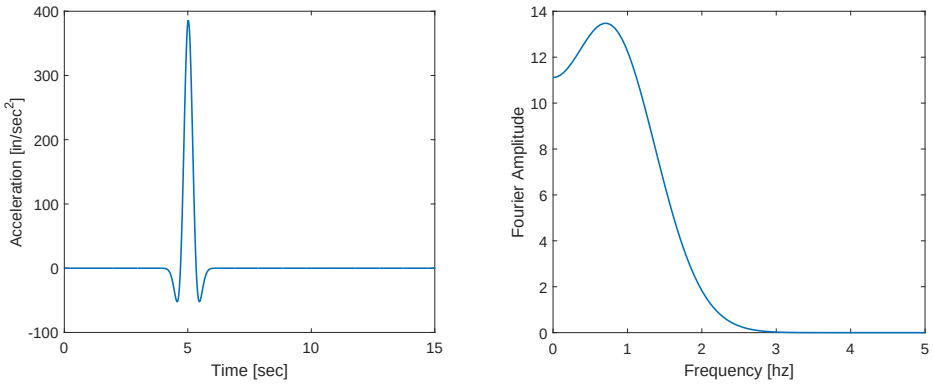

(a) Time history **(b)** Fourier Amplitude Spectrum

Figure 6.2: *Ricker wavelet with predominant period* $T_p = 1.0$ *seconds*

wavelets offer an approximation of the frequency content of seismic motion. They do not, however, replicate the complexity of naturally occurring seismic records. For this reason, the ductility maps found in Figure 6.1 should be considered only as demonstrations, and not as design tools. They do, however offer insight into the behavior of inelastic SSI systems.

All three maps tend to confirm the assertion that short period structures subjected to long period ground motions may exhibit increased ductility demands when soil-structure interaction is considered. On the plots, yellow regions indicate those where the SSI ductility demands are higher than their fixed base counter

parts. As Mylonakis and Gazetas claimed, these are generally confined to regions corresponding to lower structural periods and higher input periods. Interestingly, on Figures 6.1(b) and 6.1(c) the regions corresponding to the lowest structural periods paired with the highest input periods show the relative ductility as lower than their fixed base counterparts.

It is of course possible to use the filter method to verify the ductility maps using ground motion records. Table 6.1 contains ductility data from four ground motion records with various predominant periods. Included are two longer period records from the 1994 Kobe, Japan earthquake recorded in Fukushima and on the campus of Kobe University and two shorter period records, one recorded in Tarzana during the 1994 Northridge earthquake with the other being the Loma Prieta 1989 motion used in previous examples. While the ratios displayed in the table do not exactly match those displayed in Figure 6.1, they do follow their general trend.

So, is inertial soil-structure interaction beneficial or detrimental? Based on this demonstration, the answer is that in most cases inertial SSI is indeed beneficial for inelastic systems. For most structural period-input period pairs ductility demand is reduced when inertial SSI is considered in dynamic analyses. However, just as Mylonakis and Gazetas asserted, it is possible that for short period structures subjected to long period motions the effects inertial SSI has the potential to induce increased ductility demands. For this reason, engineers should use extreme caution when applying blanket strength reduction factors during they design process.

Table 6.1: *Ductility demand ratios for four ground motion records at various structural periods*

Event / Station	Predominant Period [sec]	Structural Period [sec] 0.60	1.2	1.8
	$R_y = 1.10$			
Kobe 1994 / Fukushima	2.11	0.22	−0.03	−0.08
Kobe 1994 / Kobe University	1.35	0.31	−0.07	−0.19
Northridge 1994 / Tarzana	0.67	−0.62	−0.21	-0.14
Loma Prieta 1989 / SFA	0.35	−0.72	−0.23	−0.14
	$R_y = 1.25$			
Kobe 1994 / Fukushima	2.11	0.32	−0.06	−0.07
Kobe 1994 / Kobe University	1.35	0.10	−0.01	−0.20
Northridge 1994 / Tarzana	0.67	−0.60	−0.10	−0.16
Loma Prieta 1989 / SFA	0.35	−0.68	−0.25	−0.08
	$R_y = 1.50$			
Kobe 1994 / Fukushima	2.11	−0.13	−0.13	−0.01
Kobe 1994 / Kobe University	1.35	0.16	−0.05	0.14
Northridge 1994 / Tarzana	0.67	−0.65	−0.08	−0.14
Loma Prieta 1989 / SFA	0.35	−0.70	−0.15	−0.03

6.2 Design Application: Constant Ductility Spectra

Response spectra are tools widely used in earthquake engineering design [50]. Figure 6.3 contains the pseudo-acceleration response spectrum of an elastic, fixed base, single degree of freedom system. The plot depicts the maximum value of

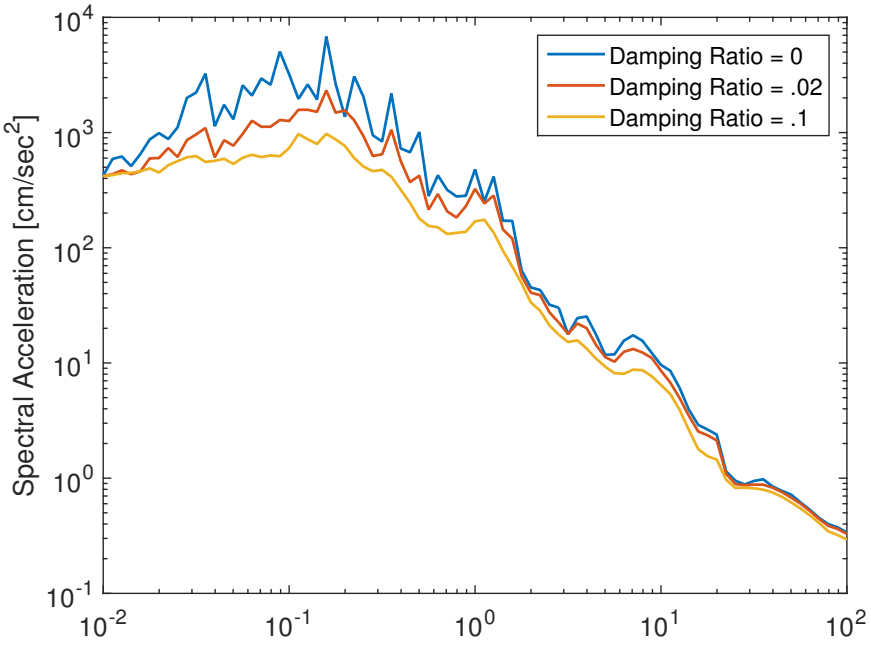

Figure 6.3: *Pseudo-acceleration response spectrum for an elastic fixed base single degree of freedom system.*

the system's pseudo-acceleration (where pseudo indicates the acceleration was computed via the system's base shear vice directly measured from the response history) for a range of structural periods and damping ratios. Each response spectrum is generated using a single ground motion. Often spectra from a suite of ground motions representative of those expected a particular site are averaged to give a general indication of how a structure will perform.

Computation of elastic spectra are straightforward. The response history is computed for each structural period. The spectral ordinates are than taken as

the maximums of the desired response quantities from each history. Computation of spectra for inelastic systems however, is more complicated. They are typically calculated for a constant ductility demand. As the relationship between yield strength and ductility is not necessarily linear in nature, an iterative procedure is required [45].

Inclusion of inertial SSI effects requires only slight modification of the established fixed base inelastic procedures. The difficulty lies in response history computation. Generation of a viable response spectrum requires computation of response histories over a wide range of structural periods, often varying from as low as 0.01 seconds to as high as five seconds (or higher). The frequency domain cannot be used as a solution method. The period range inhibits use of a single representative frequency. Recent works use replacement oscillators [39] and lumped parameter models [51–54] to generate response histories. These methods are limited to the foundation-soil characteristics of the models used to generate them, in most cases a rigid foundation embedded in a homogeneous half-space or soil layer. The filter method can leverage the advances in impedance function computation methods to improve these methods through generation of spectra for arbitrary foundation shapes and soil profiles.

6.2.1 Formulation

In general, constant ductility spectra are generated according to the algorithm outlined in Figure 6.4. To begin, a target ductility demand is selected. Next, for each desired structural period, the yield strength leading to that target ductility demand is calculated. As the algorithm shows, this is done through both interpolation and iteration. Lines 5 though 10 accomplish the interpolation lines 11 through 17 the iteration. The interpolation produces a initial estimate of the yield strength leading to the target ductility demand. The iteration then adjusts this estimate until the residual is within a desired tolerance. Note that the factor

10 in line 16 is selected based on the relationship between the magnitude of the normalized yield strength and ductility demand and may need to be customized to assure convergence.

6.2.2 Implementation

Consider the soil-foundation-structure system and its substructure model depicted in Figure 6.5. They are similar to that of Figure 5.2 with the exception that the elastic soil half-space is replaced by a soil layer over an elastic soil half-space with a contrasting elastic modulus such that E_1:E_2 = 1:4, in which E_1 represents the elastic modulus of the layer and E_2 represents the elastic modulus of the underlying half-space. The relevant parameters for this model are given in Table 6.2. The

Table 6.2: *System Parameters for inelastic soil-foundation-structure system with layered soil profile.*

Geology	
E_1: Shear Modulus of Upper Soil Layer	1×10^9 N/m^2
E_2: Shear Modulus of Lower Soil Layer	4×10^9 N/m^2
Structure	
μ: Ductility Demand	4.0
w: Structure Weight	22×10^3 kN
ξ: Damping Ratio	0.05
h: Structure Height	15 m
w_f: Foundation Weight	22×10^2 kN
b: Foundation Width	7.5 m
d: Foundation Thickness	1 m

constant ductility spectrum will be generated using the ground motion recorded at the Imperial Valley Irrigation District substation in El Centro, California during the 1940 Imperial Valley Earthquake. The record's acceleration history and Fourier amplitude spectrum are depicted in Figure 6.6.

Previous studies have offered means of approximating constant ductility spectra for such a system, but they rely lumped parameter models generated for rigid foundations resting on either an elastic soil half-space or a finite soil layer over bedrock. As such they are only approximations and do not necessarily represent the true foundation geometry or site conditions. Recent advances in computational methods have offered means of generating impedance functions for more complicated soil profiles and foundation geometries. One such work by Jeong et al. [3] reports impedances for foundations resting on layered media with various impedance contrasts. Figure 6.7 displays the real and imaginary components of the horizontal and rocking impedance functions for this system generated according to this method. Plotted for comparison are the impedance functions for the same foundation resting on an elastic half-space, denoted by E_1:E_2 = 1:1. The impedance functions for the contrasting layers exhibit significantly more variation with respect to frequency (especially for the horizontal case) than those for the uniform half-space due to reflection at the layer interface. The filter method can accommodate this variation through careful filter design. Figure 6.8 shows the fit of 17th order filters approximating both the horizontal and rocking impedance function for the 1:4 case. Likewise, Figure 6.9 shows the fits for the filters approximating the impedance functions for the 1:1 case. The coefficients corresponding to both sets of filters are contained in Table 6.3.

6.2.3 Analysis

Figure 6.10 depicts three sets of constant ductility spectra for this system. The solid black line represents the spectrum for case with a 1:4 contrast in elastic

modulus between the soil layer and the underlying half-space. The dashed red line represents the case without impedance contrast. The dashed blue line represents the fixed base case. All three spectra were generated using using the algorithm outlined in Figure 6.4 with a set of ten trial yield strengths evenly spaced from 0.1 to 1.0. The system was excited using the the north-south component of the May 18, 1940 Imperial Valley earthquake as recorded at the Imperial Valley Irrigation District Substation in El Centro, California [45]. The three spectra generally agree at relatively high structural periods. This is to be expected as long period structures are generally less susceptible to the effects of inertial SSI than those with shorter periods. Indeed, at shorter periods, the spectra diverge, especially so at periods less than half of a second. Of special note is the difference between the contrasting moduli case and the constant moduli case. At these low periods the contrasting moduli case demonstrates a marked increase in yield strength as compared to the constant moduli case. At a period of 0.5 seconds the contrasting case is approximately ten percent higher. At 0.2 seconds it is nearly seventy-five percent higher.

This result is indeed significant. It shows that soil profile can play an important role in structural response to ground motion. As computational techniques continue to improve, giving design engineers will have better access to site specific impedance functions. The filter method offers them a means of incorporating such functions into the design process.

```
Select desired target ductility demand: μ_target;
for each structural period T_n do
    Compute elastic response history: u_{n,elastic};
    Determine maximum elastic displacement: u_{max,elastic};
    for each trail normalized yield strength f̄_{y,j} do
        Compute inelastic response history response history: u_{n,inelastic};
        Determine maximum inelastic displacement: u_{max,inelastic};
        Compute ductility demand: μ_j;
    end
    Interpolate normalized yield strength assuming linear relationship
    between log(f̄_{y,j}) and log(μ_j): f̄_y;
    repeat
        Compute inelastic response history: u_{n,inelastic};
        Determine maximum inelastic displacement: u_{max,inelastic};
        Compute trial ductility demand: μ_trial;
        Compute residual: R = (μ_target − μ_trial) / μ_target;
        Update normalized yield strength: f̄_y = f̄_y − 10R f̄_y;
    until Residual R is within desired tolerance;
end
```

Figure 6.4: *Algorithm for computation of constant ductility spectrum*

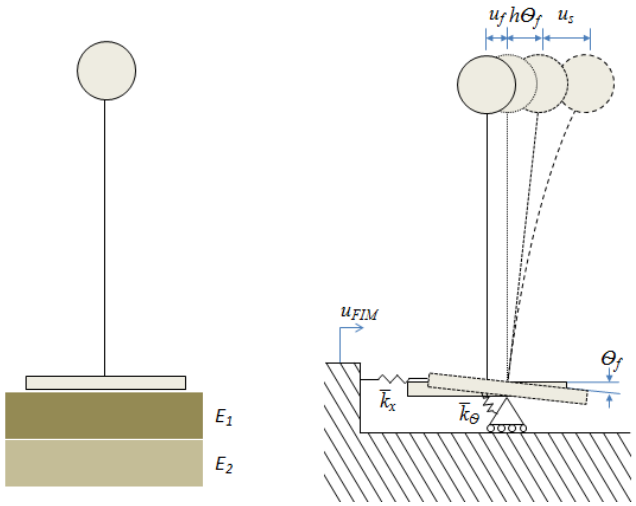

(a) Soil-Foundation-Structure System

(b) Substructure Model

Figure 6.5: *SDOF Structure with rigid foundation resting on layered soil.*

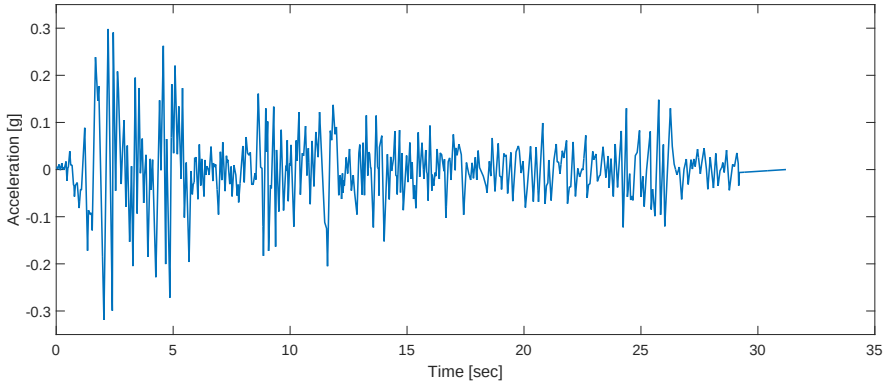

(a) Acceleration History

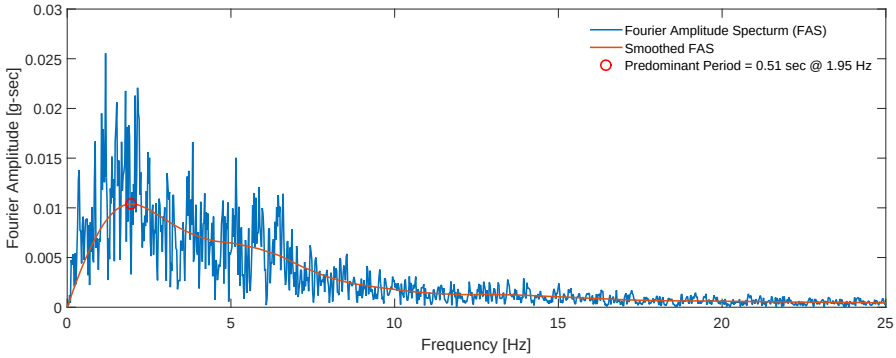

(b) Fourier Amplitude Spectrum

Figure 6.6: *Horizontal ground motion as recorded at the Imperial Valley Irrigation District substation in El Centro, California during the 1940 Imperial Valley Earthquake.*

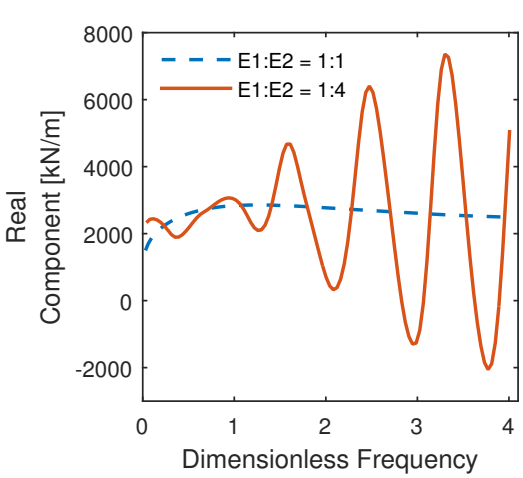

(a) Real Component of Horizontal Impedance

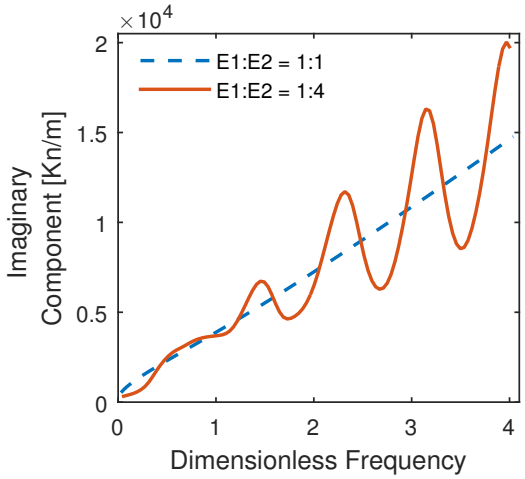

(b) Imaginary Component of Horizontal Impedance

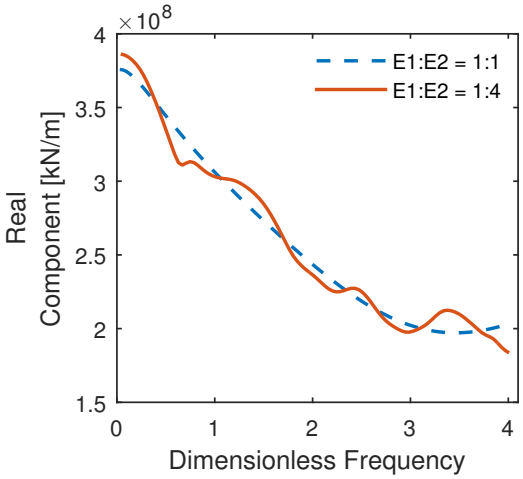

(c) Real Component of Rocking Impedance

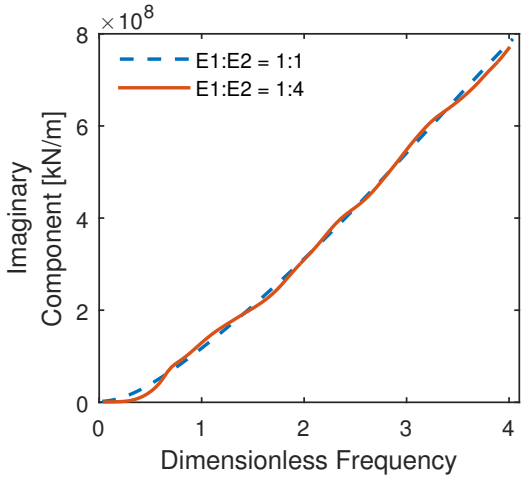

(d) Imaginary Component of Rocking Impedance

Figure 6.7: *Horizontal and rocking impedance functions for rigid foundation resting on soil layer above uniform half-space.*

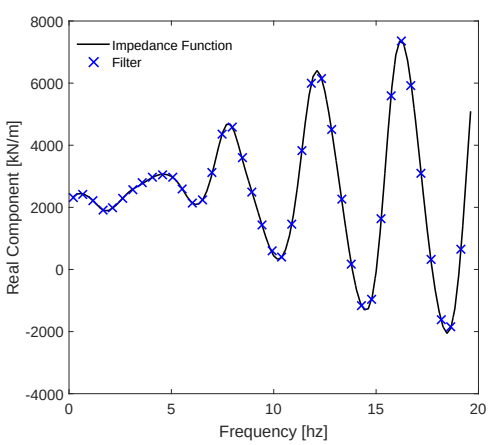

(a) Real Component of Horizontal Impedance

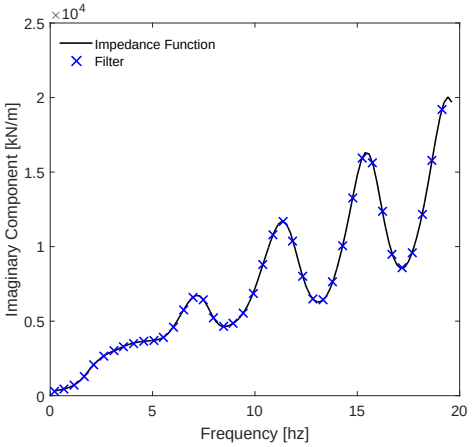

(b) Imaginary Component of Horizontal Impedance

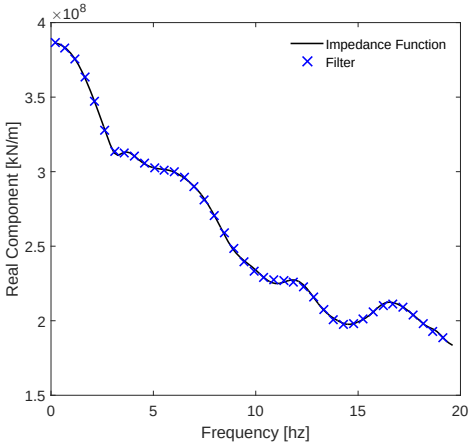

(c) Real Component of Rocking Impedance

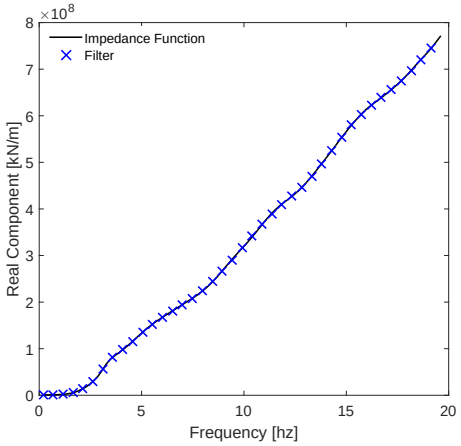

(d) Imaginary Component of Rocking Impedance

Figure 6.8: *Discrete-Time filters approximating horizontal and rocking impedance functions for rigid foundation resting on soil layer over uniform half-space with modulus contrast 1:4.*

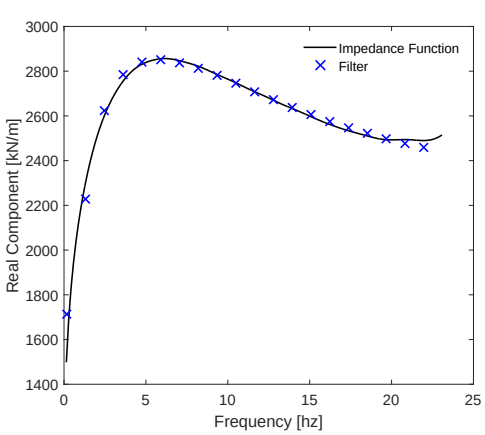

(a) Real Component of Horizontal Impedance

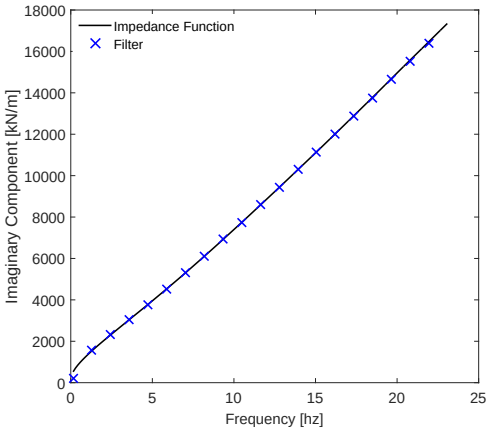

(b) Imaginary Component of Horizontal Impedance

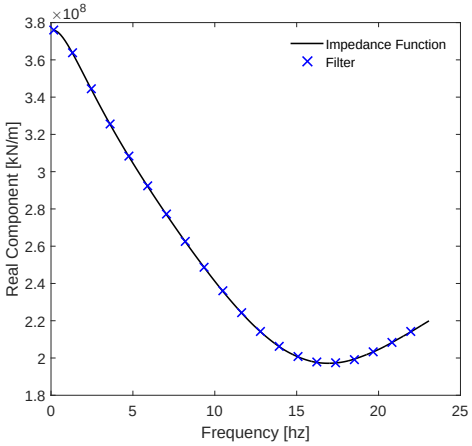

(c) Real Component of Rocking Impedance

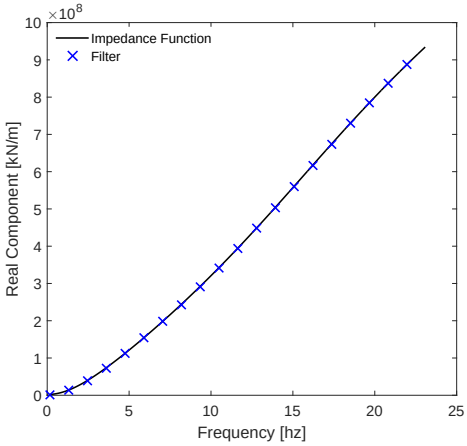

(d) Imaginary Component of Rocking Impedance

Figure 6.9: *Discrete-Time filters approximating horizontal and rocking impedance functions for rigid foundation resting on soil layer over uniform half-space with modulus contrast 1:1.*

Table 6.3: *Coefficients of discrete-time filters approximating horizontal and rocking impedance functions for rigid foundation resting on soil layer over uniform half-space.*

	$E_1 : E_2 = 1 : 1$				$E_1 : E_2 = 1 : 4$			
	Horizontal		Rocking		Horizontal		Rocking	
j	$a_{x,j}$	$b_{x,j}$ $(\times 10^{-4})$	$a_{\theta,j}$	$b_{\theta,j}$ $(\times 10^{-9})$	$a_{x,j}$	$b_{x,j}$ $(\times 10^{-4})$	$a_{\theta,j}$	$b_{\theta,j}$ $(\times 10^{-9})$
0	1.0000	1.3580	1.0000	0.8353	1.0000	0.9790	1.0000	0.6605
1	0.253	−1.8521	−0.6324	−1.6281	−0.0269	−1.4499	0.1209	−0.6278
2	−0.7869	0.5653	−0.0345	1.8677	1.6373	2.9665	0.6589	1.1551
3	−0.0475	0.0000	-0.2403	−2.0731	−1.0800	−4.6578	−0.0826	−1.1906
4			−0.6013	1.6078	1.1351	5.8549	0.2907	1.4394
5			0.6621	−0.9338	−1.981	−7.7527	0.5458	−1.0351
6			−0.3413	0.4213	0.6444	8.3533	−0.0463	0.9886
7			0.2016	−0.1432	−1.4347	−8.683	0.4495	−0.5684
8			−0.0346	.06280	0.8028	8.5001	−0.2179	0.3850
9			0.03910	−0.0180	−0.5002	−7.2833	0.2344	−0.1419
10			−0.0008	0.0031	0.7255	6.1266	−0.0726	0.0645
11			−0.0097	0.0000	−0.2832	−4.5462	0.0387	0.0000
12					0.3484	3.0262		
13					−0.3516	−1.9689		
14					0.0819	0.942		
15					−0.2527	−0.4459		
16					0.0178	0.1273		
17					−0.0627	0.0000		

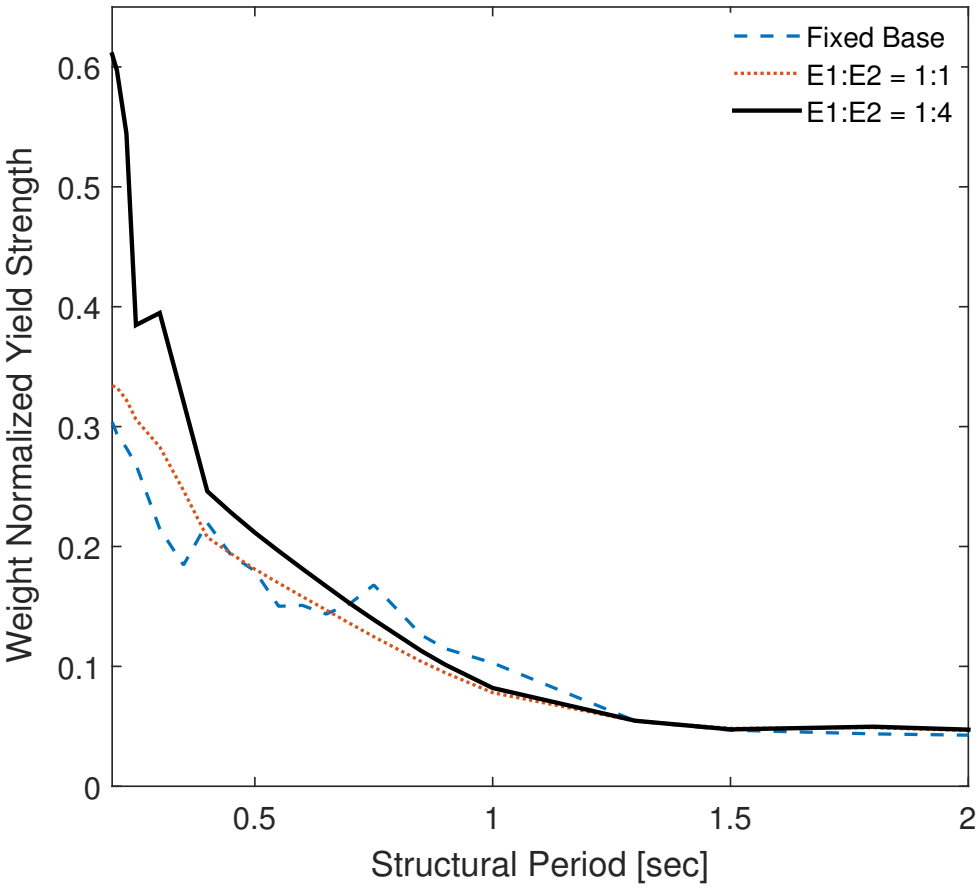

Figure 6.10: *Constant ductility spectrum for single degree of freedom structure with rigid foundation resting on soil layer above uniform half-space.*

6.3 Case Study: Millikan Library

The Millikan Library on the Campus of the California Institute of Technology has been the subject of numerous investigations since its construction in 1967. It's relatively simple structural plan and thorough instrumentation make it ideal for both ambient and force vibration analyses. The goal of this study is not to add to this body of knowledge, but to instead take advantage of the wealth of published information to demonstrate the use of the filter method on an actual structure. Specifically, this study aims to use both analytical and experimental impedance data to predict the structure's north-south response as recorded during the 2002 Yorba Linda Earthquake. As with previous studies in this work, the effects of kinematic interaction are ignored. In this case, the due to the unavailability of a viable free-field motion, the recorded foundation motion is used as the foundation input motion.

6.3.1 The Structure

The Millikan Library, pictured in Figure 6.11(a), is a nine-story reinforced concrete structure with a single-story basement. Figures 6.11(b) and 6.11(d) depict the building's north-south structural elevation a typical story plan respectively. Its total height as measured from ground level to the roof is 39.6 meters. Including the basement, the total height is 43.9 meters. Its length is 21.5 meters in the north-south direction and 23.42 meters in the east-west direction. The structure resists later forces in the north-south direction through shear walls located along its east and west faces. It resist east-west lateral motion through the central elevator core. Further detail on the structural system may be found in Kuriowa's thesis [56].

The library's foundation, shown in Figure 6.11(c), consists of a central pad 9.75 meters wide and 1.22 meters deep running with width of the building from

in the east-west direction flanked on each side by continuous foundation beams, each 3 meters wide and 0.6 meters deep. The foundation beams are connected to the pad via stepped beams as shown in the foundation elevation.

6.3.2 The Site

Data for the geology and soil profile for the Millikan Library site comes from two primary sources. A site investigation as part of construction was conducted in 1959 by Converse Foundation Engineers of Pasadena, California, the results of which are summarized by in Reference [57]. A subsequent investigation was undertaken after the San Fernando Earthquake of 1970, by Eguchi [58] and summarized in Wong et al. [59]. The values pertinent to this study are presented in Table 6.4

Table 6.4: *Key soil parameters of the Millikan Library site.*

Unit Weight [kN/m^3]	19.2
Shear Wave Velocity [m/sec]	382
Shear Modulus [kN/m^2]	2.86×10^5
Poisson's Ratio	0.25

6.3.3 Substructure Model

The substructure model used in this study for the Millikan Library soil-foundation-structure system is based on that offered by Foutch and pictured in Figure 6.12 [55]. The model consists of a 10 story shear building modeling the structure's first floor through roof, resting on a rigid foundation that is attached to a fixed reference through both horizontal and rotational impedance functions. Table 6.5 contains the values used for the structural model. The story heights and weights are taken from Kuroiwa [56]. The story stiffnesses were derived from the model

Table 6.5: *Millikan Library shear building model parameters.*

Story	B	1	2-9	Roof
Height [m]	4.27	4.88	4.27	4.88
Weight [kN]	10141	8674	8674	11565
Stiffness [MN/m]	3170	2120	3170	2200

of a cantilever shear beam as outlined by Foutch [55]. The model includes 1.8 percent viscous structural damping which is consistent with the values identified by both Kuroiwa [56] and later, Luco et al. [60]. The foundation mass moment of inertia for rotation about the east-west axis is assumed to be $1.1264 \times 10^5 \mathrm{m}^4$.

This study uses two sets of foundation impedance functions, one analytically computed, and the other experimentally identified. The analytical impedances are taken from the 1988 study by Wong et al. [59]. For this work, they calculated horizontal, rotational, and coupling foundation impedance functions according to Apsel and Luco's method for rigid foundations embedded in layered media [61]. The second set were identified by Luco et al. (also in 1988) through forced vibration testing [60],. These identified impedances include only those for horizontal and rocking motions. Both sets of impedance functions are shown in Figure 6.13. The impedance magnitudes are normalized by soil shear modulus and an effective foundation radius L such that

$$\bar{k}_x = GL[\Re(k_x) + i\Im(k_x)a_0]\,, \tag{6.4}$$

$$\bar{k}_\theta = GL[\Re(k_\theta + i\Im(k_\theta)a_0]\,, \quad \text{and} \tag{6.5}$$

$$\bar{k}_{\theta x} = \bar{k}_{x\theta} = GL[\Re(K_{x\theta}) + i\Im(k_{x\theta})a_0] \tag{6.6}$$

represent horizontal, rocking, and coupling impedances, respectively, where the operators $\Re$ and $\Im$ denote the real and imaginary parts of their complex-valued

arguments. The value for shear modulus is taken from Table 6.4. The value for effective radius is taken as $L = 13.7$ m. Dimensionless frequency is calculated according to

$$a_0 = \frac{\omega L}{V_s} \tag{6.7}$$

with ω representing continuous angular frequency and V_s representing shear wave velocity, which is also taken from Table 6.4.

Table 6.6 contains the coefficients of the discrete-time filters approximating the analytical impedance functions.

Table 6.6: *Coefficients for discrete-time filter approximating Millikan Library analytical impedance functions.*

	Horizontal		Rocking		Coupling	
j	$a_{x,j}$	$b_{x,j}$ $(\times 10^{-7})$	$a_{\theta,j}$	$b_{\theta,j}$ $(\times 10^{-7})$	$a_{c,j}$	$b_{c,j}$ $(\times 10^{-6})$
0	1.0000	3.2942	1.0000	2.2688	1.0000	0.9622
1	−0.0961	−1.4007	1.0811	2.2568	2.5687	2.4254
2	0.1782	1.9524	0.0509	0.0943	4.7470	4.4074
3	0.8044	1.0238	−0.1922	−0.4964	5.9521	5.4558
4	−0.4066	−0.5861	0.4810	1.2239	6.4415	5.8394
5	0.0610	0.0000	0.9874	2.0993	5.6585	5.1017
6			0.1843	0.4329	4.7246	4.2644
7			−0.2590	−0.6619	3.1723	2.8230
8			0.0635	0.2548	2.0402	1.8090
9			0.7184	1.5684	0.8989	0.7275
10			0.5143	1.0945	0.4178	0.3375
11			−0.1210	−0.3784	0.0478	0.0000
12			0.0089	−0.0205		
13			0.0137	0.0000		

The curve fits for these filters are shown in Figure 6.14. Likewise, the coefficients of the filters approximating the identified impedance functions are found in Table 6.7 with the curve fits shown in Figure 6.15. According to the conventions

Table 6.7: *Coefficients for discrete-time filter approximating Millikan Library identified impedance functions.*

	Horizontal		Rocking	
j	$a_{x,j}$	$b_{x,j}$ $(\times 10^{-7})$	$a_{\theta,j}$	$b_{\theta,j}$ $(\times 10^{-7})$
0	1.0000	2.0341	1.0000	1.9770
1	1.0379	1.2621	2.7033	5.2900
2	0.1426	0.7343	2.5134	4.7987
3	0.5824	0.5142	−0.6957	−1.6501
4	0.9834	2.5826	−3.2433	−6.7362
5	0.9624	0.7360	−2.0504	−4.4245
6	0.3434	1.3950	1.0940	1.7634
7	0.2224	−0.2288	2.1291	3.8708
8	0.8269	2.0844	1.0147	1.8377
9	0.1644	−0.2394	0.0643	0.1025
10	−0.2516	−0.1077	−0.0066	0.0000
11	0.0453	0.0000		

outlined in Chapter 4, the equations of motion for this system are

$$\begin{bmatrix} \boldsymbol{M}_s & \boldsymbol{M}_{sf} \\ \boldsymbol{M}_{fs} & \boldsymbol{M}_f \end{bmatrix} \begin{Bmatrix} \ddot{\boldsymbol{u}}_s \\ \ddot{\boldsymbol{u}}_f \end{Bmatrix} + \begin{bmatrix} \boldsymbol{C}_s & \boldsymbol{C}_{sf} \\ \boldsymbol{C}_{fs} & \boldsymbol{C}_f \end{bmatrix} \begin{Bmatrix} \dot{\boldsymbol{u}}_s \\ \dot{\boldsymbol{u}}_f \end{Bmatrix} + \begin{bmatrix} \boldsymbol{K}_s & \boldsymbol{K}_{sf} \\ \boldsymbol{K}_{fs} & \hat{\boldsymbol{K}}_f \end{bmatrix} \begin{Bmatrix} \boldsymbol{u}_s \\ \boldsymbol{u}_f \end{Bmatrix} = \begin{bmatrix} \boldsymbol{P}_{s,n} \\ \boldsymbol{P}_{f,n} + \hat{\boldsymbol{F}}_{f,n} \end{bmatrix} \tag{6.8}$$

where

$$\hat{\boldsymbol{K}}_f = \begin{bmatrix} k_1 + b_{x,0} & b_{c,0} \\ b_{c,0} & \sum k_j h_j^2 + b_{\theta,0} \end{bmatrix} \quad \hat{\boldsymbol{F}}_{f,n} = \begin{bmatrix} \hat{f}_{x,n} \\ \hat{f}_{\theta,n} \end{bmatrix}$$

$$\hat{f}_{x,n} = \sum_{j=1}^{J} b_{x,j} u_{f,n-j} - \sum_{j=1}^{J} a_{x,j} f_{x,n-j} + \sum_{j=1}^{J} b_{c,j} u_{f,n-j} - \sum_{j=1}^{J} a_{c,j} f_{c,n-j}$$

$$\hat{f}_{\theta,n} = \sum_{j=1}^{J} b_{\theta,j} \theta_{f,n-j} - \sum_{j=1}^{J} a_{\theta,j} f_{\theta,n-j} + \sum_{j=1}^{J} b_{c,j} \theta_{f,n-j} - \sum_{j=1}^{J} a_{c,j} f_{\theta,n-j} \, .$$

6.3.4 Excitation and Recorded Motion

The ground motion used for this study is that generated by the 4.8 magnitude Yorba Linda Earthquake on September 3rd, 2002 and recorded by the USGS Station No. 5407, instrument 134, channel 4 in the basement of Millikan Library at a distance of 40.5 kilometers from the epicenter. Figure 6.16 displays the record's Fourier amplitude spectrum. The pending simulation results will be compared against the displacement and acceleration records measured by instrument 133, channel 18 on the library's roof.

6.3.5 Results and Discussion

Figures 6.17 and 6.18 show the simulation results for both substructure models. Figure 6.17(a) compares total roof displacement calculated using the analytical impedance substructure model with the measured displacement response. The two signals generally agree with both displaying predominant periods of 0.60 seconds. The simulated displacement does, however show a more damped response with a maximum displacement of 4.14 cm as compared to a measured maximum of 6.49 cm. Figure 6.17(b) compares the signals' Fourier amplitudes along with that of the structure's simulated fixed base response. Again, the signals generally agree, both showing lengthening of period as compared to the fixed base case. Figure 6.18(a) compares the total roof displacement calculated using the identified impedance

substructure model. As with the analytical case, the signals generally match, both displaying predominant periods of 0.60 seconds. Also like the analytical case, the identified shows a relatively damped response, in this case with a maximum displacement of 5.08 cm. These results are confirmed by the Fourier amplitudes shown on Figure 6.18(b). Figure 6.19 directly compares the Fourier amplitudes of the two simulated signals with that of the measured response. For both simulated signals, the largest deviation from the measured signal comes at low frequencies.

Thus, based solely on roof displacement, both substructure models appear to comparably approximate the measured response. A look at roof acceleration response however, casts doubt this result. Figure 6.20 compares the Fourier amplitudes of the acceleration time-histories of both substructure models with the that of the measured roof acceleration. From this figure, it is readily apparent that the models are not, in fact, equal. The identified model displays significant frequency content at around seven hertz that is not found in either the signal of either analytical model or the measured response. Indeed, the identified model's maximum acceleration of 16.78 meters per second is nearly double that of the analytical model's 8.36 meters per second and the measured response's 8.48 meters per second.

Table 6.8 summarizes the key parameters for each time history response.

Table 6.8: *Key response parameters for Millikan Library when excited by the 2002 Yorba Linda Earthquake.*

	Predominant Period [sec]	Maximum Displacement [cm]	Maximum Acceleration [m/sec]
Measured	0.60	6.49	8.48
Analytical Substructure	0.60	4.14	8.36
Identified Substructure	0.60	5.08	16.78
Fixed Base	0.55	3.97	4.72

(a) View looking north-west

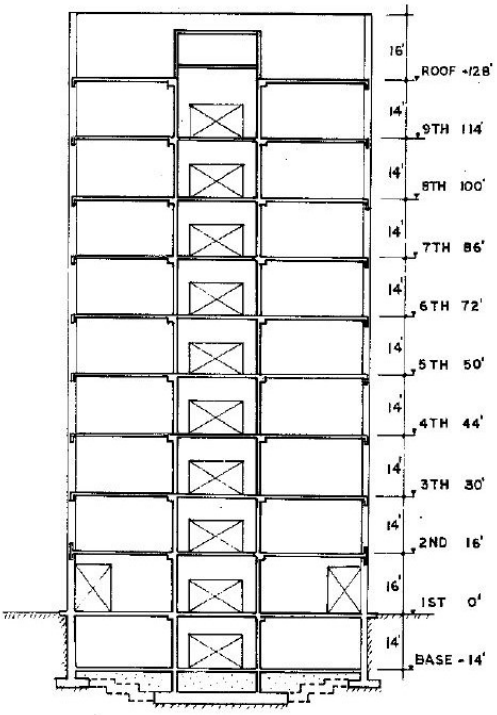

(b) North-south structural elevation

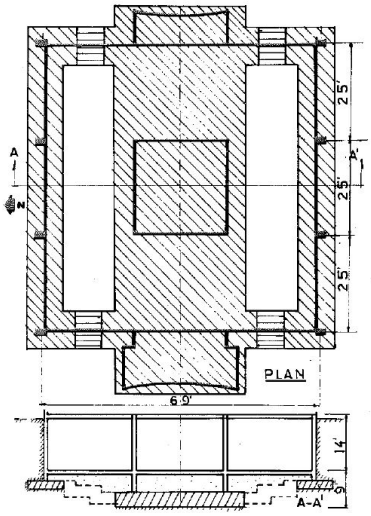

(c) Foundation plan with north-south elevation

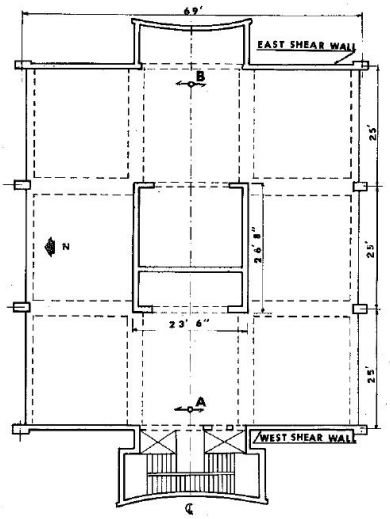

(d) Typical story plan

Figure 6.11: *The Millikan Library on the Campus of the California Institute of Technology (image from earthquake.usgs.gov; structural drawings originally published by Foutch [55]).*

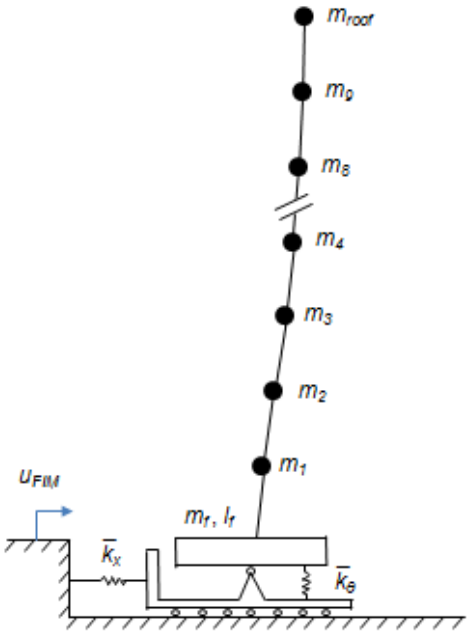

Figure 6.12: *Substructure Model of Millikan Library, redrawn from Foutch [55].*

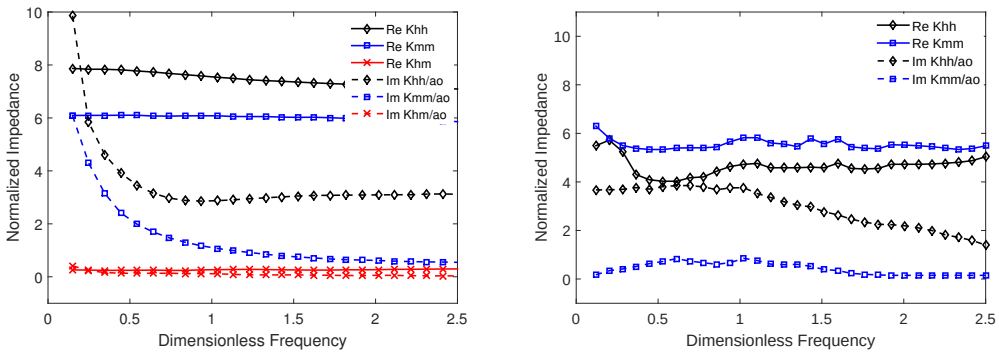

(a) Analytical **(b)** Identified

Figure 6.13: *Analytical and identified impedance functions for Millikan Library (adapted from Wong et al. [59] and Luco et al. [60]).*

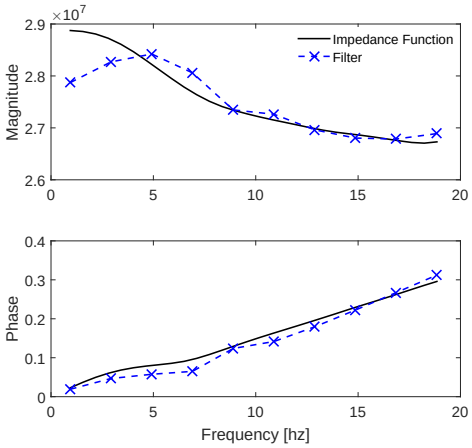

(a) Horizontal

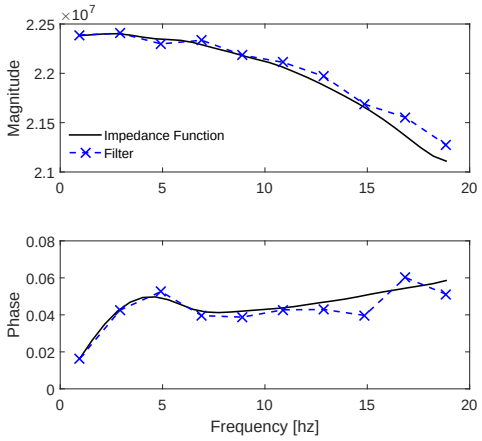

(b) Rocking

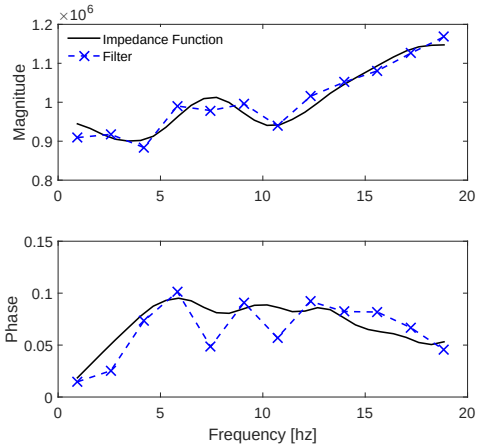

(c) Coupling

Figure 6.14: *Filter approximations of the Millikan Library's analytical impedance functions.*

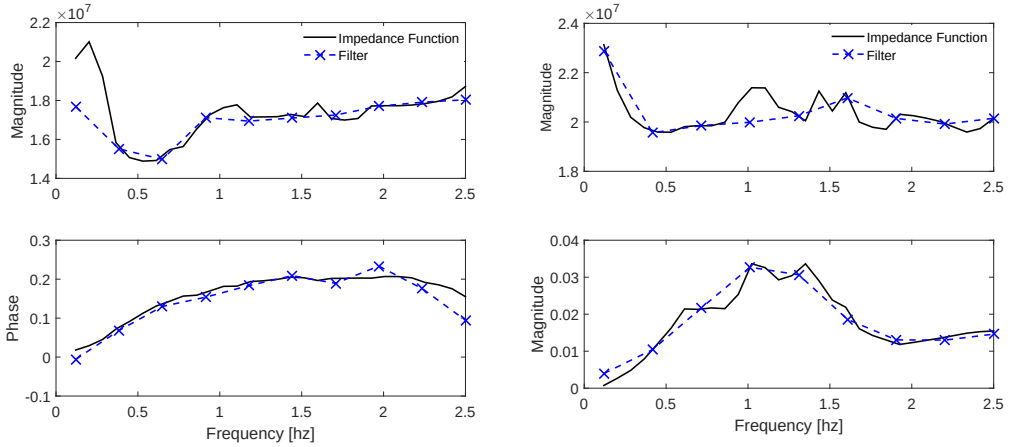

(a) Horizontal **(b)** Rocking

Figure 6.15: *Filter approximations of Millikan Library identified impedance functions.*

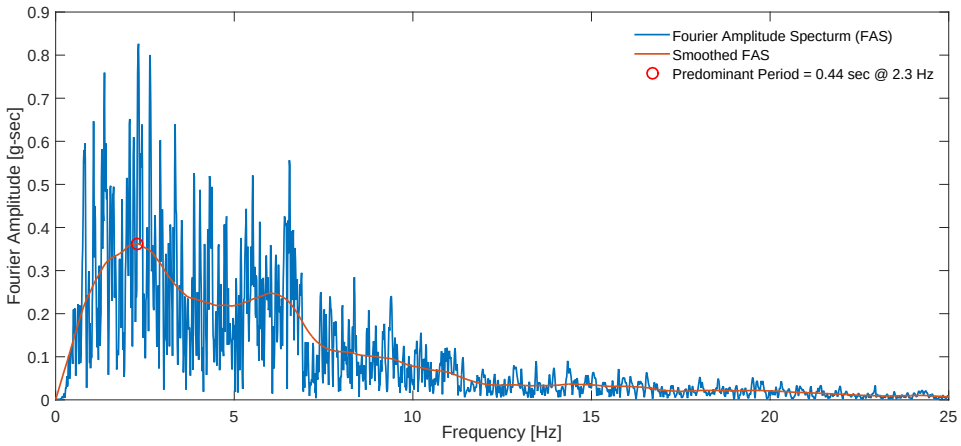

Figure 6.16: *Fourier amplitude spectrum of acceleration recorded by the 2002 Yorba Linda Earthquake at USGS Station No. 5407, Instrument 134, Channel 6.*

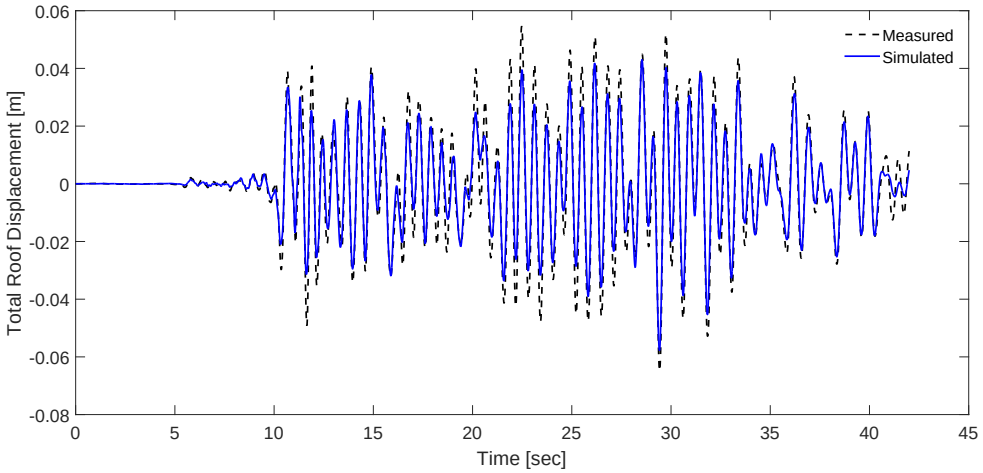

(a) Time History

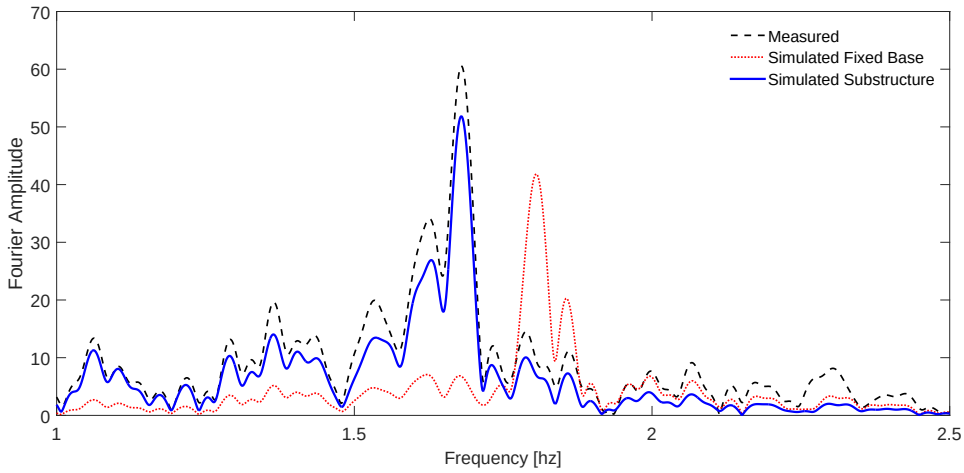

(b) Fourier Amplitude Spectrum

Figure 6.17: *Response of Millikan Library with analytical impedance to 2002 Yorba Linda Earthquake.*

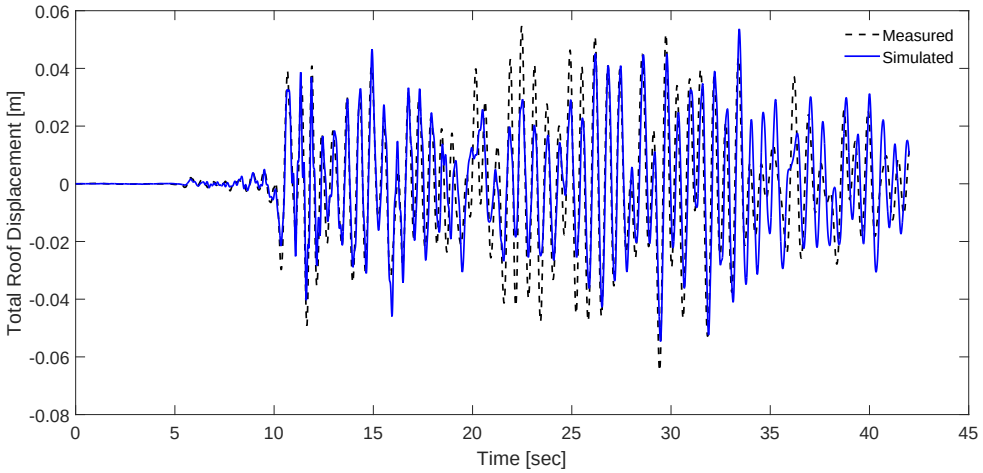

(a) Time History

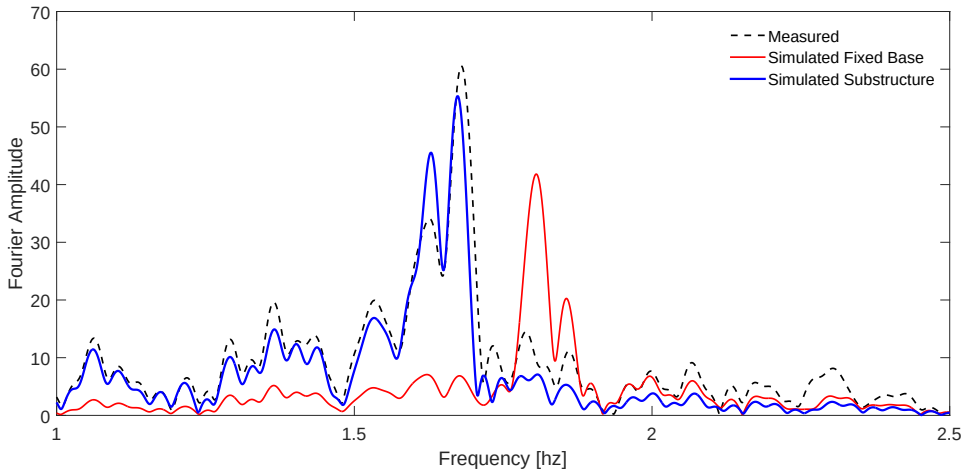

(b) Fourier Amplitude Spectrum

Figure 6.18: *Response of Millikan Library with identified impedance to 2002 Yorba Linda Earthquake.*

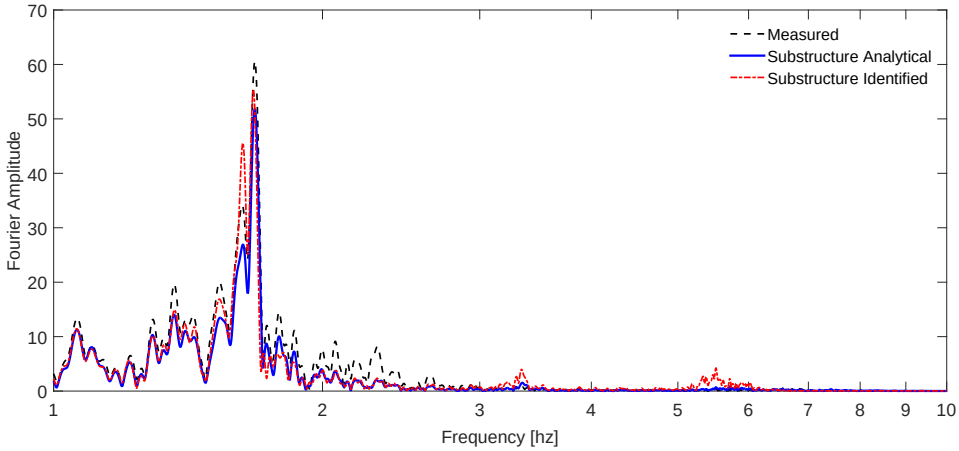

Figure 6.19: *Comparison of Fourier amplitude spectra of displacement time-history responses of Millikan Library to the 2002 Yorba Linda Earthquake.*

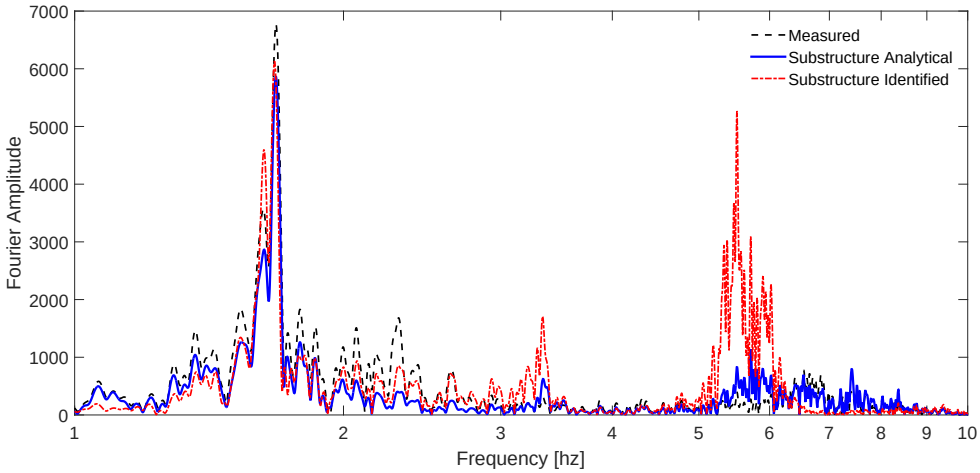

Figure 6.20: *Comparison of Fourier amplitude spectra of acceleration time-history responses of Millikan Library to the 2002 Yorba Linda Earthquake.*

CHAPTER 7

Discrete-Time Filter Design Revisited

Chapter 3 outlined the basics of discrete-time filter design and introduced the least squares method of curve fitting. This chapter revisits the filter design process, adding detail and offering options to improve both filter accuracy and stability. The goal being to assist a practicing civil engineer, who might not be familiar with the intricacies of signal processing, with the discrete-time filter design process. In general terms, filter design consists of three major steps: frequency sampling, frequency mapping, and curve fitting. Frequency sampling involves reduction of a continuous signal into a sequence of discrete values. Frequency mapping involves conversion of the signal's domain from continuous to discrete frequency. The final step, curve fitting, involves approximation of the resultant sequence of discrete impedance data by a ratio of two polynomials. The following sections explore the role of each of these steps on accuracy and stability. Included is a demonstration of how to modify and apply the MATLAB built-in function `invfreqz.m` [62] to accomplish filter design.

7.1 Sampling

Impedance data is typically available in three formats: as algebraic expressions; as plotted real and imaginary (or magnitude and phase) functions; or as tabular values. Sampling is the process by which data from the first two formats are reduced to sequences of discrete values. As tabular data is already discretized, the following does not directly apply, but an engineer may find that resampling

data (from any of the formats) at different sampling intervals may lead to improved accuracy and/or stability. To demonstrate the concept of sampling, consider the arbitrary continuous impedance function

$$\bar{k} = k + i\omega c \tag{7.1}$$

in which frequency, ω, assumes continuous values from zero to some maximum frequency, ω_{max}. Sampling involves evaluating $\bar{k}$ at each frequency, $l(\Delta\omega)$ where l takes integer values from one to L and $\Delta\omega$ is the sampling interval. Thus, the continuous function $\bar{k}$, when sampled, becomes the sequence,

$$\bar{k}_l = \left\{ \bar{k}_1 \quad \bar{k}_2 \quad \cdots \quad \bar{k}_L \,. \right\} \tag{7.2}$$

7.2 Mapping

Once the impedance data is discretized, the next step in the filter design process is to map the frequency samples from the continuous domain, to the discrete domain where frequency is defined around the unit circle from zero to 2π. This process is known as frequency warping [63]. As introduced in Chapter 3, this mapping is not linear, but is instead accomplished via the transformation

$$\Omega_l = 2 \arctan\left(\frac{\omega_l}{2f_s}\right) \tag{7.3}$$

in which f_s is the so-called *sampling frequency* which is equal to twice the value of the largest continuous frequency sample in hertz. Thus,

$$f_s = \frac{\omega_{max}}{2\pi} \,. \tag{7.4}$$

The non-linearity in this mapping leads to a distortion in the mapped discrete frequency domain. It is possible to control the effects of this distortion by selecting a pre-warping frequency that will minimize that distortion at the desired frequency in the discrete domain [32]. In the context of soil-structure interaction, this would

allow an engineer to specify a closer filter "fit" at the natural frequency of a structure, or at the anticipated predominant frequency of a ground motion. Pre-warped mapping is accomplished according to

$$\Omega_l = 2 \arctan \left(\frac{\omega_l \tan(\pi \frac{f_p}{f_s})}{2\pi f_p} \right) \tag{7.5}$$

where f_p is the designated pre-warping frequency in hertz.

7.3 Curve Fitting

The final step in the filter design process is fitting the impedance data with a curve described by a ratio of polynomials. As previously mentioned, algorithms for accomplishing this abound in signal processing literature. This work has demonstrated two, a standard approach based on Levy's [31] single least-squares error minimization and presented in Equation (3.10) and Sanathanan and Koerner's [33] iterative least-squares approach presented in Equation (3.18) and restated here:

$$E = \sum_{l=1}^{L} \left| D\bar{k}_j - N \right|^2 \frac{1}{|D|^2} \tag{7.6}$$

in which N represents the numerator polynomial:

$$N = b_0 + b_1 z^{-1} + \cdots + b_J z^{-J} \,, \tag{7.7}$$

and D represents the denominator polynomial:

$$D = 1 + a_1 z^{-1} + \cdots + a_J z^{-J} \,, \tag{7.8}$$

and z represents the z-transform parameter, L represents the total number of discrete frequencies Ω_l and J is the filter order. Although what follows is directed toward the iterative approach, it is equally applicable to the standard method.

7.3.1 Polynomial Order

There is no hard rule governing selection of the order of the filter numerator and denominator polynomials. In general, the more "wavy" the impedance function,

the higher the polynomial order that will need to be to offer an acceptable fit. However, as Safak cautions, using too high an order can lead to instability in addition to adding to computational expense. He suggests determining the polynomial order by designing filters of increasing order until the difference in the optimization error metric between successive iterations drops below a an appreciable level.

It is also important to note that the order of the numerator and denominator polynomials need not be the same. Indeed, for his rational approximations, Wolf suggests selecting the degree of the numerator to be one less than the degree of the denominator to aid in subsequent manipulation into lumped parameter models [24]. Interestingly, this author has found that the best fits tend to come using the opposite, a numerator order of one *greater* than the denominator. Unless otherwise stated, all filters in this work are designed as such.

7.3.2 Weight Functions

If difficulty is encountered obtaining a fit over a desired frequency range, weighting functions may be added to the least-squares approximation process to add emphasis to those frequencies. Modifying the iterative method in (7.8) to accommodate a given weight function, W_l yields:

$$E = \sum_{l=1}^{L} \left| D\bar{k}_l - N \right|^2 \frac{W_l}{|D|^2} \,. \tag{7.9}$$

Examples of weight functions that emphasize low frequencies include a simple frequency inverse, or standard weight function:

$$W_l = \frac{1}{\Omega_l} \,, \tag{7.10}$$

and the well known Gaussian weight function:

$$W_l = \frac{1}{\sigma\sqrt{2\pi}} e^{\frac{(\frac{\omega_l}{2\pi} - \mu)^2}{2\sigma^2}} \tag{7.11}$$

in which σ and μ represent the standard deviation and mean of the desired Gaussian distribution. This work uses $\sigma = 7$ and $\mu = 0$ throughout.

7.3.3 Filter Stability

An accurate curve fit is just one of two major requirements for an adequate filter. The second is stability. Unlike Chapter 4, which investigates stability of the combined filter-integrator, this section address only stability of the filter. A recursive discrete-time filter is said to be stable if all of its poles lie within the complex unit circles, the poles being the roots of the denominator polynomial D stated in (7.8). It is possible to stabilize and unstable filter by mirroring any offending poles inside the unit circle, but doing often involves a loss in accuracy. Often, the best way to stabilize a filter is to simply redesign using a different sampling interval, pre-warping frequency, and/or filter order. A filter design algorithm can be readily programmed to iteratively adjust these parameters until desired the desired fit is achieved.

7.4 Discrete-Time Filter Design Using the MATLAB Programming Environment

The MATLAB programming environment offers a built-in means for design of recursive discrete-time filters via the function `invfreqz.m`. The function `ImpedanceFilter.m` (the code for which is included in Appendix A) makes use of the `invfreqz.m` algorithm to design filters in an SSI context via the modified function `invfreqz2.m`. This function contains one minor debugging modification the details of which are outlined in `ImpedanceFilter.m`'s preamble. Inputs to `ImpedanceFilter.m` include the sampled impedance function $\bar{k}_l$, sampled continuous frequency ω_l in radians, the desired filter order, the desired pre-warping frequency in hertz, and user specified options controlling the least squares algorithm and weight function. The function returns the filter numerator and denominator coefficients b_j and a_j and the filter's transfer function H_l which can be juxtaposed with $\bar{k}_l$ to determine goodness of fit.

7.4.1 Frequency Warping

The function begins by warping the sequence of sampled continuous frequencies ω_l into a sequence of discrete frequencies Ω_l according to two options. If the user passes a pre-warping frequency of "0" the function uses the Line 47 to apply the standard mapping transform given in Equation (7.3). If the user passes a non-zero pre-warping frequency, the function uses Line 51 to apply the pre-warping transform given in Equation (7.5).

7.4.2 Weight Function

The function next computes the weight function according to the user's preference. Three options exist: no weight function computed on Line 55, the standard inverse frequency weight function of Equation (7.10) computed on Line 61, and the Gaussian weight function of Equation (7.11) computed on Line 59. The Gaussian weight function is coded have a mean of zero and a standard deviation of seven. This may be modified as desired by the user.

7.4.3 Least Squares Approximation

The function offers four least squares approximation options. These include a choice between a complex or real filter and the choice of whether of not to invoke MATLAB's `polystab.m` [62] function to stabilize the denominator polynomial. The `polystab.m` function reflects any pole outside the unit circle inside. As already mentioned, this may come at a cost in terms of accuracy. It should be noted that the least squares approximations in `invfreqz.m` are slightly different than those presented in this work, thus the coefficients of filters designed using `ImpedanceFilter` will be slightly different than those designed using (3.10) and (3.18)/(7.6).

7.5 Discrete-Time Filter Design Example

The following example demonstrates the effects of the aforementioned filter design parameters on both fit and stability. All curve fitting is done using the iterative least squares algorithm given in (7.6) or its weighted counterpart given in (7.9) via the MATLAB function `ImpedanceFilter.m`. The example uses the impedance function and soil-foundation parameters from the rigid disk on elastic soil layer above bedrock example in §3.3.2 of this work. Table 3.3 contains the values of relevant parameters. Figure 3.3 displays the impedance coefficients. The impedance function itself is given in equations (3.16) and (3.17).

The design parameters used for each iteration are listed in Table 7.1. The

Table 7.1: *Parameters for discrete-time filter design example.*

Iteration	No. of Samples	Frequency Step [hz]	Filter Order	Least Squares Option	Weight Option	Pre-Warping Frequency [Hz]
1	17	6	4	Real	None	0
2	17	6	13	Real	None	0
3	100	1	13	Real	None	0
4	100	1	13	Real	None	55
5	100	1	13	Real	Gaussian	55
6	100	1	13	Real	Standard	55
7	100	1	13	RealPolystab	Standard	55

resultant filters are shown in Figure 7.1 for iterations one through four and in Figure 7.2 for iterations five through seven.

7.5.1 Discussion of Results

Iteration 1

The first design iteration demonstrates the effects of selecting too low a filter order. The resultant filter is stable with a maximum pole radius of $r_p = 0.8952$, but as shown in Figure 7.1 (a), the fit is not good.

Iteration 2

The second iteration increases the filter order from $N = 4$ to $N = 13$. The result, shown in Figure 7.1 (b) is a much better fit. Unfortunately, the filter is now unstable with a maximum pole radius of $r_p = 1.0005$.

Iteration 3

For the third iteration, the impedance function is up-sampled to so $\bar{k}_l$ and ω_l include 100 samples at an interval of $\Delta_f = 1.0$ hertz. The filter is now stable, with a maximum pole radius of $r_p = 0.9826$. The fit, shown in Figure 7.1 (c) is still good, perhaps even better than Iteration 2's, but it has a distinct kink at around 55 hertz.

Iteration 4

In the fourth iteration, a pre-warping frequency of $f_p = 55$ hertz was used with goal of reducing distortion at that frequency. As seen in Figure 7.1 (d) this was achieved. However, although the result is still stable, with a maximum pole radius of $r_p = 0.9994$, the fit at the lowest frequency is now poor. As much of the frequency content of typical ground motions occur at relatively low frequencies, this may have a significant effect on the accuracy of any time-history response generated using the filter.

Iteration 5

The fifth iteration adds a Gaussian weight function to emphasize low frequencies during least squares optimization. The result of this are shown in Figure 7.2 (e). While fit to low frequencies is indeed very good, the fit to high frequencies has suffered greatly. Also, the resultant filter is unstable, with a maximum pole radius of $r_p = 1.1549$.

Iteration 6

The sixth iteration switches the Gaussian weight function with an inverse frequency, or standard, weight function. This result, shown in Figure 7.2 (f) is a stable filter (maximum pole radius $r_p = 0.9646$) with better fit, but still with inaccuracy at the lowest frequency.

Iteration 7 - Final Design

The final design uses the sampling rate, order, standard weight function, and prewarping frequency of the sixth iteration, but uses the "realpolystab" least squares option, invoking an iterative design with a prescribed maximum pole radius of one. Figure 7.2 (g) displays the result. The fit is good across the entire frequency range and the maximum pole radius of $r_p = 0.9031$ is indeed less than one. The coefficients of the final filter are displayed in Table 7.2.

Table 7.2: *Coefficients of discrete-time filter designed using* `ImpedanceFilter.m`.

j	A_j	B_j ($\times 10^{-4}$)
0	1.0000	0.4570
1	0.0948	−0.6097
2	1.5810	1.3377
3	−0.0988	−1.6254
4	0.9466	2.0422
5	0.0141	−2.0161
6	0.2623	1.9841
7	0.3422	−1.5752
8	−0.1164	1.2576
9	0.3602	−0.8267
10	−0.2289	−0.2641
12	−0.1068	0.1148
13	0.0690	−0.0411
14	−0.0150	0.0000

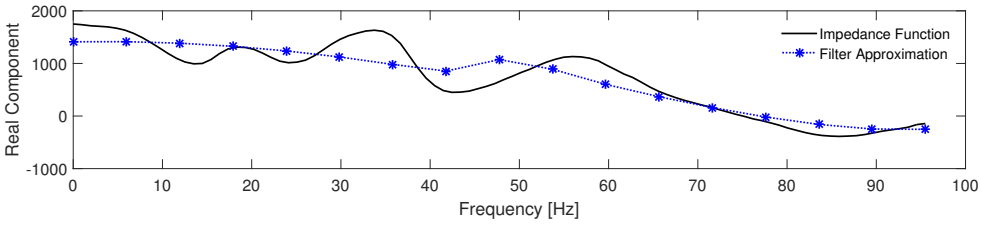

(a) Trial 1 - Low filter order yields poor fit.

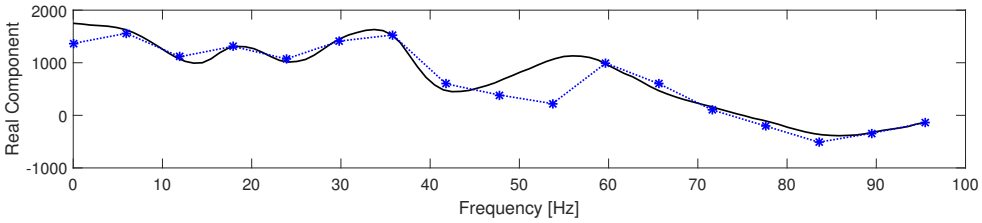

(b) Trial 2 - Increased filter order to address fit but resultant filter is unstable.

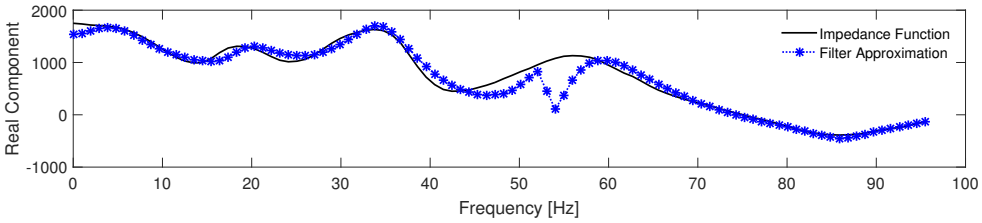

(c) Trial 3 - Up-sampled to address stability

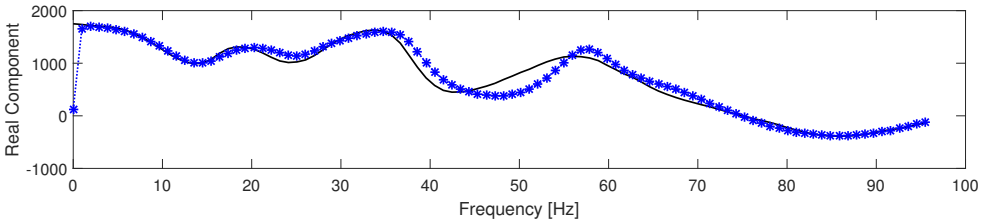

(d) Trial 4 - Frequency pre-warped at 55 Hz to address kink in fit.

Figure 7.1: *Iterations 1-4 of discrete-time filter design.*

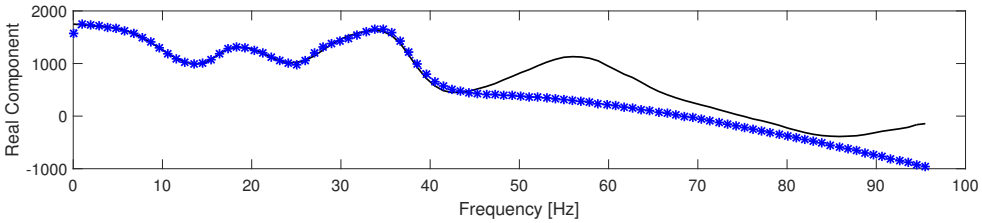

(a) Trial 5 - Gaussian weighting function added, poor fit, filter unstable

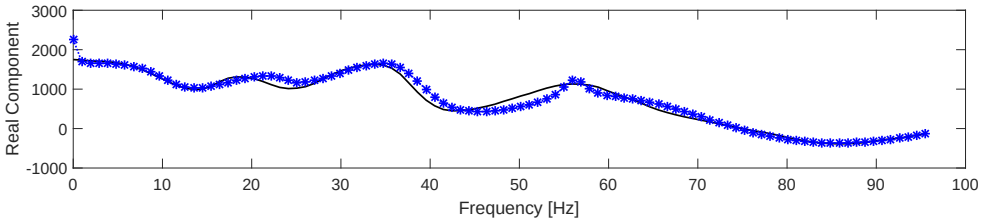

(b) Trial 6 - Standard weighting function added

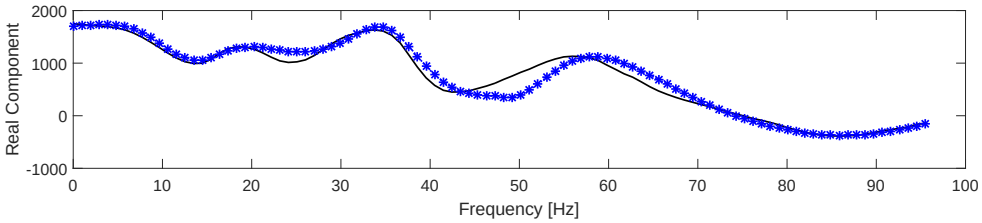

(c) Iteration 7 - Final Design - Iterative least squares with standard weight function

Figure 7.2: *Iterations 5-7 of discrete-time filter design.*

CHAPTER 8

Concluding Remarks

8.1 Summary

The goal of this dissertation is to offer practicing engineers a viable method of accounting for inertial soil-structure interaction in the time domain. The first chapter outlined four lines of effort that direct work toward that end. The first explored the background of, and motivation for, the use of discrete-time filters as time-domain approximations of frequency dependent foundation impedance functions. The second demonstrated implementation for systems with both elastic and inelastic structures. Addressed were both uncoupled, or scalar impedance functions, and coupled, or matrix impedance functions. For the matrix case, the multiple-input-multiple-output filter representing the impedance matrix was implemented as four single-input-single-output filters. Also included with this line of effort was a rigorous investigation into the stability of the method when combined with a time-stepping numerical integrator. To this author's knowledge, no previous works on rational approximations for use in SSI substructure analyses have have addressed this. It was shown that the equations of the combined filter-integrator may be reduced to a linear constant coefficient difference equation (LCCDE). If the roots of the characteristic equation of this LCCDE are all less than one, the combined filter-integrator will be stable.

The third line of effort applied the results of the second using practical applications that included ductility maps, constant ductility spectra, and the Millikan

Library case study. The ductility maps, corroborated Mylonakis and Gazetas' assertion that, contrary to the guidance of popular code-informing documents, inertial SSI may in fact be detrimental to inelastic structures. The second application demonstrated the ability of the filter method to generate site-specific constant ductility spectra using impedance functions generated via state-of-the-art computational methods. These spectra can vary significantly from those produced with impedance functions that assume simplified site geology. The final application demonstrated the ability of the filter method to predict the motion of Millikan Library when subjected the motion recorded at the site during the 2002 Yorba Linda Earthquake. This case study used both analytically derived and experimentally generated impedance functions. It was demonstrated that the response history generated using the analytical impedances offers a better match to the structure's motion as recorded during the earthquake.

These applications demonstrate the potential of the filter method, especially given continuing advances in computational methods for derivation of impedance functions and the growing demand for accurate, efficient response history analyses fueled by the rise of probabilistic based seismic design. While these lines of effort account for the majority of the project, in terms of both academic effort and written words, the true legacy of this work will be judged by its final line of effort, that of relevancy. To achieve its goal, practicing engineers must find this work of use. At first glance, the filter method may seem formidable. Mere mention of discrete-time filters is likely enough to scare off civil engineers who may lack experience in signal processing. Chapter 3 may only serve to make matters worse as it rigorously addresses both the method's derivation and the mathematical aspects of filter design. Chapter 7 is specifically targeted to allay such fears. It lays out the necessary details of the filter design process in an easy to follow manner and offers a design tool in the form of a filter design function for the MATLAB coding

environment. This function will provide filters that are ready to be inserted into equations of motion as outlined in Chapters 4 and 5 of this work. Download it and give it a try!

8.2 The Road Ahead

What of the road ahead? In general the way forward consists of two related, but distinct paths. The first is software development. As outlined in this work, the filter method is ready to be packaged as a module compatible with state-of-the-art structural analysis software. Such a tool would give engineers an accurate and efficient means of accounting for arbitrary (coupled or uncoupled) foundation impedances for both elastic and inelastic analyses. The second path is improved implementation. The signal processing community continues to invest significant effort into discrete time-filter design. Many cutting edge technologies such as speech-to-text, voice recognition, and wireless communication rely on discrete-time filters. As the signal processing state-of-practice continues to advance, so too will opportunities continue to arise to apply new techniques to the soil-structure interaction context. While there is certainly a learning curve involved in being able to understand and apply signal processing literature, it is an investment worth making. Specific areas that this author would like to see addressed include improved curve fitting over the least-squares approaches addressed in this work and a detailed investigation into the stability of coupled filters, or impedance matrices when combined with time-stepping numerical integration methods.

A third way ahead also exists. In general, the filter method offers a means of reducing the domain of the soil-foundation interface to the forces generated by notional springs and dashpots. This is in essence a model order reduction technique similar to that used in other dynamic analysis simulations such as vibration

of an airplane wing caused by rotating engine turbines. This third way ahead involves seeking out research areas outside the soil-structure interaction context where the filter method could be applied. Sharing knowledge with other fields, which may indeed be significantly ahead in terms of model order reduction, will directly benefit the civil engineering community.

Now is an exciting time to be a civil engineer. Computational methods continue to rapidly advance. The design community is rapidly shifting from prescriptive to performance-based methods. Construction materials and structural systems continue to evolve. All of these changes highlight the need to for efficient, accurate methods of conducting response history analyses of soil-foundation-structure systems. The filter method offers a viable means of meeting this need.

APPENDIX A

MATLAB Code: `ImpedanceFilter.m`

The following is a function coded in the MATLAB environment to generate the coefficients of a recursive discrete-time filter. As shown in the documentation, its use requires modification of the built-in MATLAB function `invfreqz.m`.

```
1  function [Az Bz H] = ImpedanceFilter(Kw,w,N,method,weight,fp)
2  % ******************************************************************
3  % Richard J.H. Gash
4  % 06 March 2013
5  %
6  % Function to compute time domain approximation of frequency dependent
7  % foundation impedance function.
8  %
9  % Input:
10 % Kw      1xn Complex Foundation Impedance Values
11 % w       1xn Frequency Values [Radians]
12 % N       1x1 Filter Order
13 % method  String identifying desired least squares algorithm
14 %           'Real' Designs a real filter
15 %           'Complex' Designs a complex fitler
16 %           'RealPolystab' Asks INVFREQZ2 to stabilize denominator
17 %           'ComplexPolystab' Asks INVFREQZ2 to stabilize denominator
18 % weight  String identifying desired weight funciton
19 %           'None' No weight function used
20 %           'Gaussian' Guassian weight function
21 %           'Standard' Standard weight function
```

```
% fp      1x1 Prewarping frequency in hz
%
% Note: INVFREQZ2 is a version of MATLAB function INVFREQZ modified
%       as follows to correct bug. Change line 179 as follows:
%              INVFREQZ: while all([V1 > Vcap ll<20])
%              INVFREQZ2: while all([V1 >= Vcap ll<20])
% Output:
% Az      1xN+1 IIR Denominator Coeffiecients
% Bz      1xN+1 IIR Numerator Coeffiecients
% H       1xn Transfer function of approximation
%
% Output can be organized into ratio of polynominals as:
%
%       Bz(1)*z^0+Bz(2)*z^(-1)+...+Bz(nzeros+1)*z^(nzeros)
%  H =  ---------------------------------------------------
%       Az(1)*z^0+Az(2)*z^(-1)+...+Az(npoles+1)*z^(npoles)
%
%  Where
%
%  z = exp(1i*pi*wd)
%
%*********************************************************************

f = w./(2*pi); %Frequency [Hz]
fs = 2*max(f); %Sampling Frequency [Hz]
% Frequency warping. No prewarping if fp = 0
if fp == 0
    wd = 2 *atan(w/(2*fs));
else
    wd = 2*atan(w*tan(pi*fp/fs)/(2*pi*fp));
end
% Calculate weight function
if strcmpi(weight,'None') == 1
    wt = ones(1,length(f));
```

```
elseif strcmpi(weight,'Gaussian') == 1
    mu = 0;      % Mean (May be adjusted by user)
    s = 7;       % Standard Devaiton (May be adjusted by user)
    wt = 1/(s*sqrt(2*pi))*exp(-(f-mu).^2./(2*s^2))*1000;
elseif strcmpi(weight,'Standard')
    wt = 1 ./ (2*pi*f);
end
% Compute Time Domain Approximation
n = 1;   % Make denominator one order higher than numerator
         % May be changed to suit user preference
if strcmpi('ComplexPolystab',method) == 1
    wd = [-fliplr(conj(wd)),wd];
    Kw = [fliplr(conj(Kw)),Kw];
    wt = [fliplr(conj(wt)),wt];
    [Bz,Az] = invfreqz2(Kw,wd,'complex',N,N+n,[wt],[]);
elseif strcmpi(method,'Complex') == 1
    wd = [-fliplr(conj(wd)),wd];
    Kw = [fliplr(conj(Kw)),Kw];
    wt = [fliplr(conj(wt)),wt];
    [Bz,Az] = invfreqz2(Kw,wd,'complex',N,N+n,[wt]);
elseif strcmpi(method,'RealPolystab') == 1
    [Bz,Az] = invfreqz2(Kw,wd,N,N+n,[wt],[]);
else
    [Bz,Az] = invfreqz2(Kw,wd,N,N+n,wt);
end
% Generate Transfer Function
H = freqz(Bz,Az,wd);

return
```

References

[1] Applied Technology Council (ATC), *Tentative Provisions for the Development of Seismic Regulations for Buildings, ATC-3-06.* San Fransisco, CA, 1978.

[2] G. Mylonakis and G. Gazetas, "Sesmic soil-structure interaction: Beneficial or detrimental," *Journal of Earthquake Engineering*, vol. 4, pp. 277–301, July 2000.

[3] C. Jeong, E. E. Seylabi, and E. Taciroglu, "A time domain substructuring method for dynamic soil structure interaction analyses of abitrarily shaped foundation geometries on heterogenous media," in *Proc. International Workshop on Computing in Civil Engineering*, pp. 346–353, ASCE, June 2013.

[4] J. M. Roesset, "Soil structure interaction the early years," *Journal of Applied Science and Engineering*, vol. 16, no. 1, pp. 1–8, 2013.

[5] E. Kausel, "Early history of soil-structure interaction," *Soil Dynamics and Earthquake Engineering*, vol. 30, no. 9, pp. 822–832, 2010.

[6] J. Zhang and Y. Tang, "Dimensional analysis of structures with translating and rocking foundations under near-fault ground motions," *Soil Dynamics and Earthquake Engineering*, vol. 29, pp. 1330–1346, 2009.

[7] National Institute of Standards and Technology (NIST), *Soil-Structure Interaction for Building Structures, NIST GCR 12-917-21.* Gaithersburg, MD, 2012. Prepared by the NEHRP Consultants Joint Venture, a Partnership of the ATC and CUREE.

[8] E. Reissner, "Stationäre, axialsymmetrische, durch eine schüttelnde masse erregte schwingungen eines homogenen elastischen halbraumes," *Ingenieur-Archiv*, vol. 7, no. 6, pp. 381–396, 1936. (in German).

[9] G. N. Bycroft, "Forced vibrations of a rigid circular plate on a semi-infinite elastic space and on an elastic stratum," *Philosophical Transactions of the Royal Society of London. Series A, Mathematical and Physical Sciences*, vol. 248, no. 948, pp. 327–368, 1956.

[10] A. Veletsos and Y. Wei, "Lateral and rocking vibration of footings," *Journal of the Soil Mechanics and Foundations Division*, vol. 97, no. 9, pp. 1227–1248, 1971.

[11] J. E. Luco and R. A. Westmann, "Dynamic response of circular footings," *Journal of the Engineering Mechanics Division*, vol. 97, no. 5, pp. 1381–1395, 1971.

[12] A. S. Veletsos and B. Verbic, "Vibration of viscoelastic founations," *Earthquake Engineering and Structural Dynamics*, vol. 2, pp. 87–102, 1973.

[13] A. Pais and E. Kausel, "Approximate formula for dynamic stiffnessess of rigid foundations," *Soil Dynamics and Earthquake Engineering*, vol. 7, pp. 213–227, October 1988.

[14] G. Gazetas, "Formulas and charts for impedances of surface and embedded foundations," *Journal of Geotechnical Engineering*, vol. 119, pp. 1363–1381, September 1991.

[15] J. Zhang and N. Makris, "Kinematic response functions and dynamic stiffnesses of bridge embankments," *Earthquake Engineering and Structural Dynamics*, vol. 31, no. 11, pp. 1933–1966, 2002.

[16] M. A. Ghannad, N. Fukuwa, and R. Nishizaka, "A study on the frequency and damping of soil-structure systems using a simplified model," *Journal of Structural Engineering, Architectural Institute of Japan*, vol. 44, pp. 85–93, 1998.

[17] J. P. Wolf, "Spring-dashpot-mass models for foundation vibrations," *Journal of Earthquake Engineering and Structural Dynamics*, vol. 26, pp. 931–949, 1997.

[18] W.-H. Wu and W.-H. Lee, "Systematic lumped-paramter models for foundations based on polynomial-fraction approximation," *Journal of Earthquake Engineering and Structural Dynamics*, vol. 31, pp. 1383–1412, 2002.

[19] N. M. Newmark, "A method of computation for strucutural dynamics," *Journal of the Engineering Mechanics Division*, vol. 85, no. EM3, pp. 67–94, 1959.

[20] A. Paronesso and J. P. Wolf, "Recursive evaluation of interaction forces and property matrices from unit-impulse response functions of unbounded medium based on balancing approximation," *Earthquake Engineering and Structural Dynamics*, vol. 27, pp. 609–618, June 1998.

[21] Y. Hayaski and H. Katukura, "Effective time-domain soil-structure interaction analysis based on fft algorithm with causality condition," *Earthquake Engineering and Structural Dynamics*, vol. 19, pp. 693–708, July 1990.

[22] N. Nakamura, "A practical method to transform freqeuncy dependent impedance to time domain," *Earthquake Engineering and Structural Dynamics*, vol. 35, pp. 217–234, February 2006.

[23] S. Luo and Z. Chen, "Iterative methods for extracting causal time-domain parameters," *IEEE Transactions on Microwave Theory and Techniques*, vol. 53, March 2005.

[24] J. P. Wolf, *Foundation Vibration Analysis Using Simple Physical Models*. Prentice Hall, 1994.

[25] E. Safak, "Time-domain representation of frequency-dependent foundation impedance functions," *Soil Dynamics and Earthquake Engineering*, vol. 26, pp. 65–70, 2006.

[26] J. P. Wolf and M. Motosaka, "Recursive evaluation of interaction forces of unbounded soil in the time domain from dynamic-stiffness coefficients in the frequency domian," *Earthquake Engineering and Structural Dynamics*, vol. 18, pp. 365–376, 1989.

[27] A. Paronesso and J. P. Wolf, "Global lumped-parameter model with physical representation for unbounded medium," *Earthquake Engineering and Structural Dynamics*, vol. 24, pp. 637–654, 1995.

[28] P. Ruge, C. Trinks, and S. Witte, "Time-domain analysis of unbounded media using mixed-variable formulations," *Earthquake Engineering and Structural Dynamics*, vol. 30, pp. 899–925, 2001.

[29] X.-L. Du and M. Zhao, "Stability and identification for rational approximation of frequency response fuction of unbounded soil," *Earthquake Engineering & Structural Dynamics*, vol. 39, pp. 165–186, 2010.

[30] X.-L. Du, M. Zhao, and L. Jiang, "Stability and identification for rational approximation of frequency response fuction of unbounded soil," in *14th World Conference on Earthquake Engineering*, October 2008.

[31] E. C. Levy, "Complex curve fitting," *IEEE Transactions on Automatic Control*, vol. AC-4, no. 1, pp. 37–44, 1959.

[32] A. V. Oppenheim, R. W. Schafer, and J. R. Buck, *Discrete-Time Signal Processing*. Prentice Hall Signal Processing Series, Upper Saddle River, New Jersey: Prentice Hall, 2nd ed., 1998.

[33] C. K. Sanathanan and J. Koerner, "Transfer function synthesis as a ratio of two complex polynomials," *IEEE Transactions on Automatic Control*, vol. 8, pp. 56–58, January 1963.

[34] K.-J. Bathe, *Finite Element Procedures in Engineering Analysis*. Upper Saddle River, New Jersey: Prentice Hall, 1982.

[35] M. G. Katona, R. Thompson, and J. Smith, "Efficiency study of implicit and explicit time integration operators for finite element applications," Technical Report R856, United States Defense Nuclear Agency, 1977.

[36] T. Hull and W. A. J. Luxemburg, "Numerical methods and existence theorems for ordinary differential equations," *Numerische mathematik*, vol. 2, no. 1, pp. 30–41, 1960.

[37] American Society of Civil Engineers (ASCE), *Minimum Design Loads for Buildings and Other Structures*. Reston, VA, ASCE/SEI 7-10 ed., 2013.

[38] Applied Technology Council (ATC), *Improvement of Nonlinear Static Seismic Procedures, FEMA 440*. Applied Technology Council, Washington, D.C., 2005.

[39] J. Avilés and L. E. Pérez-Richa, "Soil-structure interaction in yielding systems," *Earthquake Engineering and Structural Dynamics*, vol. 32, pp. 1749–1771, September 2003.

[40] F. Khoshnoudian and I. Behmanesh, "Evaluation of fema 440 for including soil-structure interaction," *Earthquake Engineering and Engineering Vibration*, vol. 97, pp. 397–408, September 2010.

[41] Applied Technology Council (ATC-55 Project), *Next Generation Performance Based Seismic Design, FEMA 445*. Federal Emergency Management Agency, August 2006.

[42] Applied Technology Council (ATC), *Preliminary Evaluation of Methods for Defining Performance, ATC 58-2*, 2003.

[43] Structural Engineers Association of California (SEOSC), "Vision 2000: Performance based seismic design of buildings, volume i," tech. rep., SEOSC, April 1995.

[44] S. Jarernpasert, E. Bazan-Zurita, and J. Bielak, "Seismic soil-structure interaction reponse of inelastic structures," *Soil Dynamics and Earthquake Engineering*, vol. 47, pp. 132–143, April 2013.

[45] A. K. Chopra, *Dynamics of Structures: Theory and Application to Earthquake Engineering*. Prentice Hall, 2nd ed., 2001.

[46] J. C. Simo and T. Hughes, *Computational Elasticity*. Springer-Verlag, 1998.

[47] H. Krawinkler, F. Parsi, L. Ibarra, A. Ayoub, and R. Medina, "Development of a testing protocol for woodframe structuresa: Curee publication no. w-02," tech. rep., Consortium of Universities for Research in Earthquake Engineering, 2001.

[48] R. L. Finney and G. B. Thomas, *Calculus*. Addison-Wesley, 1992.

[49] N. Ricker, "The form and laws of propogation of seismic wavelets," *Geophysics*, vol. 18, pp. 10–40, January 1953.

[50] M. D. Trifunac, "Early history of the response spectrum method," *Soil Dynamics and Earthquake Engineering*, vol. 28, pp. 676–685, September 2008.

[51] M. A. Ghannad and H. Jahankhan, "Strength reduction factors considering soil-structure interaction," in *13th World Conference on Earthquake Engineering*, August 2004.

[52] F. Khoshnoudian, E. Ahmadi, and S. Sohrabi, "Response of nonlinear soil-mdof structure systems subjected to distinct frequency components of near-fault ground motions," *Earthquake Engineering and Structural Dynamics*, vol. 43, pp. 701–716, 2014.

[53] B. Ganjavi and H. Hao, "Ductility reduction factor for multi-degree-of-freedom systems with soil-structure interaction," in *15th World Conference on Earthquake Engineering*, 2012.

[54] F. A. Nik and F. Khoshnoudian, "Strength reduction factor for multistory building-soil systems," *Earthquakes and Structures*, vol. 6, no. 3, 2014.

[55] D. A. Foutch, "A study of the vibrational charateristics of two multi-story buildings," tech. rep., Earthquake Engineering Research Laboratory, 1976.

[56] J. H. Koroiwa, "Vibration tests of a multistory building," Master's thesis, California Institute of Technology, 1967.

[57] P. C. Jennings and J. H. Kuroiwa, "Vibration and soil-structure interaction tests of a nine-story reinforced concrete building," *Bulletin of the Seismological Society of America*, vol. 58, pp. 891–916, June 1968.

[58] R. T. Eguchi, "Shear velocities and near-surface geologies at accelerograph sites that recorded the san fernando earthquake," tech. rep., University of California, Los Angeles, 1976.

[59] H. Wong, M. Trifunac, and J. Luco, "A comparison of soil-structure interaction calculations with results of full-scaled forced vibration tests," *Earthquake Engineering and Structural Dynamics*, vol. 7, no. 1, pp. 22–31, 1988.

[60] J. Luco, M. Trifunac, and H. Wong, "Isolation of soil-structure interaction effects by full-scale forced vibration tests," *Earthquake Engineering and Structural Dynamics*, vol. 16, pp. 1–21, 1988.

[61] R. Apsel and J. Luco, "Impedance functions for foundations embedded in a layered medium," *Earthquake Engineering and Structural Dynamics*, vol. 15, pp. 213–231, February 1987.

[62] MATLAB, *Version 8.5.0 (R2015a)*. Natick, MA: The Mathworks, Inc, 2015.

[63] A. V. Oppenheim and D. H. Johnson, "Discrete representation of signals," *Proceedings of the IEEE*, vol. 60, pp. 681–691, June 1972.